On the estimation of nitrous oxide flux from agricultural fields of Canterbury New Zealand using micro-meteorological methods

---

A thesis

submitted in partial fulfilment

of the requirements for the degree

of

Doctor of Philosophy in Environmental Science

by

Sandipan Mukherjee

October 1, 2013

"... To my parents and to my extended family ..."

Abstract

Traditionally, agricultural nitrous oxide (N_2O) emission of New Zealand has been measured using chambers or lysimeters, and micrometeorological flux measurement experiments have been very few. Since micrometerological flux measurement systems have the advantage of measuring spatially integrated flux values for longer time periods compared to measurements made using chambers, development and verification of such a system was needed for New Zealand's agro-meteorological conditions. In this study, efficacy of such a combined flux gradient (FG) - eddy covariance (EC) micrometeorological flux measurement system is verified by continuously measuring N_2O fluxes from some control and mitigated agricultural plots of New Zealand. The control fields had natural N_2O emission, whereas, the mitigated plots were treated with chemicals to reduce N_2O emission.

In this combined FG-EC method, the turbulent eddy diffusivities were estimated using the Monin-Obukhov (M-O) similarity theory based parameterization (where diffusion velocity 'd_h^p' was used) and a thermal approach (where eddy diffusivity 'k_h^t' was used) from the EC measurements. These transfer coefficients (k_h^t and d_h^p) along with the measured N_2O concentration differences were then fitted to the traditional FG equation to compute final flux values. As the primary objective of this study, measured fluxes from two different seasons and from two approaches were compared for consistency and then verified against published results. Under this wider objective of verification of the FG-EC micrometeorological method of N_2O flux estimation, this research thesis addresses three key issues: (i) assessment of error propagation in the measured flux through the eddy diffusivity - to understand the random error dynamics of the system and to estimate precision of the overall method, (ii) quantification and separation of N_2O source area emission rates from adjacent plots - to identify the contribution of an individual plot to the measured flux when multi-plot fluxes were measured from sources with different biogenic characters, and (iii) quantification of the effect of animal grazing and mitigation on the measured flux and actual emission

rate of N_2O - to assess robustness of the FG-EC micrometeorological system. As a fourth objective of this study, (iv) new scaling properties of a turbulence surface layer model of a convective atmosphere is investigated as an alternative to the standard M-O similarity theory, as significant questioning of the M-O theory has been reported in some recent publications.

Results from the verification experiment showed that the daily measured flux values obtained from this combined micrometeorlogical system for control plots varied between 0-191.9 and 0-491.8 $gN_2O\text{-}N.ha^{-1}.day^{-1}$ for autumn and spring experiments, respectively, for the parameterization method. Similarly, the daily mean flux values were found to be 10.9 ± 0.98 and 11.7 ± 0.57 $gN_2O\text{-}N.ha^{-1}.day^{-1}$ for the autumn and spring seasons, respectively. All these values were found to be of **the same order of previously reported values** in the literature and found to verifying that this FG-EC system works well under a range of meteorological conditions within a defined error range. Therefore, when the propagated random error was computed in the final flux value using k_h^t and d_h^p, the mean relative error in k_h^t was found to be higher than the mean relative error in d_h^p, irrespective of stability. From a Monte-Carlo type simulation of the random error, it was found that the maximum error can be up to 80% for k_h^t irrespective of stability, and 49% and 35% for d_h^P respectively for stable ($1/L \geq 0$, where L is Obukhov length) and unstable ($1/L < 0$) atmosphere. Errors in the concentration differences were estimated based on the minimum resolvable estimates from the gas analyzer and the associated random errors were found to be 6% and 8% for unstable and stable conditions. Finally, the total mean random error in the N_2O flux values was found to be approximately of the order of 9% and 12% for the parameterization method for unstable and stable conditions, respectively, and 16.5% for the thermal method, irrespective of stability.

Objective (ii) of this research was addressed by developing a 'footprint fraction' based inverse footprint method. Results of the footprint analysis method were assessed, first, by comparing footprint fractions obtained from both an analytical footprint model and a 'forward' simulation of a backward Lagrangian stochastic (bLs) model; and second, by comparing the source area emission rates of a control plot obtained from the footprint analysis method and from the 'backward' simulation of the bLs model. It was observed that the analytical footprint fractions were realistic as they compared well with the values obtain from the bLs model. The actual emission rates were found to be on average 2.1% higher than the measured flux values for the control plots. On average 4.3% of the measured fluxes were found to be contributed by source areas outside of

the field domain. Again, the proposed footprint method of emission rate estimation was found to work well under a wider range of atmospheric stability, as the inverse footprint model and bLs model based emission rates were found to correlate well (0.70 and 0.61 for autumn and spring, respectively) with a 99% statistical significance.

Similarly when the effect of grazing on the N_2O fluxes was considered, a 90% enhancement in the flux values was observed after grazing, followed by a decreasing trend in fluxes. However, contrary to existing knowledge of mitigation of N_2O flux by an inhibitor, this study found no statistically significant effect of mitigation in the pastoral emission of N_2O. Error accumulation, lesser soil N_2O production potential and/or inefficiency of the FG-EC method was conjectured to be reason/s for such discrepancy and some alternative convective boundary layer turbulence scaling was tested. Separate field measurement data, including the vertical profile measurements of the convective boundary layer and sonic anemometer measurements within the surface layer were used for this purpose. The spectral analysis of the vertical wind component, temperature and heat flux revealed that this new model of the convective boundary layer, which explains atmospheric boundary layer turbulence in terms of some nonlocal parameters, is more suitable than the traditional Monin-Obukhov similarity theory based model of atmospheric turbulence where the atmospheric flow properties are local. Therefore, it can be concluded that this new model of turbulence might provide the framework for a newer model of flux **estimation in future**.

Overall, the FG-EC model of N_2O flux estimation method seems to work well within a certain error range. However, more field applications of this FG-EC method are needed for different agro-meteorological conditions of New Zealand before this method is accepted as a standard method of flux estimation, particularly, inefficiency in detecting the effect of mitigation should be tested. Development of an alternative flux gradient model which includes nonlocal atmospheric surface parameters might also be considered as a future research objective.

Acknowledgment

I am indebted to **Prof. Andrew Sturman** and **Dr. Peyman Zawar-Reza** for providing me the opportunity of doing my PhD study at the University of Canterbury under their supervision. I would specially like to thank Andy for his continuous advice, encouragement and support through out my study period. Discussions with Peyman were always nice and more than formal. I mostly enjoyed those conversations which were beyond the horizon of science. Again, thanks to Andy and Peyman, without their continuous support this thesis wouldn't have been possible.

I would like to thank **Dr. Andrew McMillan** and **Dr. Mike Harvey** from National Institute of Water and Atmospheric Research, New Zealand. I am obliged to both of them for providing me a research grant (contract no. CO1X0816 from Ministry for Primary Industries, New Zealand) for this study and co-supervising my thesis. I am grateful to Andrew for all those micrometerology tips that he gave me during our field trip days. I didn't have any field experiment skill before I joined this project and Andrew, Mike, Tony Bromley, Ross Martin and Matt Evans from NIWA, Wellington have helped me a lot to learn.

My sincere thanks to **Dr. Johannes Laubach**, Landcare Research, Lincoln, New Zealand. Johannes was not a part of my thesis supervisory group, but he did more than a formal thesis supervision. I am grateful for his insightful comments, ideas and reviews on some of my research chapters. I always enjoyed working with him.

My sincere thanks to **Dr. Keith McNaughton**, School of GeoSciences, The University of Edinburgh, UK for his insightful comments about the spectral work of my thesis.

Many thanks to **Justin Harrison** and **Nick Key** for helping me on my field work in 2011. Thanks to **Steven Sykes** and **Graham Furniss** for resolving my computer issues. Thanks to Marwan, Basit, Mohammad, Zahid, Colin and Omid for constructive discussions during my study period.

Finally, thanks to my parents, relatives and friends for their continuous support and encouragement, specially during the earthquake period of 2011.

Abbreviations

List of repeatedly used symbols and abbreviations are provided here. Other symbols are explained in the text.

ABL	Atmospheric boundary layer	-
b	Turbulent kinetic energy (TKE)	$m^2\ s^{-2}$
bLs	Backward Lagrangian stochastic footprint model	-
CBL	Convective boundary layer	-
CDS	Chaotic dynamical system	-
d	Displacement height	m
d_h^p	Diffusion velocity	$m\ s^{-1}$
EC	Eddy covariance method	-
$ER_{F^0_{eqn}}$	Emission rate using F^0 from numerical method	$gN_2O\text{-}N\ ha^{-1}\ day^{-1}$
ER_{bLs}	Emission rate from bLs model	$gN_2O\text{-}N\ ha^{-1}\ day^{-1}$
$F^{1,2,3,4}$	Measured flux at masts 1 to 4	$gN_2O\text{-}N\ ha^{-1}\ day^{-1}$
FG	Flux gradient method	-
F_g	Surface flux density	$kg\ m^{-2}\ s^{-1}$
F_0	Background flux	$kg\ m^{-2}\ s^{-1}$
f_p	Footprint function	-
F_{N_2O}	Surface flux density of N_2O gas	$gN_2O\text{-}N\ ha^{-1}\ day^{-1}$
k	Wave number in turbulence spectra	m^{-1}
k_h, k_m, k_g	Eddy diffusivity of heat, momentum and a gas	$m^2\ s^{-1}$
k_h^t	Thermal eddy diffusivity of heat	$m^2\ s^{-1}$
k_h^p	Parameterized eddy diffusivity of heat	$m^2\ s^{-1}$
L	Obukhov length	m
LFC	Layer of free convection	-
ML	Mixed Layer	-
MO	Monin-Obukhov	-

MNL	McNaughton-Laubach	-
SE	Standard error	-
SFL	Surface friction layer (CDS approach of turbulence)	-
SFM	Statistical fluid mechanics	-
SL	Surface layer (SFM approach of turbulence)	-
T	Temperature	°C
TEAL	Theodorsen ejection amplifier like	-
u, v and w	Wind speed components	m s^{-1}
$u_\star$	Friction velocity	m s^{-1}
u_ϵ	Dissipation velocity	m s^{-1}
$\overline{w'T'}$	Temperature flux	m s^{-1}°C
z or z_m	Measurement height	m
z_i	CBL height	m
z_0	Roughness length	m
z_s	Surface friction layer height	m
ΔC_{N_2O}	Concentration gradient of N_2O	ppb
Δz	Height gradient	m
$\Delta C_{N_2O}^{min}$	Minimum resolvable concentration gradient of N_2O	ppb
ΔT	Temperature gradient	°C
$\delta d_h^p / d_h^p$	Relative error in Diffusion velocity	-
$\delta k_h^t / k_h^t$	Relative error in thermal eddy diffusivity of heat	-
$\delta L / L$	Relative error in Obukhov length	-
$\delta \Delta T / \Delta T$	Relative error in temperature gradient	-
$\delta u_\star / u_\star$	Relative error in $u_\star$	-
$\delta \overline{w'T'} / \overline{w'T'}$	Relative error in temperature flux	-
$\delta \Delta z / \Delta z$	Relative error in height gradient	-
ϵ	TKE dissipation rate	m^2 s^{-3}
ϵ_0	TKE dissipation rate at the CBL	m^2 s^{-3}
γ	Footprint fraction from a footprint model	-
κ	von Karman constant = 0.40	-
η	inverse of γ	-
ϕ_h, ϕ_m, ϕ_g	Stability functions of heat, momentum and gas	Non-dimensional
ψ_h, ψ_m, ψ_g	Integrated stability functions of heat, momentum and gas	Non-dimensional
ρ_a	Density/concentration of air	kg m^{-3}
ρ_g	Density/concentration of a gas	kg m^{-3}

Notes

- Part of Chapter - 3 is under review in *Atmospheric Environment* as: "*Assessment of error propagation in the measured flux values of a micrometeorological method through eddy diffusivity*", S. Mukherjee, AP Sturman, AM McMillan, M Harvey, P Zawar-Reza. 2013.

- A modified part of Chapter - 4 is prepared for *Journal of Applied Meteorology and Climatology* as: "*Footprint methods to separate N_2O emission rates from adjacent paddock areas*", S Mukherjee, AM McMillan, AP Sturman, M Harvey, J Laubach. 2013.

Other publications associated with this project is:

- Manuscript submitted to *Agricultural and Forest Meteorology* as: "*A micrometeorological method to assess the efficacy of a nitrous oxide mitigation strategy*", AMS McMillan, M Harvey, R Martin, T Bromley, M Evans, S Mukherjee, J Laubach. 2013.

- M Harvey, AMS McMillan, M Ross, AM Bromley, MJ Evans, J Laubach, S Mukherjee. Development of micrometeorological techniques for assessing nitrous oxide emission and mitigation from dairy pastures. In: *Greenhouse Gases and Animal Agriculture Conference (GGAA2013)*, Dublin Ireland, 23-26 June 2013.

- S Mukherjee, AP Sturman, AMS McMillan, M Harvey, P Zawar-Reza. Analysis of uncertainty in the nitrous oxide flux values measured using a coupled eddy covariance - flux gradient technique. In: *American Geophysical Union Fall Meeting*, San Francisco, 2012.

Deputy Vice-Chancellor's Office
Postgraduate Office

UNIVERSITY OF CANTERBURY
Te Whare Wānanga o Waitaha
CHRISTCHURCH NEW ZEALAND

Co-Authorship Form

This form is to accompany the submission of any thesis that contains research reported in co-authored work that has been published, accepted for publication, or submitted for publication. A copy of this form should be included for each co-authored work that is included in the thesis. Completed forms should be included at the front (after the thesis abstract) of each copy of the thesis submitted for examination and library deposit.

Please indicate the chapter/section/pages of this thesis that are extracted from co-authored work and provide details of the publication or submission from the extract comes:

*A modified part of chapter 3 is under review to a peer reviewed journal, 'Atmospheric Environment', as: "*Assessment of error propagation in measured flux values obtained using an eddy diffusivity based micrometeorological method*", Sandipan Mukherjee, Andrew Sturman, Andrew McMillan, Mike Harvey, Peyman Zawar-Reza. 2013.*

Please detail the nature and extent (%) of contribution by the candidate:

The PhD candidate was responsible for the computer modelling, data analysis and write-up of this paper (85%). The co-authors provided regular advice and feedback on the paper as it was developed (15%).

Certification by Co-authors:

If there is more than one co-author then a single co-author can sign on behalf of all

The undersigned certifies that:

- The above statement correctly reflects the nature and extent of the PhD candidate's contribution to this co-authored work
- In cases where the candidate was the lead author of the co-authored work he or she wrote the text

Name: Prof. *Andrew Sturman* Signature:  Date: *9/5/2013*

Deputy Vice-Chancellor's Office
Postgraduate Office

UNIVERSITY OF CANTERBURY
Te Whare Wānanga o Waitaha
CHRISTCHURCH NEW ZEALAND

Co-Authorship Form

This form is to accompany the submission of any thesis that contains research reported in co-authored work that has been published, accepted for publication, or submitted for publication. A copy of this form should be included for each co-authored work that is included in the thesis. Completed forms should be included at the front (after the thesis abstract) of each copy of the thesis submitted for examination and library deposit.

Please indicate the chapter/section/pages of this thesis that are extracted from co-authored work and provide details of the publication or submission from the extract comes:

*A modified part of chapter 4 has been prepared for a peer reviewed journal, 'Journal of applied meteorology and climatology', as: "*Footprint methods to separate N_2O emission rates from adjacent paddock areas*", Sandipan Mukherjee, Andrew McMillan, Andrew Sturman, Mike Harvey, Johannes Laubach. 2013.*

Please detail the nature and extent (%) of contribution by the candidate:

The PhD candidate was responsible for the computer modelling, data analysis and write-up of this paper (85%). The co-authors provided regular advice and feedback on the paper as it was developed (15%).

Certification by Co-authors:

If there is more than one co-author then a single co-author can sign on behalf of all

The undersigned certifies that:

- The above statement correctly reflects the nature and extent of the PhD candidate's contribution to this co-authored work
- In cases where the candidate was the lead author of the co-authored work he or she wrote the text

Name: Prof. *Andrew Sturman* Signature:  Date: *9/5/2013*

Contents

i

Abstract **iii**

Acknowledgment **vii**

Abbreviations **ix**

Notes **xiii**

1 General introduction **1**
1.1 Background 1
1.2 Research objectives 7
1.3 Thesis outline 8

2 Overview of measurement techniques and a brief climatology of the experimental field **11**
2.1 Introduction 11
2.2 Non flow through non-steady state chambers 11
2.2.1 Operating principles 13
2.2.2 Advantages and disadvantages 14
2.3 Micrometeorological measurement techniques 14
2.3.1 Eddy covariance 15
2.3.2 Flux gradient 16
2.3.3 Flux footprint models for source area estimation 17
2.3.4 Advantages and disadvantages 20
2.4 Overview of climatology of the experimental site 22
2.5 Comments 24

3 Measurement of nitrous oxide flux and assessment of error propagation **27**
3.1 Introduction 27

3.2 Theory: flux gradient relationships . . . 29
3.3 Description of experimental site . . . 31
3.4 Instrumentation and measurement details . . . 32
3.4.1 Data description and processing . . . 33
3.4.2 Measurement heights . . . 35
3.5 Results . . . 35
3.5.1 Turbulence statistics . . . 35
3.5.2 Stability parameter ($1/L$) - inverse Obukhov length . . . 37
3.5.3 Wind distribution and roughness length . . . 39
3.5.4 Transfer coefficients . . . 40
3.5.5 Nitrous oxide flux . . . 42
3.5.6 Uncertainties in transfer coefficients . . . 48
3.5.7 Measure of uncertainty in transfer coefficient terms . . . 52
3.5.8 Error sensitivity study using a Monte-Carlo type method . . . 56
3.5.9 Measure of uncertainty in the nitrous oxide concentration difference term . . . 60
3.6 Summary and conclusion . . . 62

4 Estimation of source area emission rates using footprint methodologies 65
4.1 Introduction . . . 65
4.2 Experimental setup and measurements . . . 67
4.3 Methods and footprint models . . . 68
4.3.1 Numerical setup for estimating source area emission rate . . . 69
4.3.2 Analytical flux footprint model . . . 72
4.3.3 Backward Lagrangian model . . . 73
4.4 Results and discussion . . . 74
4.4.1 Footprint from analytical models . . . 74
4.4.1.1 Measured fluxes and emission rates from control plots 78
4.4.1.2 Error analysis of the analytical footprint model . . . 80
4.4.2 bLs model setup . . . 82
4.4.3 Comparison with analytical model . . . 83
4.4.3.1 Comparison of the footprint fraction values . . . 83
4.4.3.2 Comparison of the surface emission rates . . . 84
4.5 Conclusion . . . 86

5 Assessment of grazing and mitigation effects on nitrous oxide flux 89
5.1 Introduction . . . 89
5.2 Description of field activity . . . 91
5.3 Results . . . 91

5.3.1 Effect of grazing on the measured flux values 91
5.3.2 Measured flux from the experimental plot 93
5.3.3 Effect of mitigation on the measured flux and comparison with the control plots 95
5.3.4 Effect of mitigation on N_2O emission rates from the experimental plots after footprint correction 99
5.4 Discussion 100

6 Analysis of the spectral properties of turbulence and some alternative scaling parameters 103
6.1 Preface 103
6.2 Introduction 103
6.3 Theory 106
6.3.1 Inner and outer eddies and their interactions 106
6.3.2 Profiles of TKE and TKE dissipation rate 108
6.4 Experimental site, instrumentation and data description 109
6.5 Results 111
6.5.1 Analysis of the profile measurements 111
6.5.2 MLsp from the 10 m mast 113
6.5.2.1 Estimation of TKE dissipation rate in the CBL . . . 113
6.5.2.2 Estimation of SFL height and dissipation velocity . 114
6.5.2.3 Estimation of CBL depth 115
6.5.3 Spectra from the 10 m mast 117
6.5.3.1 w - wind component spectra 117
6.5.3.2 Temperature spectra 118
6.5.3.3 Heat flux co-spectra 120
6.6 Summary and conclusion 121

7 Summary, discussion and future work 125
7.1 Discussion 128
7.2 Possible future work 130

A WPL Correction 131

B Coordinate rotation 133

C Essential findings of McMillan et al. (2012) 135
C.1 Performance of the micrometeorological system in determining N_2O gradients 135
C.2 Frequency distribution of ΔN_2O 135

C.3 Diurnal variation of ΔN_2O 137

D Unit of nitrous oxide flux **139**

E Korman-Meixner footprinting model **141**

List of Figures

1.1 Flowchart showing nitrification and denitrification processes. Obtained from Farquharson and Baldock (2008). 2

1.2 Change in the total emission of individual gases from the 1990 level for New Zealand. Obtained from Sweeney et al. (2011). 3

2.1 Left: 100 mm diameter machined PVC ring provides a semi-permanent collar as a receptacle for a CO_2 flux chamber; right: 300 mm diameter static chamber with removable lid for N_2O measurement, designed by Landcare Research. From Harvey et al. (2008a). 12

2.2 The 10 m instrumented tower of 2011 campaign. 22

2.3 The nitrous oxide gas inlets (shown by white lines) are fitted with the CSAT3 and LiCor 7500 of 2010 campaign. 22

2.4 A permanent eddy covariance tower at the paddock setup by NIWA in 2011 in the same field. 22

2.5 Two-year averages of (a) air temperature (°C), (b) average rainfall (mm), and (c) net radiation (MJm^{-2}) for the month of (Autumn) May and June and (Spring) September to November observed at the experimental site. 25

3.1 Topography of the area is shown with an approximate location of the field, marked with a red dot. This figure is modified from Sturman and Spronken-Smith (2001). 31

3.2 Field layout showing individual subplots (marked as A - E) and measurement stacks marked as 1-4. The blue half-circles are irrigator pathways. The location of the site (43.67°S, 171.58°N) is shown by a green box. 32

3.3 Wind speed (ms^{-1}) represented as a function of $u_\star$ (ms^{-1}) before and after filtration for autumn (a, c, e, g) and spring (b, d, f, h). Plots a - d are for the CSAT3 data, and plots e - h are for the Gill anemometer data. Red lines are the best fit linear regression lines. 36

3.4 Comparison of friction velocities from wind profile (cup anemometers) and sonic anemometer measurements for neutral cases ($|1/L| \leq 0.04$) of (a) autumn and (b) spring experiments. Red lines represent the linear fit between $u_\star$ from the CSAT3 and cup anemometer measurements. . 37

3.5 Histogram of inverse Obukhov length (1/L) for (a) autumn and (b) spring . The bin sizes are 0.01 m^{-1}. 38

3.6 Wind distributions for (a) the autumn and (b) the spring campaigns. Wind sectors are sub-divided based on wind speed (m s^{-1}). 39

3.7 Box-plot (a) showing variations in mean and standard deviation values of d_h^p in spring and autumn; the linear fit between the filtered d_h^p from CSAT3 and Gill for (b) autumn and (d) for spring; and the linear fit between the filtered $\overline{w'T'}$ from the CSAT3 and the Gill for (c) autumn and (e) spring. 41

3.8 Daily mean N_2O fluxes from control subplots for the autumn experiment. Diffusivities from the CSAT3 and Gill anemometers are used with the parameterization, represented as subscript 'p', and thermal approach, represented as subscript 't'. Grazing periods are shown by rectangles. The daily mean flux values between 17 - 28 May are considerably higher than the average value of the entire period. Possible reasons may include the effect of grazing or sudden bursts of N_2O as mentioned in Harvey et al. (2008b). 44

3.9 Same as Figure 3.8, but for the spring experiment with the addition of an irrigation period. 46

3.10 Scatter-histogram of flux values represented as a function of the stability parameter (1/L). Green circles are fluxes from the parameterization method and red circles are fluxes from the thermal method. 49

3.11 The relative error in d_h^p, $\delta d_h^p/d_h^p$, for 1/$L \geq 0$ shown as a function of (a) inverse Obukhov length (1/L) and (b) $u_\star$ for autumn from both CSAT3 and Gill observations. A fitted pdf of the relative error in d_h^p is shown in the lower panel (c). 54

3.12 Relative error in d_h^p for 1/$L < 0$ shown as a function of (a) 1/L and (b) $u_\star$ for autumn, obtained from both CSAT3 and Gill observations. A fitted pdf of the relative error in d_h^p for 1/$L < 0$ cases is shown in the lower panel (c). 56

3.13 The upper panel shows the scaled relative error in k_h^t as a function of ΔT with the histogram of observed ΔT at the corner. The lower panel shows the scaled relative error in k_h^t as a function of $\overline{w'T'}$ with the histogram of the observed $\overline{w'T'}$. Observed values are from the autumn experiment. 58

3.14 The left upper-panel (a) shows the histogram of $\delta d_h^p/d_h^p$ for $1/L \geq 0$ and right upper-panel (b) panel shows the same for $1/L < 0$ cases. Bin size for both the histograms is 0.0078. The lower panel (c) shows the pdfs of the error anomalies for different stability cases. 60

3.15 Histograms of the nitrous oxide concentration differences (ΔC_{N_2O}, ppb) are shown for the (a) autumn and (b) spring experiments. Variance of ΔC_{N_2O} is shown in (c) as a function of 1/L (m^{-1}) for both autumn (blue squares) and spring (green circles). The vertical and horizontal bars in (c) are the standard deviations. 61

4.1 Layout of the measurement field showing subplots A-E. EC-1 is the location of the CSAT3 anemometer, EC-2 is the location of the Gill anemometer, G-1 to G-4 are the FG gas intake positions. 68

4.2 (a) The locations of 30/20 minute f_p^{max} from the EC-1/G2 measurement mast for only the N-NE wind directions (left panel for autumn and right panel for spring), (b) The γ values for subplots for only the N-NE wind regime at the EC-1/G-2 mast. Upper panel is for autumn and lower panel is for the spring campaign. 76

4.3 The $\gamma_{outside}$ values of both autumn and spring are plotted for (a) a neutral atmosphere ($|1/L| < 0.04$) and (b) a stable atmosphere ($1/L > 0.1$) using measurements at masts EC-1 and EC-2. Similarly, $\gamma_{outside}$ values of both autumn and spring are plotted for (c) N-NE and (d) N-NW and S-W wind regimes irrespective of stability and using measurements at masts EC-1 and EC-2. 78

4.4 Emission rates ($ER^{A,C}$) and observed flux values (F^{obs}) in gN_2O-N.ha^{-1}.day^{-1} are represented as functions of inverse Obukhov lengths ($1/L$) in m^{-1} for (a-b) autumn and (c-d) spring campaigns of subplots A and C, respectively. 80

4.5 Comparison of the filtered model predicted z_0 values at the G-2 and G-3 masts with observations for the (a) autumn and (b) spring campaigns. The observed values of z_0 were obtained from the profile measurement. 81

4.6 Comparison of the footprint fraction values obtained from the analytical footprint model and the bLs model for subplot A of (a) autumn and (b) spring experiment. The observed mean and standard deviation of errors between the two footprint fractions are shown in the bottom panels for respective seasons. 85

4.7 Comparison of emission rates from numerical method ($ER_{F^0_{eqn}}$) and bLs model (ER_{bLs}) for subplot A of autumn (shown in blue circles) and spring (shown in green squares) campaign. The red and blue lines indicate the fitted linear regression between $ER_{F^0_{eqn}}$ and ER_{bLs}. The intercept, slope and correlation coefficient (r) values for each campaign are shown inside the textboxes. 86

5.1 Field activity for the (a) autumn and (b) spring campaign is shown with the daily total rainfall. 'F' and 'D' represents those dates when fertilizer and DCD were applied. Grazing days are marked with the rectangles. The irrigation period for the spring campaign is shown with a dotted rectangle. Heights of these rectangles do not provide any information. 92

5.2 Daily mean nitrous oxide flux values (mean $\pm$ SE) for (a) Pre (13-19 September, 2010) and (b) post (23-29 September, 2010) grazing are compared between subplot A and B of spring experiment. Blue lines are for flux values using CSAT3 diffusivity and red lines are from Gill diffusivity. 94

5.3 Daily mean nitrous oxide fluxes for all the subplots from the (a) autumn and (b) spring experiments. Panels (1) and (2) indicate flux values using transfer coefficients from the CSAT3 and Gill measurements, respectively. Heights of these rectangles do not provide any information. Comparatively high daily flux values were observed for all the subplots during 17 to 28 May of autumn campaign and has also been shown in Figure 3.8. 96

5.4 Panel (a) shows the total rainfall of each day after DCD application. Changes in the daily mean N_2O flux values (mean$\pm$SE) in gN_2O-$N.ha^{-1}.day^{-1}$ are compared for all subplots of the autumn experiment after DCD application. Panels (b) and (c) show N_2O flux values from CSAT3 and Gill measurements, respectively. 97

5.5 Same as Figure 5.4, but for the spring experiment. 98

6.1 Field layout of the spring 2011 campaign. T-1 is the approximate location of the 10 m tower shown with a red dot. The N_2O gas measurement inlets are shown with white dots and represented by T-2. T-3 shows the location of the SODAR. The yellow rectangle is the boundary of the extended field. The red rectangle shows the experimental paddock. The background field image was retrieved from Google Earth on 1 December, 2012. 110

6.2 (a) Average wind speed (m s^{-1}) profiles from SODAR data are shown for day (upper panel) and night time (lower panel). Observations for the period of 16 to 25 Sept. are used to produce this diagram. Figures (b) and (c) show the wind direction for day and night time, respectively, obtained from the 10 m mast. Wind sectors (shown in different colours) are subdivided based on wind speed (m s^{-1}). 112

6.3 Observed averages of the profiles of (a) TKE (m^2 s^{-2}) and (b) TKE dissipation rate (m^2 s^{-3}) from SODAR data. The σ_w observations (obtained with a 15 min interval) from the SODAR are used with Equations 6.4 and 6.5 to compute TKE and TKE dissipation rate. The term 'average of averages' signifies the day-time averages of each day which are further averaged over 10 day period of the experiment. The green triangles and blue dots are for night and day time periods, respectively. The horizontal bars are showing the standard deviations. . 113

6.4 (a) Comparison of ϵ_0 values ($m^2 s^{-3}$) from the parameterization method (x-axis) and observations from SODAR (y-axis). ϵ_0^{param} is obtained from the sonic anemometer observations and using Equation 6.1. ϵ_0^{sodar} is obtained using σ_w from SODAR measurements and using Equation 6.5. The linear fit is shown with a red line. The y and x variables in the equation are the y and x axis parameters. (b) Comparison of u_ϵ (m s^{-1}) with $u_\star$ (m s^{-1}) values. u_ϵ is obtained using Equation 6.3. The blue dotted line is the linear fit through origin. 114

6.5 Comparison of the CBL depths (z_i) with the PBL heights obtained for each class of data described in Table 6.1. The mean z_i values with normalized standard deviations are shown by blue bars, whereas, the mean PBL heights with normalized standard deviations are shown by green bars. 116

6.6 The normalized vertical velocity spectra multiplied with respect to (a) $(\epsilon_0 z)^{-2/3}$ and (b) $(\epsilon_0 z_i)^{-2/3} \times (z/z_i)^{-5/3}$. The velocity scale $(\epsilon z)^{-2/3}$ of (a) has been obtained from the MNL model and found to represent the slope of -2/3 of inertial subrange well and collapses well near the peak. The velocity scale of $(\epsilon_0 z_i)^{-2/3} \times (z/z_i)^{-5/3}$ is also obtained with the MNL model with marginal modification. 118

6.7 The normalized temperature spectra multiplied with respect to (a) $(\epsilon_0 z)^{2/3} \times H_0^{-2}$ and (b) $\epsilon_0^{2/3}(z_s z)^{1/3} \times H_0^{-2}$. The vertical dashed lines of (a) and (b) are obtained from the MNL model. The bold vertical lines of (a) and (b) are the spectral averages. 120

6.8 The normalized heatflux co-spectra multiplied with respect to (a) H_0^{-1} and plotted against $z_i^{1/2} z_s^{1/2}$; (b) H_0^{-1} and plotted against $z_i^{1/4} z_s^{1/4} z^{1/2}$. The vertical line of 6.8(a) shows the peak location of the T spectrum from McNaughton et al. (2007), whereas, the vertical line of 6.8(b) shows the average peak location of all the classes at a normalized wavenumber 5.6. 121

C.1 (Autumn) ΔN_2O measurement under neutral conditions (Stability Parameter $|z/L|$ = 0.01) on 25/5/2010 12:30-13:00. (a) 100 individual 18 s gradient determinations (grey lines), means at each 0.1 s measurement interval (blue lines) and average of blue lines (red dashed line) during valid measurement interval between each pair of vertical blue solid lines; (b) time series of concentration and (c) measured gradients over the entire measurement interval (1800 s). Histograms of individual 0.1 s N_2O determinations for the (d) upper inlet and (e) lower inlet. (f) Histogram of the 100 determined gradients (f) the black dashed line is the zero concentration gradient and the red line is the gradient determined from the difference between the averaged concentrations depicted by the red lines in plot (a). The gradient for this period is 0.163$\pm$0.041 ppb, a difference that is significant at the P$<$1% level. The windspeed was 3.5 m/s and $u_\star$ = 0.22 m/s. (Spring) ΔN_2O measurement under stable conditions on 10/6/2010 00:00-00:30. The gradient for this period is 0.920$\pm$0.062 ppb, a difference that is significant at the P$<$1% level. The wind speed was 1.6 m/s, $u_\star$ = 0.03 m/s, and z/L = 1.01 (stable). 136

C.2 Frequency distribution (left) and cumulative frequency distribution (right) of all measured gradients. The grey line on panel (b) indicates that 21.7% of ΔN_2O values were less than 0.088 ppb, which is the P<1% resolution limit for the Autumn Experiment. Similarly, the black line indicates that 15.6% of ΔN_2O values were less than 0.066 ppb, which is the P<1% resolution for the Spring Experiment. The magenta line indicates that 10.0% of ΔN_2O values were less than $\Delta N_2O min_{best est}$ (which is 0.049 ppb). 137

C.3 Frequency distribution of gradient observations for the autumn and spring experiments. 138

C.4 Diurnal variability in N_2O during the Autumn (left panel) and the Spring (right panel) Experiments. 138

List of Tables

2.1 Sources of error in eddy covariance measurements and appropriate corrections (adapted from Burba and Anderson (2010)) 21

2.2 Advantages and disadvantages of techniques of flux estimation, modified from Harvey et al. (2008a). 23

3.1 Number of observations available for diffusion/diffusivity parameters (d_h^p, k_h^t) in different stability classes based on 1/*L*. 42

3.2 Mean $\pm$ Standard Error of N_2O flux values in $gN_2O\text{-}N.ha^{-1}.day^{-1}$ for autumn is summarized. Total number of observations is shown in parenthesis and mean values are computed over the total number of observations. 45

3.3 Mean $\pm$ Standard Error N_2O flux values in $gN_2O\text{-}N.ha^{-1}.day^{-1}$ for spring. Total number of observations is shown in parenthesis and mean values are computed over the total number of observations. 47

3.4 Mean uncertainty in the diffusivity parameter k_h^t for $\delta\overline{w'T'} = 0.0001$ m s^{-1}°C and $\delta\Delta T$ = 0.005 °C. $< |\frac{\delta\overline{w'T'}}{\overline{w'T'}}| >$ and $< |\frac{\delta\Delta T}{\Delta T}| >$ represents the mean relative error in the heat flux and temperature difference term. 53

3.5 Mean uncertainty in the diffusivity parameter d_h^p for $1/L > 0$ cases for $\delta u_\star = 0.01$ m s^{-1} and $\delta L = 0.5$ m are shown here. $< |\frac{\delta u_\star}{u_\star}| >$ represents the mean relative error contribution from $u_\star$ and $< |\frac{\delta L}{L}| >$ represents the mean relative error from *L*. 55

3.6 Mean uncertainties in the diffusivity parameter d_h^p for $1/L < 0$ cases are shown here and are obtained using $\delta u_\star = 0.01$ m s^{-1} and $\delta(C_4 - C_6 ln(\frac{1+y_2}{1+y_1})) = 0.1$ m. Term $< |\frac{\delta u_\star}{u_\star}| >$ signifies the mean relative error from $u_\star$ whereas $< |\frac{\delta(C_4 - C_6 ln(\frac{1+y_2}{1+y_1}))}{(C_4 - C_6 ln(\frac{1+y_2}{1+y_1}))}| >$ represents the mean relative error from the stability dependent term. 56

4.1 Percentage contributions of the principal source areas (PSA) to fluxes measured at the EC-1/G-2 location are shown for different wind regimes. Mean values of peak distance of the footprint function, $\overline{f_p^{max}}$, are also shown. 77

4.2 Arithmetic mean $\pm$ standard error of the selected measured flux and emission rate of N_2O in $gN_2O\text{-}N.ha^{-1}.day^{-1}$ for the autumn and spring experiments are denoted by 'arithmetic'. Emission rates are estimated using F^0 from Equation 4.9 ($ER_{F^0_{eqn}}$). Observations were only used for this comparison where both measured flux and emission rate values were available. Hence, the mean $Flux_p$ values computed here can be marginally different than the values reported in Table 3.2 and 3.3. The total number of such observations is shown in parenthesis. 79

5.1 Comparison of flux values estimated using parameterisation (*p*) and thermal (*t*) methods from CSAT3 and Gill data. Mean $\pm$ Standard Error values of N_2O flux ($gN_2O\text{-}Nha^{-1}day^{-1}$) are shown for the autumn and spring campaigns. Total numbers of observations are shown in parenthesis. 95

5.2 Mean measured flux and emission rate values of N_2O in $gN_2O\text{-}N.ha^{-1}.day^{-1}$ for the autumn (9 days) and spring (12 days) experiment after DCD application on subplots B and D. The results are compared with the control plot C. $Flux_p$ values are from the CSAT3 anemometer observations as mentioned in Section 5.3.3. Emission rates are estimated using F^0 from Equation 4.9 of Chapter 4. High mean values of autumn than spring experiment for this selected period has been discussed in Chapter 3. 100

6.1 Description of the MLsp obtained according to the surface layer classification of 6.5.2.2. The standard deviations are provided in parenthesis. 116

Chapter 1

General introduction

1.1 Background

Emission of non-CO_2 greenhouse gases is believed to contribute substantially to global warming and nitrous oxide (N_2O) is one of the more potent non-CO_2 greenhouse gases in the context of agricultural anthropogenic emissions. The 100-year average global warming potential of N_2O is **310 time higher** than an equal mass of CO_2 (Crutzen et al., 2008). An estimated 6% of total greenhouse warming is contributed by N_2O and it is the fourth largest single contributor to positive radiative forcing of the atmosphere (Denman et al., 2007). Tropospheric N_2O is primarily inert, and therefore, the atmospheric residence time of N_2O is more than 100 years (Cicerone, 1989). However, it is a principal source of nitric oxide (NO) in the stratosphere and indirectly responsible for ozone depletion. The Ozone Depleting Potential (ODP)[1] of N_2O is similar to some of the chlorofluorocarbons and it has been estimated by Ravishankara et al. (2009) that the N_2O emission of the present time is the single most important ozone-depleting contributor and will remain so for the 21st century. A global scale relationship between the amount of nitrogen fixed by the biogeochemical and atmospheric processes in the terrestrial biosphere, and the total nitrogen released in the atmosphere through emission of N_2O has been investigated by Crutzen et al. (2008). Estimates show that for both pre-industrial period and recent times the concentration growth of newly fixed N to N_2O has an overall conversion factor of 3-5%, and the atmospheric mixing ratio of N_2O has changed from 270 nmol/mol of the pre-industrial period to 315 nmol/mol of recent times. The atmospheric concentration of N_2O is increasing at an annual rate

[1] ODP of a chemical compound is defined as the ratio between the amount of stratospheric ozone destroyed by the release of a unit mass of that chemical at Earth's surface to the amount destroyed by the release of a unit mass of chlorofluorocarbon 11, ($CFCl_3$) (Ravishankara et al., 2009).

of 0.2-0.3% (Prather et al., 1995) and 80% of all anthropogenic sources of N_2O is contributed by the agricultural sector (Saggar et al., 2010).

Predominantly, nitrous oxide gas is produced in soil during the microbiological processes of nitrification and denitrification. Nitrogen compounds are added to the soil in the form of animal excreta or chemical fertilizers of which the ammonium (NH_4^+) and nitrate (NO_3^-) ions undergo chemical changes and produce N_2O gas as a by-product. The biological oxidation of the NH_4^+ ion to NO_2^- is called nitrification and the reduction of the NO_3^- ion in the presence of nitrate reductase is the denitrification process. N_2O gas is mostly produced during the denitrification process. A flowchart of nitrification and denitrification is shown in Figure 1.1. The microbiological processes are affected by a number of soil and climate factors, such as soil pH, enzyme activity, nitrate concentrations, rainfall/irrigation, water-filled pore space (WFPS), and soil temperature and moisture. The meteorological and land surface conditions, particularly rainfall, can change the soil moisture and soil oxygen content to a large extent, which ultimately leads to variation of N_2O production (Theobald et al., 1995; McTaggart et al., 1999; Smith and Dobbie, 2001).

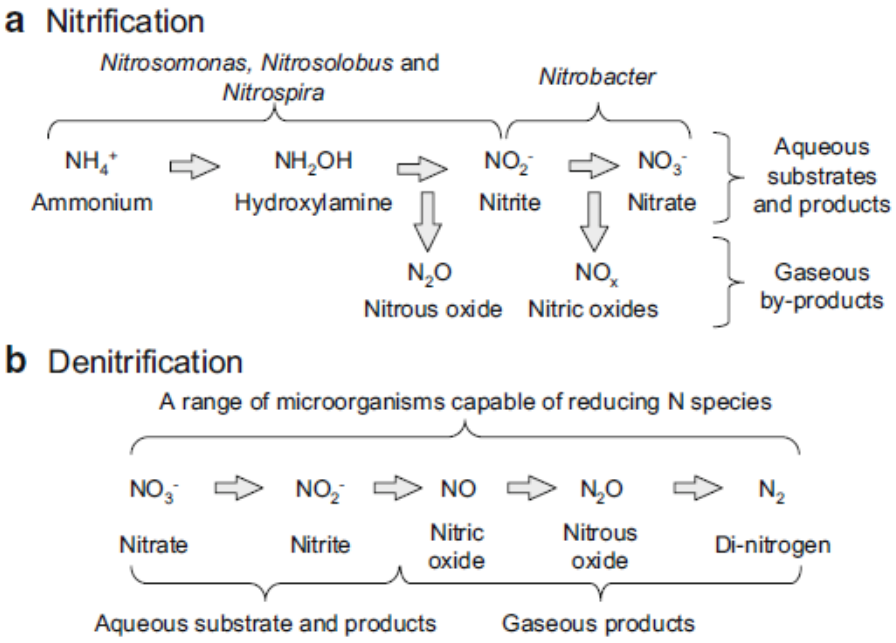

Figure 1.1: Flowchart showing nitrification and denitrification processes. Obtained from Farquharson and Baldock (2008).

Since 1990, overall greenhouse gas emissions, including CO_2 and most of the non-CO_2 chemical species, have been increasing for New Zealand. Figure 1.2 shows the

change in the total emission of individual gases from 1990's levels. A 23.0% enhancement in the emission rate of N_2O has been observed in New Zealand from the 1990's level, which is the second largest enhancement after CO_2 (Sweeney et al., 2011). The largest source of N_2O in New Zealand is the green pastures where livestock are produced, and in 2009 alone, 94.6% of the total emission of N_2O was contributed by the agricultural sector. Such a large growth in the emission of N_2O is attributed to the fivefold increased use of nitrogen fertilizers in agricultural fields and to increased animal excreta (Sweeney et al., 2011). Therefore, N_2O is one of the primary concerns for mitigation.

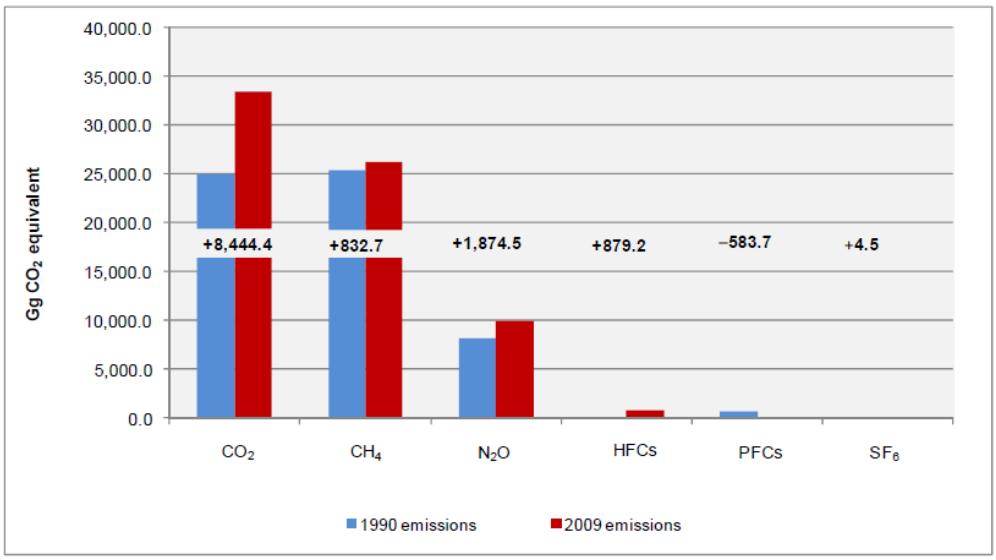

Figure 1.2: Change in the total emission of individual gases from the 1990 level for New Zealand. Obtained from Sweeney et al. (2011).

As a part of the United Nations Framework Convention on Climate Change (UNFCCC), New Zealand is required to report the annual greenhouse gas emissions and removal. Therefore, proper measurement and mitigation strategies for individual greenhouse gases are to be developed. A Sustainable Land Management and Climate Change (SLMACC) plan was developed by the Government of New Zealand in 2007 to address issues such as, (i) the impact of and adaptation to climate change, (ii) reduction of greenhouse gas emissions and (iii) exploring business opportunities from climate change (Ministry for Primary Industries, 2012). As part of the SLMACC plan, a number of different projects involving measurement and mitigation of non-CO_2 greenhouse gases are being implemented. In particular, several measurement and mitigation exper-

iments have been carried out for N_2O using chambers. However, a top-down paddock scale measurement system was seldom implemented and very few micrometeorological experiments have been carried out in New Zealand to measure N_2O flux from paddocks (Kelliher et al., 2002; Harvey et al., 2008b; Saggar et al., 2010). The advantage of the micrometeorological setup over the chamber measurement is that the spatially integrated fluxes can be measured using this setup continuously for long time periods. Furthermore, most of the previous studies investigating the effect of the nitrification inhibitors on the N_2O emission were conducted using chambers or lysimeters (Di and Cameron, 2002b,a, 2003; Di et al., 2007; Saggar et al., 2008), thereby neglecting the larger meteorological effects. Therefore, the 'Agricultural Emission Group' of National Institute of Water and Atmospheric Research Ltd. (NIWA), along with University of Canterbury, New Zealand, has undertaken an independent measurement project entitled "Verification of the management and mitigation of agricultural nitrous oxide emissions at the Paddock to Regional Scale" using the flux gradient (FG) - eddy covariance (EC) micrometeorological approach. The project is funded by the SLMACC programme of Govt. of New Zealand and this PhD research is a part of it. Although the principal objective of this project is the development and implementation of a paddock-scale N_2O measurement system, this PhD research is mostly focused on the theoretical aspects of the micrometeorological setup and addresses key issues such as uncertainty in the flux measurement, source area contribution to the measured flux values, and the effect of mitigation on N_2O flux reduction. Brief backgrounds of these issues are provided in the following paragraphs.

Error or uncertainty estimation of the measured flux value of a coupled FG-EC system is typically important. This is because in a coupled FG-EC system of flux estimation, large error can accumulate in the final flux value primarily from three different sources: (i) measurement error, (ii) systematic error and (iii) footprint heterogeneity error, of which the largest contribution to the total uncertainty is predominately produced from the measurement error (Hollinger and Richardson, 2005). Since the measured flux from the FG-EC approach is dependent on the eddy diffusivity or transfer coefficients estimated at the measurement height, a major source of error in the flux value is associated with the errors in the measured surface-layer variables that are used to estimate the transfer coefficients. Although considerable work has been done to estimate systematic error and random error propagation through EC measurements (Goulden et al., 1996; Vickers and Mahrt, 1997; Mahrt, 1998), this study provides an alternative numerical method to estimate total relative random error in the measured flux of a

FG-EC system involving variables contributing to the standard Monin-Obukhov flux-gradient calculations. The mathematical method is developed for the N_2O concentration and, final error values include error in the measured N_2O concentration. However, the described method is generic and can be applied to any other species measured using a similar approach. Details are provided in Chapter 3.

As mentioned earlier, this research is also focused on estimating the source area emission rate from the measured flux value and, therefore, includes footprint analysis. The question addressed in this study is 'how does one obtain an actual source area emission rate for a plot when multiplot flux measurement is carried out over a heterogeneous field'. A heterogeneous field is assumed to be differentiated by mitigative treatments or biogenic characters. Such multi-plot measurements from heterogeneous field are becoming common. The problem addressed in this study is relevant as considerable uncertainties can be induced in the measured flux as a result of treated and untreated plot representation. Therefore, an inverse footprint fraction approach is developed here to compute the actual emission rate of a particular field where measurements are carried out among differently mitigated plots. The footprint fractions are obtained from an analytical footprint model of Kormann and Meixner (2001) and Neftel et al. (2008) and the emission rates obtained from the proposed mathematical method are ascertained with values obtained from a backward Lagrangian stochastic model derived by Flesch et al. (1995).

As a third objective and an extension of the verification process of the proposed micrometeorological setup for N_2O flux measurement, effects of grazing and mitigation on the measured flux values are also explored. It is a well established notion that cattle grazing enhances the emission rate of N_2O from green pastures of New Zealand (Saggar et al., 2004; Luo et al., 2008b) and a nitrification inhibitor, such as Dicyandiamide (DCD), reduces the N_2O emission rate irrespective of season (Di and Cameron, 2002b,a, 2003). However, most of the reports confirming that notion are based on the measurements carried out using chambers and Lysimeters which mostly ignore the atmospheric diffusion and meteorological effects. Since the proposed micrometeorological setup includes atmospheric surface layer processes during flux measurement, the established notion of 'emission rate enhancement due to grazing' and 'emission rate degradation due to mitigation' will be explored in Chapter 5.

Since this research is focused on the application of micrometeorological methods of flux estimation, a proper understanding of atmospheric surface layer turbulence is necessary. The fundamental concept of the FG-EC measurement setup, as used in this

research, is built upon the validity of the Monin-Obukhov similarity theory (Monin and Obukhov, 1954). This theory explains the surface layer turbulence properties based on some derived length scale and velocity properties, such as the Obukhov length (L) and friction velocity ($u_\star$). Since the field experiments of Kaimal et al. (1972, 1976), numerous other experiments have established the Monin-Obukhov similarity theory as a standard model of the atmospheric surface layer. However, some discrepancies have been noted in the fundamental understanding of this turbulence model (Kader and Yaglom, 1990; McNaughton, 2004b; McNaughton et al., 2007). Consequently, a few alternative turbulence models have been proposed (Hogstrom et al., 2002; McNaughton et al., 2007). Some of these, particularly the turbulence model and the new scaling parameters proposed by McNaughton et al. (2007) and Laubach and McNaughton (2009) appear to be closer to reality, as the spectra produced using the new scaling properties were found to fit well in the discontinuous regions of the spectra mentioned by Kaimal et al. (1972, 1976). Therefore, in the penultimate chapter of this thesis, the turbulence model of McNaughton et al. (2007) and Laubach and McNaughton (2009) is studied using the field observation data collected during the nitrous oxide measurement campaign. Field observations are directly used for the first time to deduce the new variables of the McNaughton model of turbulence, such as dissipation velocity (u_ϵ) and surface layer height (z_s), and compared with the traditional surface layer length and velocity scales such as, $u_\star$ and L. Finally, spectra of surface wind components, temperature and heat flux are analyzed.

In short, the overarching aim of this thesis is to verify a micrometerological setup of nitrous oxide flux measurements from the green pastures of Canterbury, New Zealand. This verification procedure is performed by (i) comparing the measured the flux from this setup with already existing values in literature, (ii) estimating error propagation in the measured flux values, (iii) investigating flux footprint effect on the measured flux and by (iv) assessing the effect of mitigation and grazing effects on the measured flux. These objectives are addressed in different chapters of this thesis. Furthermore, during the verification procedure of the FG-EC technique, it has been also realized that the fundamental model of atmospheric surface layer turbulence should be addressed from a nonlocal parameterization point of view and therefore, a new turbulence model has been studied in Chapter 6 in comparison to the Monin-Obukhov theory as an alternative.

1.2 Research objectives

This research thesis has two broad objectives: first, verification of a micrometeorological approach to N_2O flux measurement, that involves detailed investigation of issues such as the uncertainty in measured flux, identification of source areas and their contributions to the measured value, and effects of mitigation; and second, investigation of an alternative surface layer turbulence model for a convective atmosphere, involving analysis of the turbulent spectra of atmospheric surface layer variables. Within this broad framework specific research objectives are as follows:

- **Verification of a flux gradient - eddy covariance micrometeorological technique of nitrous oxide flux measurement**

  The effectiveness of a micrometeorological set up has been evaluated over a commercial paddock in Canterbury, New Zealand. Nitrous oxide flux has been estimated using the transfer coefficients from a parameterization and a thermodynamic approach to FG-EC micrometeorological measurement and compared.

- **Analysis of uncertainty in the nitrous oxide flux values**

  Error sensitivity analysis has been performed based on some newly derived algebraic relationships of random relative error of the eddy diffusivity. This study investigates the total error/uncertainty variance in eddy diffusivities as a cumulative effect of uncertainties in their constitutional variables. A Monte-Carlo type approach has been followed to obtain probabilistic estimates of random relative error. Subsequently, errors in the concentration gradients are estimated and final error variances are produced for flux values in stable and unstable atmospheres.

- **Identification of the source area of N_2O emission and estimation of actual emission rates**

  Two important objectives of this study are to: (i) investigate the effect of wind distribution and atmospheric stability on the footprint functions and the emission rate; and (ii) determine the actual flux density of N_2O from the individual control subplots. This study aims to address the problem of identifying the actual surface emission rate from a specific plot when heterogeneous multi-plot flux measurements are carried out. Therefore, a new inverse footprint fraction approach is proposed.

- **Effect of grazing, fertilization and mitigation on the N_2O flux emission rate**

  The study is aimed at verifying the effect of mitigation on N_2O emission rate using measured flux values from a FG-EC system, as such a measurement system has a larger spatio-temporal scale with enhanced degrees of freedom than a non-flow through non-steady state chamber in terms of atmospheric processes. Since the atmospheric flow properties are not constrained in a FG-EC system, atmospheric processes incorporated in such a system are better represented than the traditional chamber measurement. Furthermore, the effects of grazing and irrigation on the N_2O emission rate have also been explored.

- **Investigation of a new model of surface layer turbulence**

  The McNaughton-Laubach (ML) model of convective boundary layer turbulence is investigated. The ML-scaling parameters have been deduced from the profile values of turbulent kinetic energy (TKE, b) and TKE dissipation rate (ϵ) of a CBL. The profile values of b and ϵ have been derived using the wind profile observations from a SODAR and a parameterization scheme provided in Kramar and Kouznetsov (2002). Finally, the new ML-scaling properties are verified for this case study. This investigation is aimed at enhancing the understanding of CBL turbulence so that an alternative flux gradient model can be developed in the future.

1.3 Thesis outline

Chapter 2 - Overview of measurement techniques : As mentioned in its heading, this chapter overviews the available techniques of nitrous oxide flux measurement along with the basic operating principles. Some of the advantages and disadvantages of each measurement technique are also discussed. A concise review is also added for flux footprint methods, although, background relating to turbulence theory is provided in the penultimate chapter.

Chapter 3 - Measurement of nitrous oxide flux and assessment of error propagation : This chapter describes the first two research objectives mentioned above, providing detailed derivations of the theory of flux gradient measurement along with the uncertainty measures. Nitrous oxide flux values are estimated for all the subplots and compared.

Chapter 4 - Estimation of source area emission rates using footprint methodologies : The research objective mentioned in bullet three of the previous section, addressing the flux footprint problem, is described here along with brief descriptions of the footprint models used for the study.

Chapter 5 - Assessment of grazing and mitigation effects on nitrous oxide flux : The effect of mitigation on the nitrous oxide flux value is described in this chapter. A brief overview of previous reports and experiments of N_2O mitigation are provided in the 'Introduction' section.

Chapter 6 - Analysis of the spectral properties of turbulence and some alternative scaling parameters : This chapter verifies a newer approach to atmospheric boundary layer turbulence. The 'Introduction' section will provide some basic classification of atmospheric boundary layer. The new model for the atmospheric boundary layer turbulence is briefly described in the 'Theory' section. Results and implications are described at the end.

Chapter 7 - General conclusion : The general conclusion section briefly summarizes the findings of this research, recognizes any limitations and provides some insights about some possible future work.

This thesis is based on the theory and application of micrometeorological techniques for greenhouse gas estimation. Therefore, the immediate beneficiary of this research outcome would be future policy makers and researchers in this field. The analytical graphs and figures are all produced using the University of Canterbury licensed version of MATLAB (R2011b). Some of the results of this study have been compiled in a report to the Ministry of Agriculture and Forestry, New Zealand via NIWA.

Chapter 2

Overview of measurement techniques and a brief climatology of the experimental field

2.1 Introduction

Presently, approaches for biogenic N_2O flux measurement either involve use of small scale non flow through non-steady state chambers, or a spatially integrated measurement technique using micro-meteorological instruments. These two different approaches also include different instrumentation and application schemes. In this chapter, some of the instrumentation and application schemes suitable for agricultural N_2O flux estimation will be discussed. Furthermore, a brief climatology of the experimental field used for this study will be provided. This overview chapter is not exhaustive and only a few of the instrumentation and measurement approaches are described here of which some are used for the experiments described in this study.

2.2 Non flow through non-steady state chambers

Non flow through non-steady state chambers (described as 'chambers' hereafter) are the most convenient and most commonly used tools for measuring trace gas fluxes from a particular surface and the majority of the agricultural nitrous oxide flux data reported in the literature have been obtained using such chambers (Bouwman et al., 2002). Therefore, most of the mathematical modeling techniques used for N_2O flux prediction from soil, such as by Li (2000), Delgrosso et al. (2005) and Saggar et al.

(2004), are validated using chamber measurements. Chamber measurement of biogenic fluxes is an old technique (Lundegardh, 1926) and several methodological improvements have been made in chamber design and implementation procedures in the last few decades (Matthias et al., 1980; Smith and Conen, 2004). Some of these enhancements and implementation protocols can be found in Rochette and Hutchinson (2005) and De Klein et al. (2011).

The operating principles of chambers are simple and chambers are highly flexible and portable. Chambers are placed over a soil surface and the overlying air motions are controlled in such a way that the fluxes of gases lead to a measurable change in the gas concentration inside the chamber volume over time. The most important physical characteristics of chambers are: (i) the shape and dimension of the area enclosed, and (ii) the volume of the chamber. Rectangular or cylindrical chambers are used with a wide range of volumes and dimensions, and Figure 2.1 shows two such cylindrical chambers with different diameters and dimensions of area covered.

Figure 2.1: Left: 100 mm diameter machined PVC ring provides a semi-permanent collar as a receptacle for a CO_2 flux chamber; right: 300 mm diameter static chamber with removable lid for N_2O measurement, designed by Landcare Research. From Harvey et al. (2008a).

2.2.1 *Operating principles*

Chambers are mainly categorized as open or flow-through chambers and closed or non-flow-through chambers. In open chambers, a constant flow of outside air is maintained within the chamber head space, whereas in a closed chamber very little or no air is exchanged with the outside atmosphere.

In an open chamber, concentrations are measured when air is entering the head space of the chamber, as well as when it is leaving. The surface flux density F_g (kg m^{-2} s^{-1}) is calculated from the relationship (Denmead, 2008):

$$F_g = v(\rho_{g0} - \rho_{gi})/A \tag{2.1}$$

where v (m^3 s^{-1}) is the volume flow; ρ_{g0} (kg m^{-3}) is the gas concentration in the air leaving the chamber; ρ_{gi} (kg m^{-3}) is the gas concentration in the air entering the chamber; and A (m^2) is the surface area covered by the chamber. A wind tunnel is an example of an open chamber where the airflow simulates the external aerodynamic conditions.

In a closed chamber, there is very little or no replacement of air in the head space of the chamber, and gas concentration increases continuously. The rate of gas increase is monitored and the flux density F_g is calculated using the following relationship (Denmead, 2008):

$$F_g = (V/A)(\partial\rho_g/\partial t) \tag{2.2}$$

where, ρ_g is the concentration of the gas in chamber and A is the same as in Equation 2.1. V is the volume of the head space and t is time. A closed chamber can be of two types: a static chamber and a dynamic chamber. In a static chamber no air circulation takes place between the sensor and the chamber and a series of samples are removed from the head space volume at a specific time interval. Collected samples are analyzed at a later stage using gas chromatography. In a dynamic chamber, the concentration change is continuously monitored in the head space volume. Dynamic chambers are more sophisticated than static chambers as the air is circulated in a loop between the head space and the gas analyzer.

The best practices of non-flow-through chamber measurement for N_2O flux from the pastures of New Zealand were provided in De Klein et al. (2003) where two different methods of chamber deployment were adopted for laboratory and field conditions. These two chamber deployment methods were mostly differed by issues such as cham-

ber location, sampling interval and, nature of the chamber head-space. However, the nature of the non-flow-through chamber deployment and gas sampling techniques can vary from location to location as Skiba et al. (1998) has used slightly different method for N_2O flux measurement than De Klein et al. (2003), which was adopted for the GREENGRASS project in Europe. Automated and open path chambers are also used for N_2O flux measurement and usage of a series of four automated static chambers can be found in Parkin (2008).

2.2.2 Advantages and disadvantages

Chambers have both advantages and disadvantages. The benefit of using chambers in the field includes their limited power requirements, so that chambers are cost effective. Conceptually, chamber application is simple, and operation of chambers in the field is straightforward. Chambers are also portable and easy to deploy in the field and the chamber placement in the field can be controlled. The number of variables to control in a chamber is limited. In the case of a dynamic chamber, the device can be used for continuous recording of emission data from a single site (Harvey et al., 2008a).

The main disadvantage of chamber measurement is the small area coverage of experimental sites which can lead to inaccuracy in measurements of some greenhouse gases, especially the emission of agricultural N_2O which is highly variable in space. Also, increasing gas concentration in the head space of the chamber affects the emission rates of gases from the area underneath, while chambers deployed in the field alter some meteorological variables at the field surface, such as radiation, rainfall and temperature. For a static chamber, the wind speed is altered, which leads to a change in the turbulence properties of the atmosphere above it, thus causing problems for flux estimation. Rochette and Eriksen-Hamel (2008) described a minimum set of criteria for reliable measurement of nitrous oxide flux using chambers.

2.3 Micrometeorological measurement techniques

Direct measurement techniques are an alternative approach to the chamber methods. Measurement of biogenic gases using the direct approach includes estimation of aerodynamic variables without affecting the turbulent properties of the atmosphere. Gas flux can be estimated using such techniques for longer time periods, as these techniques do not disturb atmospheric diffusion and turbulent properties. Different micrometeo-

rological techniques, such as (i) eddy covariance, (ii) flux gradient and (iii) the eddy accumulation methods, are used for biogenic N_2O flux measurements and some of the applications can be found in Mammarella et al. (2010); Kroon et al. (2010) and Harvey et al. (2008b). The integrated horizontal flux technique (IHF) is another possible approach to flux estimation, which can perform better than flux gradient and eddy covariance system during a small upwind and large crosswind measurement condition. Applications of the IHF technique for methane flux estimation from the paddocks of New Zealand can be found in Laubach and Kelliher (2004) and Laubach and Kelliher (2005). Brief theoretical descriptions of the eddy covariance and flux gradient methods are given in Section 2.3.1 and 2.3.2 as these methods are used in further experiments. Identification of the surface source area that contributes to the measured flux values, is also an important aspect of micrometeorological measurement, and hence, flux footprint estimation is necessary. Information from the footprint analysis of a particular field measurement can also be used to estimate the actual emission rate of a chemical species. Applications and theoretical concepts of some of these flux footprint methods are reviewed in Section 2.3.3.

2.3.1 Eddy covariance

Flux measurement using the eddy covariance (EC) method is one of the direct methods where no empirical constants are used (Businger, 1986), with few theoretical assumptions. However, the limiting condition for EC measurement is the *horizontal homogeneity*[1] of the surface and the *steady-state*[2] condition of the atmosphere. Since the EC method works on the principle of measurement of vertical transport of an entity, vertical flux is defined as $F=\overline{\rho_a ws}$, where ρ_a is density of air, w is the vertical wind speed, and s is the mixing ratio of the gas of interest. Using Reynold's decomposition, the vertical flux density can be represented as:

$$F = \overline{(\rho_a + \rho'_a)(w + w')(s + s')} \tag{2.3}$$

Equation (2.3) can be further simplified as $F=\overline{\rho_a}.\overline{ws} + \overline{\rho_a}.\overline{w's'}$ where the term $\overline{\rho_a}.\overline{ws}$ signifies the mean vertical flow which is assumed to be negligible for horizontally homogeneous terrain (Pattey et al., 2006b; Burba and Anderson, 2010). When the mean vertical wind speed (w) is not equal to zero and flux of a chemical species is measured

[1] Horizontal homogeneous surface will satisfy the condition $\partial/\partial x$=0; $\partial/\partial y$=0
[2] Steady-state atmosphere will satisfy the condition $\partial/\partial t$=0

in presence of simultaneous fluxes of sensible heat and water vapour, a *Webb correction* (Webb et al., 1980) is made to the flux estimation. Hence in short, measurement of the three-dimensional wind and the gas density are decomposed to mean and fluctuating components, and the covariance is calculated between the fluctuating component of the vertical wind and the fluctuating component of the gas concentration. The upward flux of the gas is proportional to the covariance. Fast response instruments are used for the measurement of w and ρ_g with sampling frequencies higher than or equal to 10 Hz and mean flux measurements are derived for periods of 15 minutes to 1 hour. A discussion on the appropriate time averaging periods for different applications can be found in Finnigan et al. (2003) and Foken and Nappo (2008).

Measuring devices required for EC applications are a sonic anemometer for wind measurement (*u, v and w* components) and a gas analyzing sensor that can measure the gas concentration (ρ_g) with high time resolution. Fast response gas analyzers are of two types: open and closed path. Open path analyzers are used for concentration measurements of the CO_2 and water vapour and are frequently used for eddy covariance measurements. Li-Cor 7500/7500A, 7700 are examples of CO_2/H_2O and CH_4 detecting open path infrared gas analyzers. These open path gas analyzers are high speed (between 60-10 Hz), low power consuming (10-15W in steady state) and high precision devices that can also work in harsh environmental conditions. These analyzers are easy to set up and data processing software such as *EddyPro*, *ECO$_2$S* and *TK2* are freely available.

Closed path analyzers are the alternative instruments used for gas concentration measurements. Apparatus such as the Campbell Scientific Inc. EC155 for CO_2/H_2O, and tunable diode lasers (TDL), such as the TGA-100/200 for radio carbon and N_2O measurements, are examples of closed path gas analyzers. Although these closed path systems are used for gas concentration measurements in the field, these devices are heavy, sensitive to slight disturbances in system set up, and expensive. Recently, a hybrid open-closed path EC instrument is available from Li-Cor (Li-7200) for CO_2/H_2O concentration measurements with much simpler application.

2.3.2 Flux gradient

Another alternative technique of greenhouse gas measurement is the flux gradient (FG) method. In this case, the vertical transport of gases in the surface boundary layer of the atmosphere is described by the equation (Garratt, 1992):

$$F_g = k_g(\partial\rho_g/\partial z) \tag{2.4}$$

Where the term k_g is the eddy or turbulent diffusivity of the gas of interest which is determined using local or first order closure analogous to the molecular diffusion approach, ρ_g is the concentration of the gas and z is height. F_g defines the flux density. The concentration gradient of the gas is obtained by measuring the concentration difference between two different heights, and no high frequency sensor is necessary for such estimation. The validity of the FG technique depends on Monin-Obukov similarity theory (Monin and Obukhov, 1954), while *horizontal homogeneity* and *steady state* atmospheric conditions are two important assumptions for this method. k_g, the eddy diffusivity, is determined from wind speed at a given height, aerodynamic roughness, and atmospheric stability. The Monin-Obukhov similarity theory along with flux gradient similarity are used to estimate k_g. A complete description of the method for estimation of eddy diffusivity is provided in Chapter 3.

The EC method is a direct technique of flux measurement, while the FG method is an indirect technique as it relies on Monin-Obukhov similarity theory. Many studies have been reported where the FG technique is combined with EC measurements for CH_4 and N_2O flux estimation (Laubach and Kelliher, 2004; Phillips et al., 2007; Mammarella et al., 2010; Saggar et al., 2010). An important issue about the combined FG-EC theory is that Monin-Obukhov similarity theory does not always satisfy the approximation of similarity in all the eddy diffusivities. Several studies have shown that the surface fluxes of a scalar, temperature and moisture can vary in different atmospheric conditions, particularly during the low frequency variations of wind or during a disturbed surface layer (McNaughton and Laubach, 1998; Laubach and McNaughton, 1998; McNaughton and Laubach, 2000; Smedman et al., 2007)[3]. Therefore, because of the debatable nature of the validity of Monin-Obukhov similarity theory, investigation of some alternative turbulence theories is necessary.

2.3.3 *Flux footprint models for source area estimation*

A footprint of the turbulence flux defines the spatial context of the flux measurements. The surface flux measurement of a chemical species or a scalar variable at a particular height and site does not represent the actual flux below the sensor, rather the conditions of the underlying surface upwind of the sensor are represented (Gash, 1986). This ef-

[3]Detailed discussion is provided in Chapter 6.

fective area of influence is represented as the *footprint area* and expressed as a transfer function (f_p) between the source area and the spatial extent and distribution intensity of a chemical species or scalar quantity over a domain *R*, as shown in Equation 2.5, where Q_η denotes the distribution intensity, η represents the measured value at location *r*, and *r′* denotes the separation distance between the measurement and forcing location (Pasquil and Smith, 1983).

$$\eta_r = \int_R Q_\eta(r + r') f_p(r, r') dr' \tag{2.5}$$

The measured quantity η can be different for different scalar quantities, chemical species, or bulk gradients, and different methods exist for the estimation of the flux transfer function, f_p. Common approaches for estimation of the flux-footprint include: (i) Eulerian analytical methods, (ii) numerical methods that includes large eddy simulations (LES), (iii) the backward Lagrangian stochastic (bLs) method, and (iv) the ensemble average of closure models.

The analytical flux foot-printing approach started with the application of the analytical solution of a 2-dimensional advection-diffusion equation. Although several 2-dimensional analytical solutions of the diffusion equation are available for idealized boundary layer conditions, a simple analytical solution for gas concentration was first applied by Gash (1986) at a measuring point (0, z) for infinite crosswind line sources situated at specific distances. This model assumed a neutral atmosphere with uniform wind velocity and the energy balance was not satisfied.

Later Gash's model was updated to a 2-dimensional flow flux footprint model by Schuepp et al. (1990) for a near-neutral atmosphere, specifically for weak thermal instability and large surface roughness (z_0), which was also the first differential flux footprint model. Schuepp's model was constructed with primitive assumptions and was too simple for non-neutral atmospheric applications, but the model was able to form the basis of an analytical footprinting method used by some of the sophisticated contemporary footprint approaches. Laubach and Kelliher (2004) have used a modified version of Schuepp's model for footprint estimation by including a stability parameter to allow for different atmospheric stratifications. Schuepp's model is simple and easy to apply, and is still used for comparison purposes.

A new footprint model combining the flux footprint function and surface source contribution was presented by Schmid (1994). This model was based on the works of Schmid and Oke (1990) and Schmid et al. (1991). Schmid's source area flux footprint model used the idea of continuous concentration distribution of a passive scalar from

a point source to a sensor at a definite measuring height. This approach was also able to distinguish between flux footprint and concentration footprint. The footprint function or the source weight function of Schmid's model provided information about the relative weights of individual sources. This footprint model was able to identify the most effective regions of the surface area influencing the flux signal. The model is also applied to non-neutral atmospheric condition and uses Monin-Obhukov similarity theory for defining atmospheric stability.

Another realistic analytical flux footprint model was developed by Horst and Weil (1994) for crosswind locations. The Horst and Weil (1994) model assumed that the flux footprint for a crosswind location will depend on a crosswind concentration distribution, and an approximate vertical concentration profile equation was used as an analogy of footprint function. Horst's model was extensively used for flux footprint estimation and a summary of the model can be found in Horst (1999). An exhaustive review of analytical flux foot-printing models can be found in Schmid (2002). Several different flux footprint models, predominantly based on the ideas of Schmid (1994) and Horst and Weil (1994), have been proposed since then and are used in different atmospheric conditions. Models developed by Kormann and Meixner (2001) used the power law of K-theory with Monin-Obukhov similarity theory for a non-neutral atmosphere. Examples of some other flux footprint models are the closure model of Sogachev and Lloyd (2004) and the parameterization model of Kljun et al. (2004).

The numerical simulations of flux footprinting methods include large eddy simulation (LES) procedures. The LES method uses Navier-Stokes equations and subgrid-scale parameterization to resolve large eddies in the atmosphere. This method does not require a predefined turbulence field and can be easily extended to inhomogeneous surface conditions. Although this method has been applied to relatively simple atmospheric flow conditions, it has been used to simulate the flux footprint for convective atmospheric boundary layer conditions (Leclerc et al., 1997). The LES model can also be used to simulate turbulent transport of atmospheric gases and scalar variables. Considerable improvements have been achieved in terms of subgrid-scale parameterization of the LES models and this approach seems to be most realistic of all the different flux footprint estimation techniques. The LES method has already been applied to footprint measurements and Cai and Leclerc (2007) and Cai et al. (2010) have applied a coupled Lagrangian stochastic-LES method to integrated horizontal flux footprint estimation for a convective boundary layer.

The Lagrangian stochastic (LS) model is an atmospheric dispersion model which

can be integrated forward as well as backward in time to simulate paths of individual air particles. Such models are useful tools for flux footprinting and are used for source area estimation. Some applications of this model can be found in Kljun et al. (2003, 2004). An algebraic hybrid version of the LS model has also been proposed by Hsieh et al. (2000). An alternative approach to footprinting is the backward Lagrangian stochastic model (bLs), which can be used to determine the unknown strength of a gas source located upwind. A comprehensive bLs method was developed by Flesch et al. (1995) which can be applied to a small source area of any shape. Software with the trade name *WindTrax* is available for flux footprinting from *www.thunderbeachscientific.com*, which uses the same idea proposed by Flesch et al. (1995). The bLs method has the advantage of simulating the flux footprint in the presence of Gaussian and non-Gaussian turbulence. Examples of application of this model can be found in Laubach and Kelliher (2005) and Laubach (2010), amongst other sources. The important necessary condition for using this model is the requirement of a predefined wind field. The model performance can be enhanced by improved representation of the wind field for specific case studies.

2.3.4 Advantages and disadvantages

Flux measurement using the eddy covariance method is a direct approach, hence there is no need for application of any empirical constants. Although eddy covariance is the simplest method for flux measurement, a considerable amount of post-processing of the dataset is necessary for different chemical species. Some of the post-processing corrections include: density correction or Webb correction[4], coordinate rotation[5], high frequency loss correction for a closed path sensor, energy budget closure and thermal stratification correction (specially for night time fluxes), as shown in Table 2.1.

However, the limiting condition for the EC method is the requirement of homogeneous horizontal conditions and steady state atmospheric conditions. For eddy covariance measurements, we also have to assume that the mean vertical wind velocity is negligible, wind and concentration measurement tools are collocated, and instrument responses are perfect. These conditions are hard to satisfy in a real field condition and corrections often need to be applied (Harvey et al., 2008a). The EC method has to sample the full spectrum of turbulent eddies for the vertical flux, so that a very fast

[4]Appendix A
[5]Appendix B

Table 2.1: Sources of error in eddy covariance measurements and appropriate corrections (adapted from Burba and Anderson (2010))

Errors due to	Affected fluxes	Range	Remedy
Frequency response	all	5 to 30%	Frequency response correction
Time delay	all	5 to 15%	Adjusting for delay
Spikes, noise	all	0 to 15%	Spike removal
Unleveled instrument/flow	all	0 to 25%	Coordinate rotation
Density fluctuation	H_2O, CO_2, CH_4	0 to 50%	Webb correction
Sonic heat error	Sensible heat flux	0 to 10%	Sonic temperature correction
Band broadening	Mostly CO_2, CH_4	0 to 5%	Band-broadening correction
Oxygen in the path	Some H_2O	0 to 10%	Oxygen correction
Missing data filling	all	0 to 20%	Monte-Carlo method etc.

response instrument is required. Some other problems of the EC method for the estimation of N_2O flux include the effect of simultaneous fluxes of heat and vapour which leads to the need for the Webb correction, correct mounting height in relation to gas sensor path length, and correct alignment of the anemometer (Denmead, 2008).

The flux gradient technique is an indirect method and similarity theory assumptions are applied, with horizontal homogeneity and the steady state approximation of the atmosphere being two basic assumptions. One advantage of the FG method is that no fast response measurements are required. In the FG technique, the eddy diffusivity term is parameterized and it is assumed that eddy diffusivity for the gas of interest almost equals the diffusivity of either momentum or heat (Garratt, 1992). The error in the FG technique is mostly associated with the measurement error of momentum or heat flux via temperature or wind speed. Such erroneous estimation of scalar fluxes and variables leads to an erroneous approximation of the eddy diffusivity term (Denmead, 2008).

A bLs model can be used as a footprint model to identify the predominate source area, as well to estimate the source area emission rate of a predefined plot. However, the eddy covariance measurements of atmospheric surface layer flow or the atmospheric profile measurements are necessary for this model simulation. The bLs technique makes the same assumption of homogeneous flow over flat terrain as the vertical-flux techniques. Similarity theory is applied in order to provide consistent relationships between the wind profile shape and turbulent flow parameters (surface roughness, friction velocity and stability). It is therefore applied with similar restrictions to the FG technique. In principle, it would be possible to apply the bLs technique with different flow models that can account for obstacles, roughness changes, or strongly convective conditions. However, combinations of the bLs method with such

Figure 2.2: The 10 m instrumented tower of 2011 campaign.

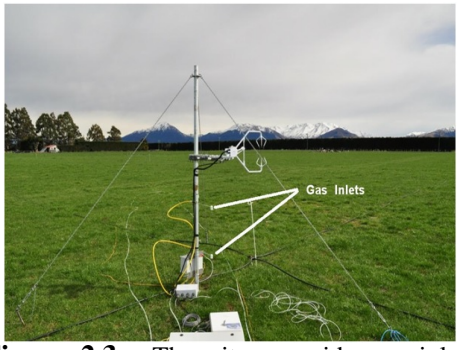

Figure 2.3: The nitrous oxide gas inlets (shown by white lines) are fitted with the CSAT3 and LiCor 7500 of 2010 campaign.

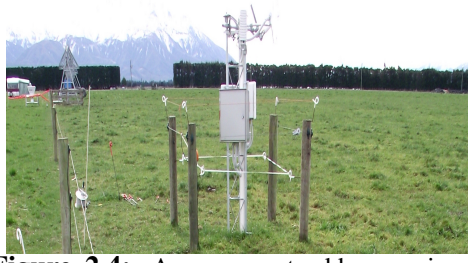

Figure 2.4: A permanent eddy covariance tower at the paddock setup by NIWA in 2011 in the same field.

models are not readily available to date. An advantage of the bLs technique over the flux-gradient technique is that it is less sensitive to precision of the concentration measurement. Table 2.2 shows a comparison of the different techniques described above.

2.4 Overview of climatology of the experimental site

A brief description of the field site climatology is provided in this section. Detailed field alignment and instrumentations are discussed in the next chapter. The experimental site for this study is located near Methven (43.67°S and 171.58°E) in the South Island of the New Zealand and has an elevation of 305 m. A National Institute of Water and Atmospheric Research (NIWA) climate station is permanently located at this site, although long term climate data are only available from the NIWA Cliflo database (http://cliflo.niwa.co.nz/) from 2010. Two field experiments, which are discussed in these thesis, were carried out in 2010 (autumn and spring) and a single field experiment was carried out in 2011 in the same paddock. The field surroundings and some of the instrumentations are shown in Figures 2.2-2.4 and details are provided in Chapter 3.

Table 2.2: Advantages and disadvantages of techniques of flux estimation, modified from Harvey et al. (2008a).

Factors	**Techniques**		
	Chambers	bLs models	Micrometeorological
Temporal variability	Limited, < 24 measurements/day	High	High
Spatial scale	m^2	$10-10000\ m^2$	tens of thousand m^2
Suitability	Yes, repeated measurements possible	Yes, through averaging	Yes, through averaging
Complexity	Low	High	Very high
Cost	Low[a]	High	High
Portability	High[b]	Low	Low
Relative sensitivity	High	High	Variable (gas sensitive)
Inhibition effect	Yes	None	None
Pressure sensitivity	Yes	None	None
Leakage sensitivity	Yes	None	None
Solar heating effect	Yes[c]	None	None
Atmospheric turbulence effect	No[d]	Yes	Yes
Rainfall effect	Yes	Yes	Yes

[a] Low cost compare to other methods, but may vary depending on the labour cost - require less than about 4 measurements/day.
[b] Provided bases are established before the measurement period.
[c] Regarded as a limitation - resulting in perturbation of emitting environment, probably increasing flux.
[d] Regarded as a limitation - closed chambers reduce the effect of ambient wind and minimize one of the principle factors of mass transfer.

To summarise the atmospheric temperature (°C), rainfall (mm) and net radiation (MJm^{-2}) at the station for the months of May-June and September-November, daily averages of these variables were estimated using data for the two years (2010 and 2011), as shown in Figure 2.5. The May-June and September-November periods were analyzed to corroborate with the time periods of field experiments of 2010 and 2011. The averages of 2 m air temperature and rainfall for the months of May and June and September to November over the experimental location were found to be 7.5 °C and 10.5 °C, and 3.48 mm and 2.67 mm respectively. A clear increasing trend in the temperature and net radiation values were observed for the spring experiment whereas the daily rainfall had a decreasing trend. These results corroborate well with the drier boreal summer time conditions of the eastern South Island.

2.5 Comments

Some of the available approaches and techniques for biogenic flux estimation have been discussed in this chapter, and it has been shown that none of the above mentioned techniques is perfect, although for nitrous oxide flux measurement, chambers have been used traditionally, and the combined FG-EC method, which is a relatively newer method than chambers from New Zealand's perspective, has a future prospect of application. This research is, therefore, focused on the verification of such a combined FG-EC micrometeorological system of N_2O measurements for agro-meteorological conditions of New Zealand. Hence, efficacy of a FG-EC micrometeorological setup is tested over a commercial paddock in New Zealand in terms of measurement accuracy, uncertainty in the flux values, identification of source areas and the effect of atmospheric surface layer turbulent properties.

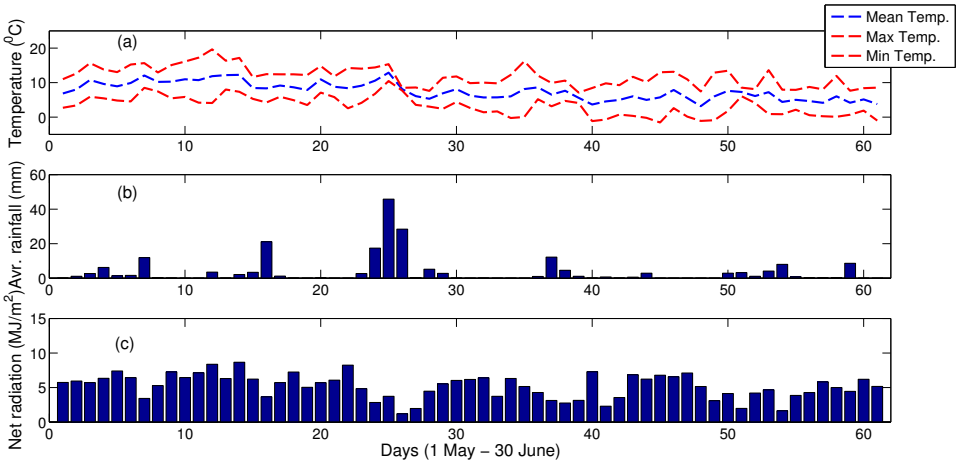

(a) Autumn

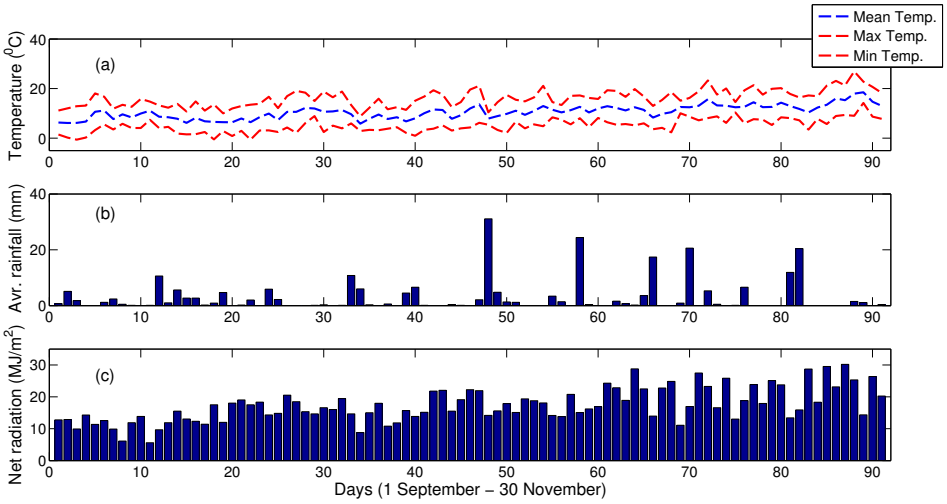

(b) Spring

Figure 2.5: Two-year averages of (a) air temperature (°C), (b) average rainfall (mm), and (c) net radiation (MJm^{-2}) for the month of (Autumn) May and June and (Spring) September to November observed at the experimental site.

Chapter 3

Measurement of nitrous oxide flux and assessment of error propagation

3.1 Introduction

N_2O has been identified as the third largest contributor to New Zealand's total greenhouse gas emissions after CO_2 and CH_4, and a substantial increase in the emission of N_2O has been estimated during 1990-2009 (Sweeney et al., 2011). The principal source of N_2O in New Zealand is the green pasture where livestock are produced (Petrie et al., 2006; Sweeney et al., 2011). Agricultural emissions of CH_4 and N_2O account for 54.8% of the total greenhouse gases emitted by New Zealand on a CO_2 equivalent basis (Saggar et al., 2008), while agricultural N_2O itself accounts for 17.2% of New Zealand's total greenhouse gas emissions (Petrie et al., 2006; Sweeney et al., 2011). Therefore, N_2O from the green pastures is one of the primary concerns for mitigation. However, the challenging nature of measurement of N_2O flux, because of its high spatio-temporal variability, leads to large uncertainty in measured concentrations. Hence, it becomes difficult to ascertain the actual effect of mitigation on the N_2O emission rate.

Traditionally, N_2O flux from the soil surface has been measured using chambers (Saggar et al., 2005; Luo et al., 2008a,b; Saggar et al., 2008), and very few micrometeorological experiments have been carried out over New Zealand to measure the emission rate of N_2O from pastures (Kelliher et al., 2002; Harvey et al., 2008b; Saggar et al., 2010). The top-down micrometeorological approach of N_2O flux estimation based on a tunable diode laser was verified by Harvey et al. (2008b) for New Zealand, and in this study, the effectiveness of a similar micrometeorological set up has been

evaluated over a commercial paddock in Canterbury, New Zealand, so that this method can be standardized and used extensively. Therefore, N_2O flux has been estimated using a coupled Eddy covariance (EC) - flux gradient (FG) micrometeorological set up where the flux values depend on eddy diffusivity, and the eddy diffusivities are estimated based on surface meteorological variables.

Since the application of a coupled FG-EC system of flux measurement is comparatively new in New Zealand, the first objective of this study is to estimate N_2O flux from an agricultural paddock for two different seasons and compare these with the previously reported values. This would verify the measurement method. Furthermore, since the eddy diffusivity of a FG-EC system can be estimated from both a parameterization and a thermodynamic approach, an inter-comparison of fluxes will also be made.

A second objective of this study would be to estimate degrees of uncertainty or error in the measured flux values. Such an uncertainty estimate of N_2O flux is necessary not only because of the high spatio-temporal variability of N_2O source area emission, but the FG-EC measurement system itself has an intrinsic error propagation mechanism. Therefore, an error sensitivity analysis of the FG-EC method of flux estimation will be performed based on some derived mathematical relationships. Instead of finding the sources of error in the transfer coefficient, some of which have already been reported by Mammarella et al. (2010) and Kroon et al. (2010), this study will investigate the total error/uncertainty variance in terms of the cumulative effect of uncertainties in their constitutional variables. A Monte-Carlo approach would be followed to estimate the probability distribution of errors. Finally, total error estimates will be provided for the measured flux values with respect to atmospheric surface layer stability. As mentioned in Chapter 1, the error analysis method described here is generic and can be applied to some other measured entity if a similar micrometeorological approach is followed. Again, systematic error and error from footprint heterogeneity will not be considered in this chapter.

Section 3.2 of this chapter describes the theory of the FG micrometeorological technique. In Sections 3.3 and 3.4, field locations and instrumentation are described. Results are described in Section 3.5. The derivation of relative random errors is provided in Section 3.5.6 and estimates are provided in Section 3.5.7. A summary has been provided in Section 3.6.

3.2 Theory: flux gradient relationships

In the FG relationship, the vertical transport of a gas (g) in the homogeneous surface boundary layer is described by the equation (Garratt, 1992):

$$F_g = -k_g(\partial c_g/\partial z) \tag{3.1}$$

Where c_g for our case is the N_2O gas concentration (ppb or nmol mol^{-1}_{air}) and z is height (m). F_g is the flux density of N_2O. The concentration difference of the gas (ΔC_{N_2O}) is obtained by measuring concentrations at two different heights. k_g is the eddy or turbulent diffusivity of the gas of interest, and is determined using a local or first order closure model analogous to the molecular diffusion approach. For stable and unstable conditions, non-dimensional universal functions for momentum, heat and gas, (ϕ_m, ϕ_h, ϕ_g), are used to estimate the eddy diffusivity. The ϕ_m, ϕ_h and ϕ_g are functions of a characteristic length scale, (ζ = z/L), where, L is Obukhov length which can be derived from eddy covariance (EC) measurements (Monin and Obukhov, 1954).

Measurement of surface flux (F_g) using the FG relationship of Equation 3.1 requires a valid estimation of k_g, which again requires estimation of ϕ_g. We assume that $\phi_g = \phi_h$ for all stability classes with a homogeneous distribution of surface sources (Dyer and Bradley, 1982). Accordingly, a valid estimation of k_h will be analogous to k_g and can be used in Equation 3.1 for estimation of N_2O flux or any other entity.

Thermodynamic, parameterization, and aerodynamic methods are available for the estimation of F_g. The terms thermodynamic and parameterization are used to differentiate the approach taken to flux estimation. In a broader sense, parametric forms of equations are used in both cases. In a simple thermodynamic method, thermocouples are used at different heights for temperature difference measurement, and heat flux obtained from a sonic anemometer is used to estimate the thermal eddy diffusivity, k^t_h ($m^2\ s^{-1}$) following Garratt (1992).

$$\overline{w'T'} = -k^t_h(\partial T/\partial z) \tag{3.2}$$

Since, the measured temperature by a sonic anemometer is approximately equal to virtual temperature, sonic temperatures were corrected for the air temperature. Again a moisture-density correction is necessary to obtain a correct sensible heat flux and details of these corrections are described in Section 3.2. Finite differences of temperature and height are used in the above equation to estimate k^t_h and together with the molar concentration of air, flux values can be obtained using Equation 3.1.

In a simple parameterization scheme, the eddy diffusivity, k_h^p ($m^2\ s^{-1}$), is calculated following the relationship:

$$k_h^p = \kappa u_\star z \phi_h^{-1} \tag{3.3}$$

where, κ which is von Karman's constant = 0.40 after Yaglom (1977) and $u_\star$ is the friction velocity and defined as $u_\star = [(\overline{u'w'})^2 + (\overline{v'w'})^2]^{1/4}$. The u, v, and w are the downwind, crosswind and vertical wind components.

A similar relationship also holds for k_m, ($k_m = \kappa u_\star z \phi_m^{-1}$), where k_m is the turbulent diffusivity for momentum. The non-dimensional thermal stratification and wind shear functions, (ϕ_h, ϕ_m), have been represented using different formulae by various authors and a detail description can be found in Garratt (1992) and Arya (2001). For a vertical wind profile, the integrated forms of ϕ_h and ϕ_m are represented by ψ_h and ψ_m, which have different analytical solutions for different atmospheric stratifications. Therefore, a diffusion velocity parameter (d_h^p) (m s^{-1}) can be defined similar to Phillips et al. (2007) as:

$$\left.\begin{aligned} d_h^p &= \kappa u_\star / J \\ J &= [ln(z_2 - d) - \psi_h(\frac{z_2 - d}{L})] - [ln(z_1 - d) - \psi_h(\frac{z_1 - d}{L})] \end{aligned}\right\} \tag{3.4}$$

where $\psi(\frac{z-d}{L})$ is represented following Paulson (1970), Businger et al. (1971) and Hogstrom (1988):

$$\begin{aligned} \psi_h(\frac{z-d}{L}) &= 2ln(\frac{1+y}{2}) \quad for\left[\frac{z-d}{L} < 0\right] \\ \psi_h(\frac{z-d}{L}) &= -7.8(\frac{z-d}{L}) \quad for\left[\frac{z-d}{L} \geq 0\right] \end{aligned} \tag{3.5}$$

where y = 0.95(1 - 11.6$\frac{z-d}{L}$)$^{1/2}$ after Hogstrom (1988). The term d represents displacement height. A similar relationship exists for the eddy diffusivity k_m and stability function ψ_m, which can be represented as follows (Paulson, 1970):

$$\begin{aligned} \psi_m(\frac{z-d}{L}) = ln[(\frac{1+x^2}{2})(\frac{1+x}{2})^2] - 2tan^{-1}x + \frac{\pi}{2} \quad for[\frac{z-d}{L}] < 0 \\ \psi_m(\frac{z-d}{L}) = -6.0(\frac{z-d}{L}) \quad for[\frac{z-d}{L}] \geq 0 \end{aligned} \tag{3.6}$$

where $x = (1 - 19.3\frac{z-d}{L})^{1/4}$ after Hogstrom (1988). Finally, flux values of any entity, or N_2O in our case, can be estimated by using the d_h^p values and the finite difference of Equation 3.1. In the following sections of this study, the term 'transfer coefficient' has been used to represent both k_h^t and d_h^p. However, it has to be considered that units of k_h^t and d_h^p are different and necessary adjustment should be made during the final flux estimation (see Appendix D).

3.3 Description of experimental site

The experimental site chosen for the field trial is a commercial dairy farm, located south-west of Christchurch, near Methven, Canterbury, New Zealand (Figure 3.1). The approximate location of the field is 43.67°S and 171.58°E, which is also the site of a separate National Institute of Water and Atmospheric Research (NIWA)/Environment Canterbury (ECAN) water management project. The elevation of the experimental plot above mean sea level is 305 m. This agricultural paddock is located close to the mountain range of the Southern Alps.

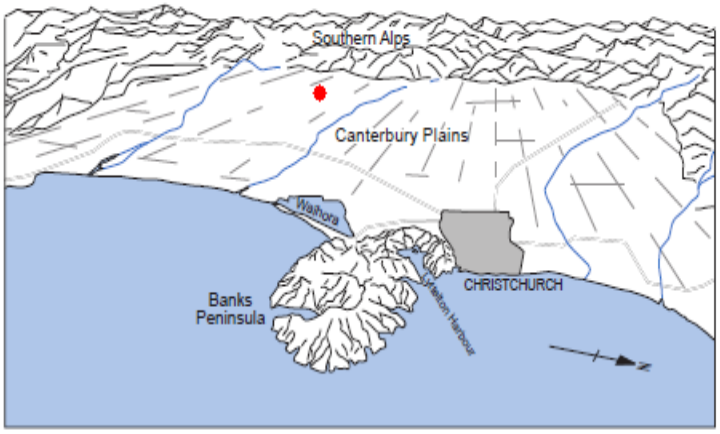

Figure 3.1: Topography of the area is shown with an approximate location of the field, marked with a red dot. This figure is modified from Sturman and Spronken-Smith (2001).

The paddock is divided mainly into two different areas: subplots for micrometeorological observations (subplots A-E) and chamber measurements (subplot below E) in Figure 3.2. The micro-meteorological plot is further subdivided into control (A, C and E) and experimental subplots (B and D). Each subplot is approximately 100 × 140 m in area. The big red square box is the external boundary of the farm and blue circles are irrigator pathways. Blue dots between the boxes are the locations of micrometeorological and flux measurement stacks with gas inlets for continuous measure-

ment of atmospheric variables. The blue square box in subplot C is the approximate location of the caravan where the tunable diode laser (TDL) was located. Green lines are the FG pipes from the gas inlets and the red line is a 240 V A.C. cable for running the TDL. The chamber measurements were not continuous, although chamber samples were collected at regular intervals from the blue rectangular box area of the chamber plot below subplot E in autumn.

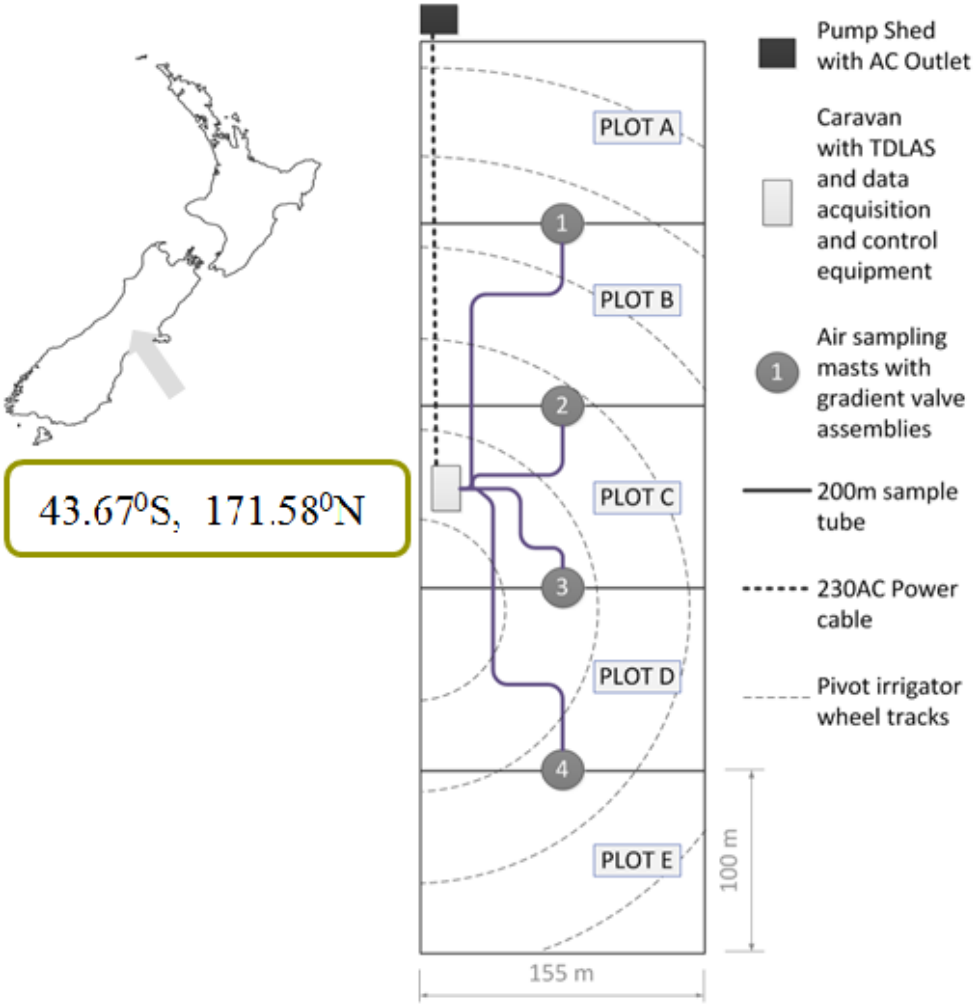

Figure 3.2: Field layout showing individual subplots (marked as A - E) and measurement stacks marked as 1-4. The blue half-circles are irrigator pathways. The location of the site (43.67°S, 171.58°N) is shown by a green box.

3.4 Instrumentation and measurement details

The Atmospheric Emissions group of NIWA has developed a micrometeorological system based on the flux gradient and eddy covariance approaches where the nitrous oxide

gas concentration is measured at two different heights (0.5 m and 1 m) with a tunable diode laser (TGA-100, Campbell Scientific Inc.). A fast response and sensitive TDL works on the principles of absorption spectroscopy and is able to detect episodic nitrous oxide emissions from fields. A comprehensive review of micrometeorological applications of TDL on paddock scale measurements can be found in Pattey et al. (2006a). Two gas inlets were fitted on each measurement mast at 0.5 m and 1.0 m height, shown by blue dots in Figure 3.2. Wind sensors were placed in three subplots. Along with the conventional cup anemometers, a 3-dimensional sonic anemometer, Campbell Scientific Inc. CSAT3, Logan , UT, (d_{sl} = 10 cm in vertical, 5.8 cm horizontal), and a Gill triaxial ultrasonic anemometer, Wind master Pro, Lymington, UK, were used on three different masts. A CO_2/H_2O open path gas analyzer, Li-Cor-7500 (path length = 12.5 cm), was used for CO_2 and H_2O flux measurements. The gas analyzer, Li-Cor-7500, and the sonic anemometer, CSAT3, were mounted on a single mast at a height of 2 m with a separation distance of 10 cm. This measurement mast was placed between subplots B and C. The Gill anemometer was placed between subplots C and D. Thermocouples and cup anemometers were mounted on a meteorological tower between subplots A and B for profile measurements on the most northward mast. Temperature sensors or free spanned resistance wires (diameter $< 20\ \mu m$) were fitted at 2.49 m, 1.302 m and 0.55 m, and cup anemometers were fitted at 2.72 m, 1.52 m, 0.72 m, and 0.406 m. This experimental set up was maintained in both campaigns except for a change in the location of the chamber measurement subplot in spring. The measurement campaign in autumn was carried out from 9 May 2010 to 21 June 2010 and in spring from 24 Sept. 2010 to 22 Nov. 2010.

3.4.1 Data description and processing

The sonic anemometers, CSAT3 and Gill, sampled data at 10 Hz. The CO_2/H_2O gas analyser, Li-Cor 7500, was mounted on the same mast as the CSAT3 and also sampled at 10 Hz. The initial data quality assessment of spike removal, similar to Vickers and Mahrt (1997), was performed by removing any data $> 3.5\sigma_{var}$ of the standard deviation value (σ) of an individual variable (var). Then, two important procedures were followed, the sonic rotation for covariance estimation and the density correction. The three dimensional wind field was trigonometrically rotated to force $\overline{w}$ = 0 and $\overline{v}$ = 0 (McMillen, 1988), and Webb correction was applied to concentration measurements of CO_2 and H_2O (Webb et al., 1980). The Webb correction for the H_2O concentration

was found to be small for both sensors and seasons and found to vary between 0.0001 - 0.005 umol m^{-2} s^{-1}. Finally, 30 and 20 min averaged runs were generated for autumn and spring, respectively. The 30 min integrating time in autumn was used to comply with the 9 sec FG sampling of the N_2O flux, whereas, during the spring experiment 6 sec FG sampling of the N_2O flux was made to include more nitrous oxide flux samples. Therefore, the integrating period was reduced to 20 min, although, both 30 and 20 min integrating periods were found to capture the entire cospectra of wind component w and temperature T. Additional corrections for data quality improvement were also carried out and described in the following sections.

Calibration of EC and FG instruments, including the sonic anemometers and the TDL, were done at the NIWA Gas-Laboratory, Wellington, New Zealand. Since the physical locations of the sonic anemometers were separated by a distance of 100 m, some differences in the measurements of these two instruments were expected. Therefore, characteristics of these sonic measurements were compared for individual seasons. A similar verification of surface layer turbulence properties were also investigated by Laubach and McNaughton (2009). Variables used for comparison are friction velocity ($u_\star$), temperature flux ($\overline{w'T'}$) and temperature (T). Continuous measurements during 15 June 2010 00:15 NZST to 21 June 2010 00:15 NZST of the autumn campaign are used to test the similarities in observations. The data period was chosen in a way that no brief interruption and no missing data occurred during the period of comparison. 30 and 20 min averaged runs from the sonic anemometers were used for this purpose. Differences in the standard deviation of $u_\star$ values for this period were found to be 0.7%, while vertical temperature flux values ($\overline{w'T'}$) differed by 0.8%. The mean difference in the standard deviation values of temperature was found to be 0.6^0C between the CSAT3 and Gill observations. The comparison data includes both day and night time atmospheric conditions, including highly stable/unstable cases. Similarly, continuous measurements from 14 Nov. 2010 18:10 NZST to 17 Nov. 2010 12:10 NZST of spring have been compared. Differences in the standard deviation values of $u_\star$ and $\overline{w'T'}$ were found to be 1% and 0.5%, where the absolute difference in the standard deviation values of temperature between the CSAT3 and Gill anemometer was found to be 0.13^0C. Although dissimilarities in these measurements were small enough and measurements of CSAT3 and Gill anemometers were consistent, corrections are made in the following section to remove observations that are not conducive for flux estimation.

3.4.2 Measurement heights

The FG technique uses gas inlets at different heights and exact representation of measuring height is always debatable. We have followed the formulations by Laubach and Kelliher (2004) for a logarithmic wind profile and intermediate height, z_m, where $z_m = \Delta z_{21}/\ln(z_2/z_1)$, and z_1 and z_2 are the two measuring heights. This measurement height approximation has been used for both seasons. Since the flux gradient inlets were located at a height of 0.5 m and 1.0 m, wind and temperature observations approximately at the same heights were used. For the wind gradient, measurements at 0.406 m and 1.52 m, and for the temperature gradient, measurements at 0.55 m and 1.30 m were used. Ideally, meteorological instruments should be located exactly at the same height as the flux gradient inlets, but because of the non-collocation of these instruments, those observations that were nearest to gas inlet measuring heights were used. Next, the mean measurement height (z_m) was computed following Laubach and Kelliher (2004), where z_1 was the average height of the bottom wind and temperature sensors (0.406 and 0.55 m) and equal to 0.478 m, and z_2 was the average height of the top wind and temperature sensors (1.52 and 1.30 m) and equal to 1.41 m.

3.5 Results

3.5.1 Turbulence statistics

Since d_h^p is dependent on the friction velocity, $u_\star$ (Equation 3.4), a proper estimation of $u_\star$ is necessary. Therefore, to filter out outliers in $u_\star$ values, measurements were discarded when the friction velocities were too low, $u_\star < 0.075$ m s^{-1}, and where $u_\star/U_{mean} > 0.2$. A similar filtering technique has been reported by Laubach (2010) where those runs with $u_\star < 0.12$ m s^{-1} and $u_\star/U_{mean} > 0.2$ were rejected. A marginally lower bound of $u_\star$ has been used in this study to accommodate more data with relevant information. Furthermore, this filtering criteria is also found to be similar to one described by Phillips et al. (2007). Filtering of the $u_\star$ values using these criteria removes periods when surface layer conditions were very stable, reducing the turbulent eddy transport, and when highly unstable surface layer stratification increases the $u_\star$ values. Figure 3.3 shows the relationship between u(z) and $u_\star$ before and after filtration for autumn and spring data, and for the CSAT3 and Gill anemometer, respectively. After the filtration, a total of 965 and 2068 samples from CSAT3, and 1346 and 2664 samples from Gill were considered for autumn and spring for further analysis. The difference

in the rejection rate between two anemometers can be attributed to the fact that the total observed data for the CSAT3 was smaller than Gill to begin with, because more data points were rejected from the CSAT3 during spike removal.

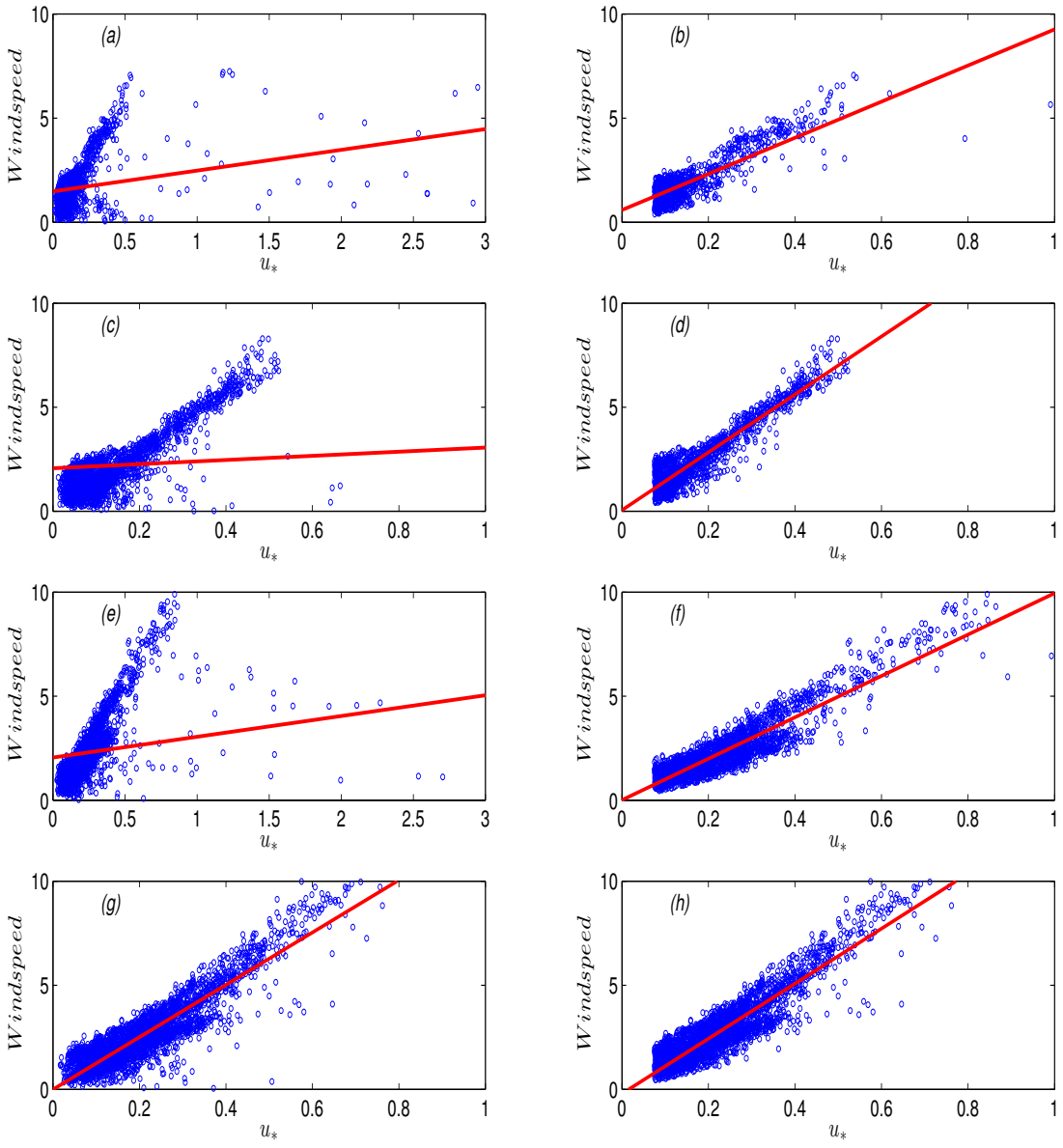

Figure 3.3: Wind speed (ms^{-1}) represented as a function of $u_\star$ (ms^{-1}) before and after filtration for autumn (a, c, e, g) and spring (b, d, f, h). Plots a - d are for the CSAT3 data, and plots e - h are for the Gill anemometer data. Red lines are the best fit linear regression lines.

Along with the eddy covariance measurements, friction velocities were also estimated based on wind profile data following the relationship (Kaimal and Finnigan, 1994):

$$u_\star = \kappa \frac{u(z_2) - u(z_1)}{ln(z_2 - d) - ln(z_1 - d)} \tag{3.7}$$

Here, z_1 and z_2 represent the height of the bottom (0.406 m) and top (2.72 m) cup anemometers. This wind profile relationship is strictly valid for a neutral atmosphere. $u_\star$ values estimated from the wind profile measurements for neutral cases ($|1/L| \leq 0.04$) were compared with the CSAT3 measurements. Figure 3.4 shows the comparison of friction velocities estimated from CSAT3 and wind profile measurements for the autumn and spring periods only for neutral cases. A better similarity in the spring campaign was due to re-calibration of the cup anemometers. Except for some higher friction velocity values in the sonic measurements, estimations of $u_\star$ by the two different methods are comparable for both seasons and no major differences were observed.

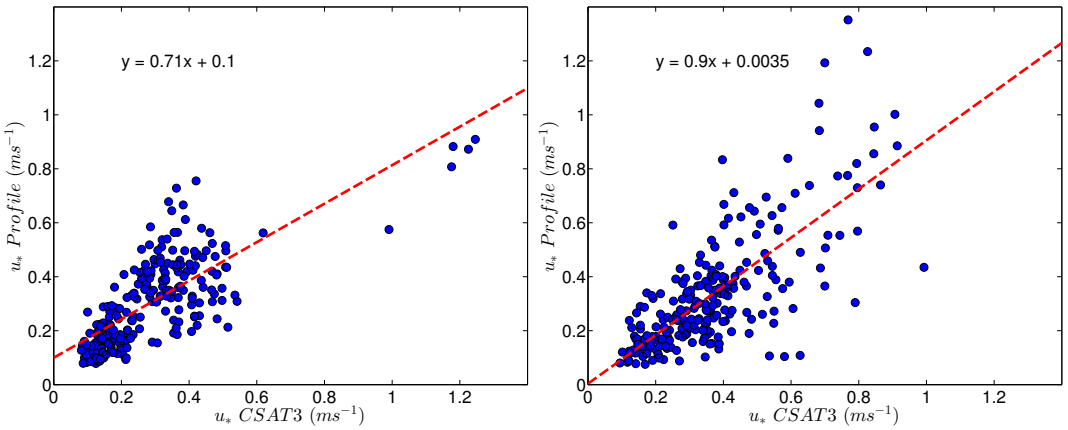

(a) (b)

Figure 3.4: Comparison of friction velocities from wind profile (cup anemometers) and sonic anemometer measurements for neutral cases ($|1/L| \leq 0.04$) of (a) autumn and (b) spring experiments. Red lines represent the linear fit between $u_\star$ from the CSAT3 and cup anemometer measurements.

3.5.2 Stability parameter (1/L) - inverse Obukhov length

In the previous section, filtered sonic measurements were compared with the profile measurements for neutral/near-neutral cases. The objective of that filtration was to remove extreme stability situations. To make sure that the data quality was good enough for more analysis, the filtered runs were further classified in terms of a stability parameter ($1/L$, m^{-1}). According to the scale analysis of Monin-Obukhov similarity theory the appropriate stability parameter is *z/L*. However, the inverse Obukhov length is also accepted as an indicator of atmospheric surface layer stability (Laubach, 2010) as $|L|$

signifies the transition from a shear driven flow in the surface layer to the buoyancy driven flow in the outer layer above the surface layer and z is used to scale the height. Most of the highly stable and unstable cases were found to be removed by the filtration and only 8 and 13 samples from CSAT3 and 6 and 21 samples from Gill, for autumn and spring, were found where $|1/L| > 0.5$. Consequently, these samples were also removed from the final data. Thus, a total of 957 and 2055 samples from the CSAT3 and, 1340 and 2643 from the Gill were used in the next section, respectively for autumn and spring. Figure 3.5 shows the histogram of $1/L$ for the autumn (subplot a) and spring (subplot b) campaigns from the CSAT3 observations. A similar distribution is also observed for the Gill data. It is evident from Figure 3.5 that for both autumn and spring, atmospheric conditions were predominantly neutral or near neutral, with only very few cases that were extremely stable or unstable. Based on the values of $1/L$, surface layer stratification was divided into 'stable', when $(1/L) > 0.1$, 'unstable', when $(1/L) < -0.1$, 'neutral', when $|1/L| < 0.04$, and 'stable-near-neutral', when $0.04 < 1/L < 0.1$ and 'unstable-near-neutral '$-0.04 > 1/L > -0.1$. This stability classification is somewhat close to the one provided by Laubach (2010).

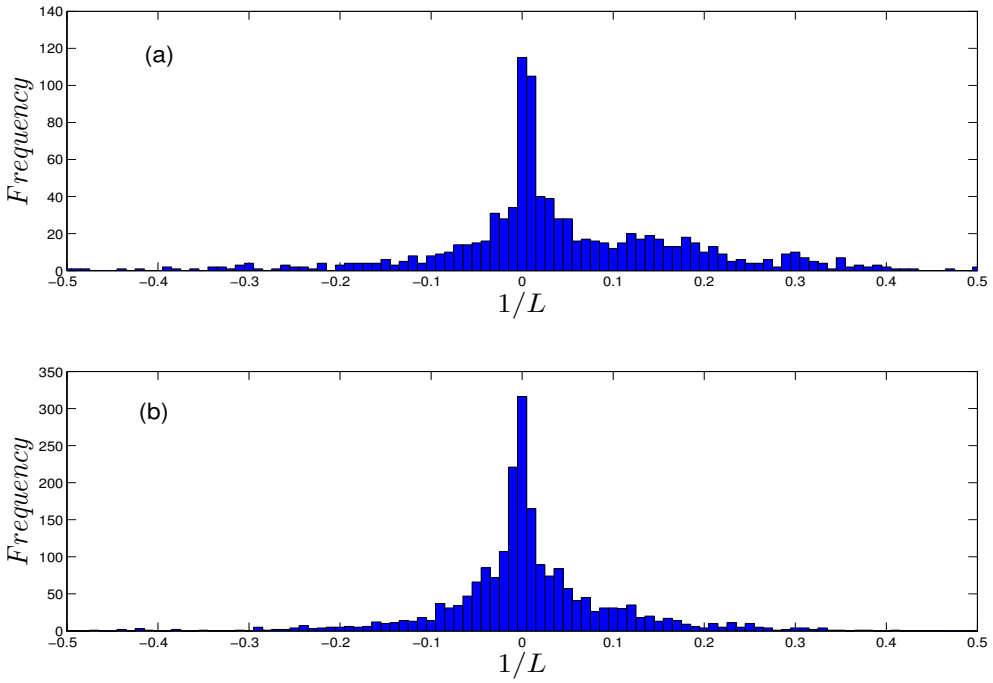

Figure 3.5: Histogram of inverse Obukhov length ($1/L$) for (a) autumn and (b) spring . The bin sizes are 0.01 m^{-1}.

3.5.3 Wind distribution and roughness length

The wind pattern during 9 May 2010 to 21 June 2010 period of the autumn campaign is shown in Figure 3.6a. A total of 957 filtered CSAT3 measurements were used for the wind-rose diagram. The wind directions shown in Figure 3.6 were relative to the orientation of the measurement plot and three predominant wind regimes were found, 0-50^0 (north-north-east) 18.1% of the total data with average wind speed 2.60 ms^{-1}, 300-360^0 (north-north-west) 33.9% of the total data with average wind of 1.94 m s^{-1}, and 200-260^0 (south-west) 22.0% of the total data with mean wind speed 2.63 m s^{-1}. Four consecutive cases of high wind, wind speed $>$ 7.0 m s^{-1}, from the south-west were also observed in this period. These were found to be associated with a frontal system moving from south to north across the South Island.

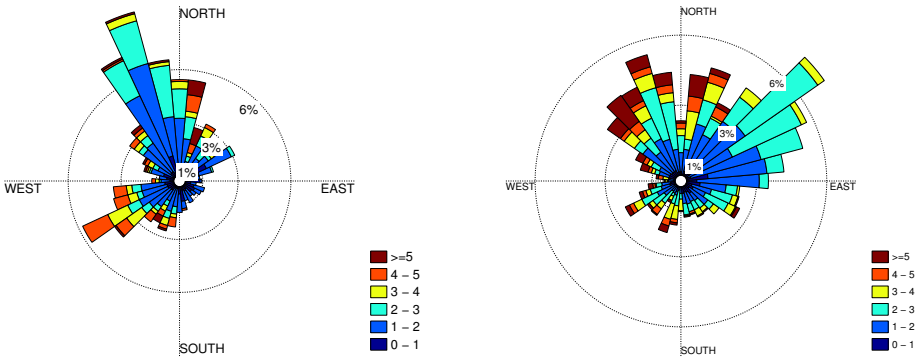

(a) Autumn (b) Spring

Figure 3.6: Wind distributions for (a) the autumn and (b) the spring campaigns. Wind sectors are sub-divided based on wind speed (m s^{-1}).

Wind patterns between 24 September 2010 and 22 November 2010 of the spring campaign are shown in Figure 3.6b. A total of 2055 samples of 20 min averaged runs from the CSAT3 were used for this purpose. Wind regimes for this period were found to be approximately the same as for autumn, except for an increase in northeasterlies. The dominant wind direction for this period was beween northerly and easterly abbreviated as north-northeasterly (0-100^0), 45.3% of the total observation with an average wind speed of 2.11 m s^{-1}. Similarly, North-northwesterlies (300-360^0) constituted 24.1% of the total observations with an average wind speed of 3.12 m s^{-1}, and south-westerlies (200-260^0) only 9.3% of the total with an average wind speed of 2.69 m s^{-1}. A few cases were also observed when strong winds, wind speed $>$ 7.0 m s^{-1}, were found to blow from northwest of the site, presumably coming from the moun-

tains. The surface wind speed and direction measurements were not affected by the presence of cattle as observations were carried out in between fertilizer applications and grazing. Changes in roughness length values with wind direction and stability were also explored for assessment of homogeneity.

Roughness length, z_0, can be estimated from the profile measurements as well as from the numerical relationship, $u(z) = (u_\star/\kappa)[\ln(z/z_0) - \psi_m(z/L)]$, where ψ_m is the stability dependent integral profile similarity function for momentum (Neftel et al., 2008) (Equation 3.6). The sonic anemometer measurements for 'neutral' conditions, $-0.04 \leq 1/L \leq 0.04$, were used for this purpose. Roughness length values were found to be comparable for both campaigns. Minor differences were observed for three predominant wind regimes because of the locations and heights of the surface roughness elements. A consistent roughness length of 0.03 m was observed for northwesterly and southwesterly wind regimes for both the campaigns, whereas a higher z_0 value was observed for the northeasterly wind. A tall shelter belt, approximately 300 m northeast of the site, is a probable reason for such variation. As a result of the analysis, $z_0 = 0.03$ m and displacement height $d = 0.066$ m, are used for both the campaigns.

3.5.4 Transfer coefficients

The transfer coefficients (k_h^t and d_h^p) were estimated using Equations 3.2 and 3.4. Filtered time averaged runs from the sonic anemometers and profile measurements were used to produce k_h^t and d_h^p values for autumn and spring. $\psi_h(\frac{z_1-d}{L})$ and $\psi_h(\frac{z_2-d}{L})$ were estimated for the mean heights mentioned previously. k_h^t values were estimated from temperature differences and covariance data from the sonic anemometers. Some outliers in the k_h^t values were observed where either the covariance term was too high or the temperature difference was too low, and such values were also neglected. Only those values of k_h^t were accepted where they range between $0 \leq k_h^t \leq 0.5$. This k_h^t range was accepted by considering 80% of the k_h^t values from the histogram. A total of 325 and 518 such k_h^t values were obtained for autumn from the CSAT3 and Gill observations. Similarly, 946 and 1186 values of k_h^t were obtained for spring.

Figure 3.7a shows the range of d_h^p values for both sensors and seasons. The median values of d_h^p were found to vary between 0.043-0.082 m s^{-1} irrespective of season and sensor. The maximum outlier value was found to be 0.417 m s^{-1} from CSAT3 measurements of the autumn experiment. The d_h^p values from the CSAT3 and Gill for autumn and spring were found to be highly comparable as high R^2 values were ob-

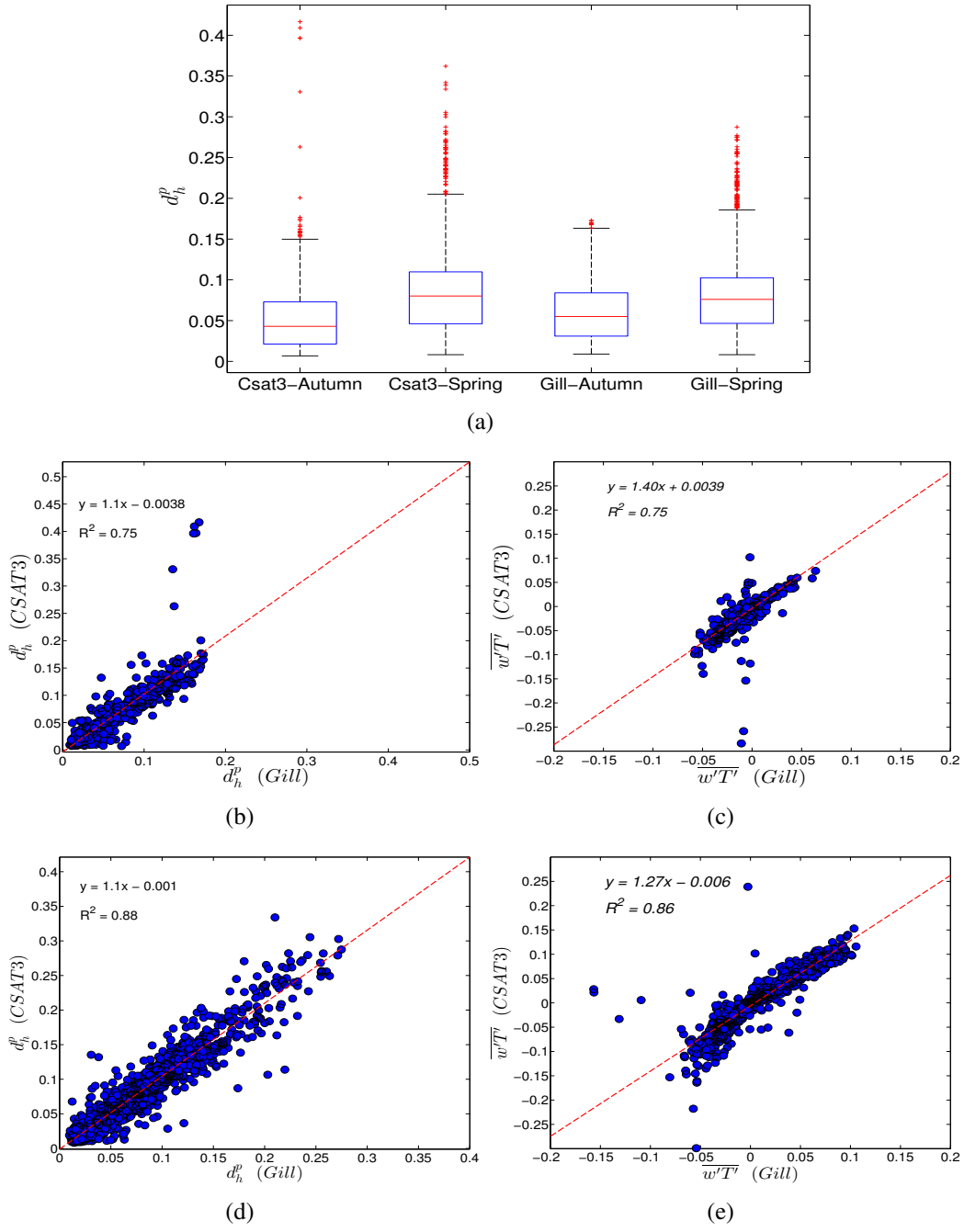

Figure 3.7: Box-plot (a) showing variations in mean and standard deviation values of d_h^p in spring and autumn; the linear fit between the filtered d_h^p from CSAT3 and Gill for (b) autumn and (d) for spring; and the linear fit between the filtered $\overline{w'T'}$ from the CSAT3 and the Gill for (c) autumn and (e) spring.

served (Figures 3.7b and 3.7d). Few d_h^p values associated with high wind speed periods were also observed in spring when the wind direction was found to be predominantly northwesterly, from over the mountains. These values were not ignored according to our filtering criteria. '*y*' and '*x*' in the linear fit equations are shown in the figures as y and x-axis variables of the corresponding diagrams.

Atmospheric surface layer stability has already been classified in Section 3.5.2 as the '*Inverse Obukhov length*'. Here, the diffusivity/diffusion parameters are further explored based on that classification[1]. Table 3.1 shows the total number of observations available for d_h^p and k_h^t for individual stability class. The stability classifications are based on 1/*L* values, where *L* is computed individually for the CSAT3 and Gill. The *L* values from two different instruments were comparable and no major differences were found. It is evident from Table 3.1 that predominant atmospheric condition was neutral for both seasons, 43.05% and 60.6% of the total observations from the CSAT3 and Gill were neutral in autumn. Similarly, 55.4% and 61.4% of the total observations in spring were neutral.

Table 3.1: Number of observations available for diffusion/diffusivity parameters (d_h^p, k_h^t) in different stability classes based on 1/*L*.

Seasons	**Stability classes**	d_h^p**-CSAT3**	d_h^p**-Gill**	k_h^t**-CSAT3**	k_h^t**-Gill**
Autumn	Neutral	412	812	194	372
	Stable	274	154	34	28
	Unstable	84	92	41	39
	Stable-near-neutral	111	176	22	31
	Unstable-near-neutral	76	106	34	46
Spring	Neutral	1140	1625	576	788
	Stable	253	157	64	44
	Unstable	150	215	62	92
	Stable-near-neutral	250	344	54	96
	Unstable-near-neutral	262	302	139	132

3.5.5 Nitrous oxide flux

Air samples were collected using two gas inlets alternatively turned on and off every 9 and 6 seconds for autumn and spring, respectively, and concentration differences were computed by subtracting the measured 1 m gas inlet concentration from the measured 0.5 m concentration of each mast. Then, the 30 and 20 min time averaged concentration

[1] $|1/L| < 0.04$ = neutral; (1/*L*) > 0.1 = stable; (1/*L*) < -0.1 = unstable; $0.04 \leq 1/L \leq 0.1$ = stable-near-neutral; $-0.04 \geq 1/L \geq -0.1$ = unstable-near-neutral.

difference (ΔC_{N_2O}) values were produced at each mast, respectively for autumn and spring. A more technical description of the ΔC_{N_2O} measurement technique can be found in McMillan et al. (2012) and in Section 3.5.9 [2].

Now, the eddy diffusivities were also computed from the CSAT3 and Gill measurements at mast 2 and 3. Assuming homogeneity and similarity of the turbulence properties of atmospheric surface layer flow, these eddy diffusivities were used at each measurement mast and when multiplied with the ΔC_{N_2O} values, measured fluxes were obtained for each mast. However, these measured N_2O fluxes were assigned to each subplot based on wind directions. That is, flux calculated at the mast 1 located in between plots A and B of Figure 3.2 was assigned to plot A if the wind was northerly relative to the field (that is a northerly bisector dividing the field into two). One has to remember that such an assignment of measured flux to a particular adjacent plot of a mast based on wind direction, may not necessarily reflect the actual emission rate of the plot, but provide useful information. However, to find out the actual emission rate from a particular plot, a footprint analysis is necessary. Details of such a footprint analysis is provided in the next chapter.

In this section, N_2O flux values[3] are analyzed only for the control plots, that is subplots A, C and E, and fluxes from the experimental plots (e.g. subplots B and D) are analyzed in Chapter 5. Figure 3.8 shows the N_2O flux values for the autumn experiment. Grazing periods are shown by rectangles and measurements are unavailable during these periods. Mean N_2O flux values along with standard error[4] (SE) of the total number of observations from individual instruments are shown in Table 3.2. To make a proper comparison between the flux values from two different instruments, only those observations were chosen where both CSAT3 and Gill flux values were available. The number of observations for the thermal method was much less than the parameterization method, and therefore, compared separately. Furthermore, in the following paragraphs, we will mostly focus on the flux values from the parameterization method as the thermal method is dependent on the heat flux term, $\overline{w'T'}$, which can

[2] Important findings of McMillan et al. (2012) are discussed in Appendix C

[3] Unit of the nitrous oxide flux value is expressed as: $gN_2O\text{-}N.ha^{-1}.day^{-1}$. The unit conversions are provided in Appendix D.

[4] SE = $\sigma_{fluxes}/\sqrt{N}$, where σ_{fluxes} is the standard deviation of fluxes and *N* is the number of observations. One has to remember that when parametric statistical methods (such as mean and SE) are used for a data analysis, it is inherently assumed that the data distribution is approximately normal. However, such assumption of a normal distribution may not be right and a non-parametric form of data analysis should be necessary. Since, most of the published data in this field of biogenic nitrous oxide flux values are reported using parametric statistical method, the N_2O flux values are represented here using mean and SE.

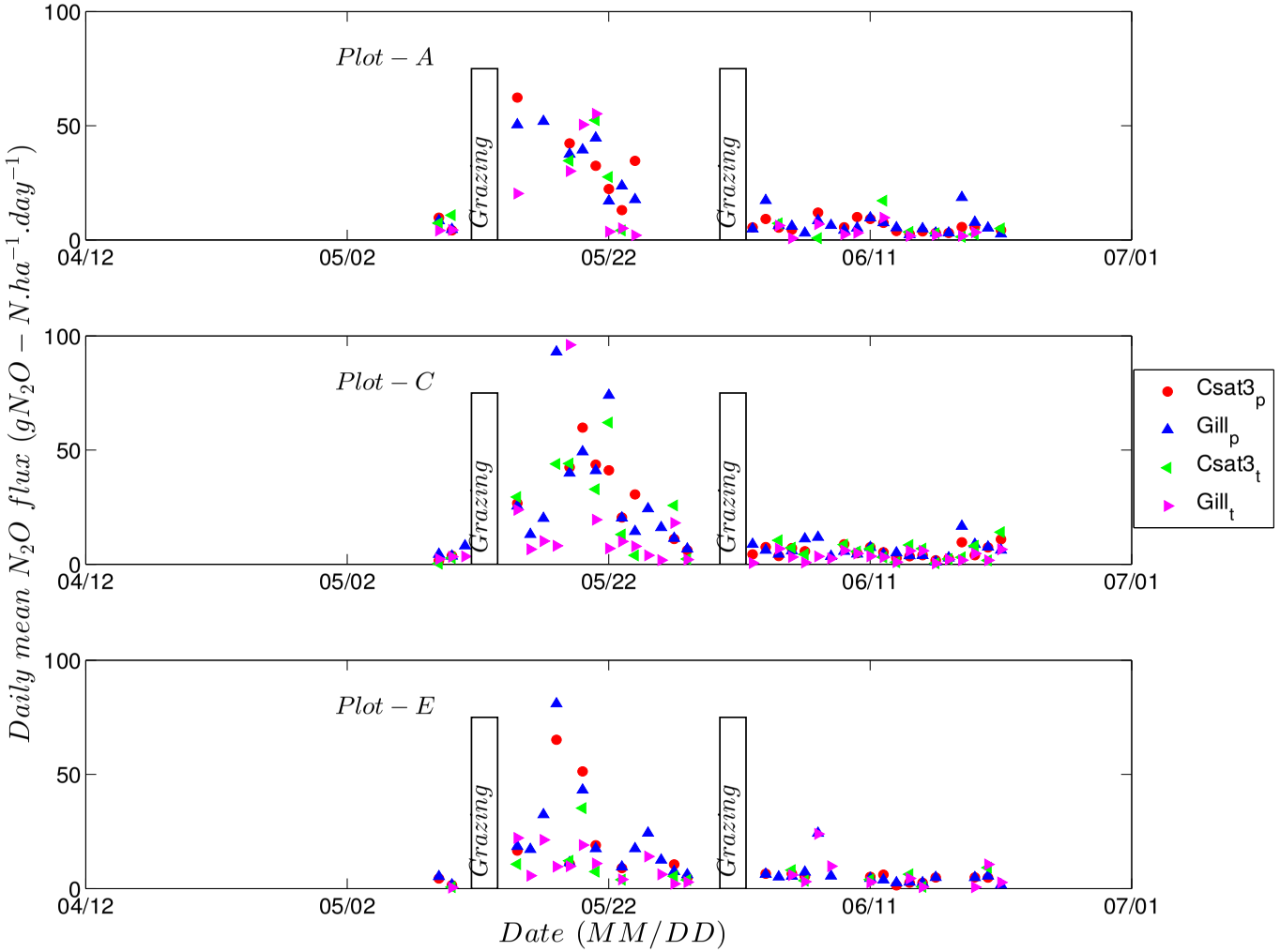

Figure 3.8: Daily mean N_2O fluxes from control subplots for the autumn experiment. Diffusivities from the CSAT3 and Gill anemometers are used with the parameterization, represented as subscript 'p', and thermal approach, represented as subscript 't'. Grazing periods are shown by rectangles. The daily mean flux values between 17 - 28 May are considerably higher than the average value of the entire period. Possible reasons may include the effect of grazing or sudden bursts of N_2O as mentioned in Harvey et al. (2008b).

have significant error accumulation during inconsistent temperature stratification.

Irrespective of measurement plots, flux values for the autumn experiment and from the parameterization method were found to vary between 0 - 191.9 $gN_2O\text{-}N.ha^{-1}.day^{-1}$. In Di et al. (2007), a similar value of 0-244 $gN_2O\text{-}N.ha^{-1}.day^{-1}$ was reported for the Lysimeter measurements of N_2O flux from over the urine patches of Lismore soil of Canterbury for late April period (Figure 2c of Di et al. (2007)). For the same method when fluxes from CSAT3 and Gill were compared, differences were found to range between 2.5-3.6%. Differences in the mean flux values were found to range between 10.8-21.5% when compared between the thermal and parameterization method. It was also evident from the R^2 values between Gill and CSAT3 fluxes derived from the parameterization method, that parameterized fluxes were more consistent (R^2 = 0.88, 0.90 and 0.96 respectively for subplots A, C and E with p-value < 0.001) and comparable than the same derived from thermal method (R^2 = 0.61, 0.72 and 0.71 for subplots A, C and E with p-value < 0.001). A higher difference in the flux values between the thermal and parameterisation methods is attributed to the higher degree of variance of the transfer coefficients from the thermal method.

Since the N_2O emission rate is highly variable spatio-temporally and very few FG-EC measurements are available over New Zealand, it is difficult to compare the flux values with previously published reports, although we have found that the mean N_2O flux values from the control plots (average of $CSAT3_p$ and $Gill_p$ for A, C and E) = 10.9 ± 0.98 $gN_2O\text{-}N.ha^{-1}.day^{-1}$ are comparable with the results of Luo et al. (2008a) of 12.0 ± 1.6 $gN_2O\text{-}N.ha^{-1}.day^{-1}$ for the autumn period. However, Luo et al. (2008a) carried out the measurement campaign using chambers and Lysimeters over urine patches. Similarly, the maximum nitrous oxide flux values of the autumn campaign were also found to be in the same range of the previously published reports of Saggar et al. (2004) who also used chambers.

Table 3.2: Mean $\pm$ Standard Error of N_2O flux values in $gN_2O\text{-}N.ha^{-1}.day^{-1}$ for autumn is summarized. Total number of observations is shown in parenthesis and mean values are computed over the total number of observations.

Sub-plots	**Mean $\pm$ S.E. N_2O flux values in $gN_2O\text{-}N.ha^{-1}.day^{-1}$**			
	$CSAT3_p$	$Gill_p$	$CSAT3_t$	$Gill_t$
Subplot-A	9.45±1.43(89)	9.19±1.27(89)	12.15±3.19(24)	8.93±2.74(24)
Subplot-C	13.76±2.35(121)	14.26±2.45(121)	13.63±3.18(45)	11.65±3.25(45)
Subplot-E	9.26±1.70 (51)	9.50±1.73 (51)	8.17±2.13(17)	7.27±1.76(17)

The spring campaign was carried out from 24 September 2010 to 20 November 2010. Mean daily flux values for this period, estimated from different instruments and

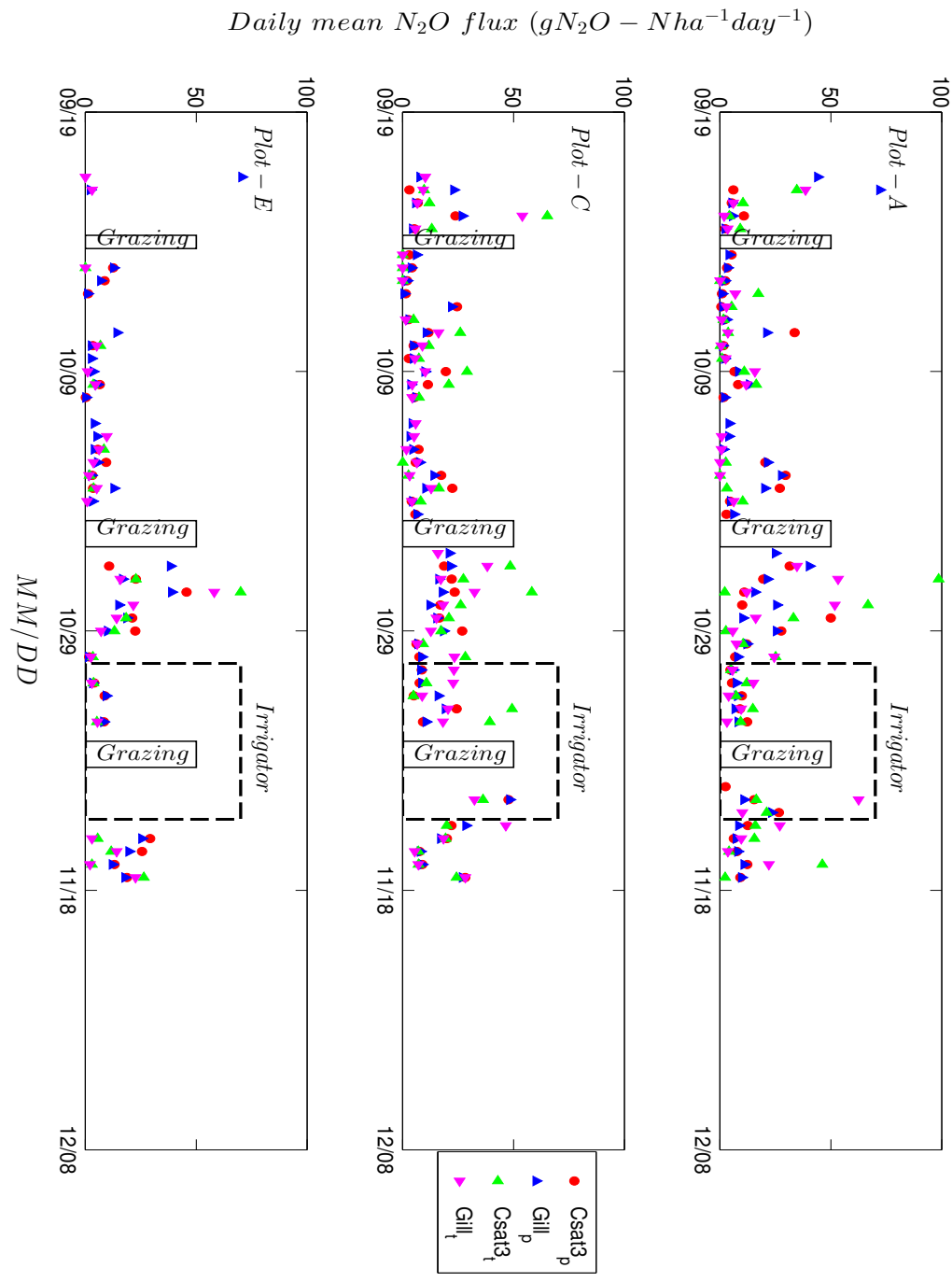

Figure 3.9: Same as Figure 3.8, but for the spring experiment with the addition of an irrigation period.

methods, are shown in Figure 3.9. Four grazing periods are shown by rectangles, and the dotted rectangle shows a period of irrigation. Similar to the autumn campaign, Table 3.3 shows the mean and standard error values of N_2O flux for the spring experiment only for those observations where both CSAT3 and Gill data were available. When the flux values were compared between CSAT3 and Gill measurements for the parameterization method, mean values were found to differ between 3.9-10.0%, marginally higher than the autumn experiment. Similar to the autumn experiment, the R^2 values between Gill and CSAT3 fluxes for subplots A, C and E were found to be 0.94, 0.98 and 0.88 for the parameterization method, whereas for the thermal method the values were 0.47, 0.93, and 0.74, with a p-value < 0.001, respectively. The significantly low value of subplot A of the thermal method was attributed to three cases of very high difference in the diffusivities from the CSAT3 and Gill measurements and these diffusivities were not removed according to our filtering criteria.

Irrespective of the measurement plots, flux values were found to vary between 0-491.8 $gN_2O\text{-}N.ha^{-1}.day^{-1}$ when compared between CSAT3 and Gill fluxes for the spring experiment of 2010. Similarly, Di and Cameron (2003) observed a maximum flux of 705 $gN_2O\text{-}N.ha^{-1}.day^{-1}$ from over the urine patches of Lismore soil of Canterbury for the spring period (Figure 4; treatment 5 of Di and Cameron (2003)). The maximum emission in the spring experiment was found to be much higher than the autumn experiment and this trend of seasonal variation was reported previously by Di and Cameron (2003) and Saggar et al. (2004). Soil moisture content, specifically wetter soil in spring after a rainy winter, was found to be the controlling factor for such seasonal variation (Saggar et al., 2004). Again, when the mean N_2O flux values from the control plots (average of $CSAT3_p$ and $Gill_p$ for A, C and E) = 11.7 ± 0.57 $gN_2O\text{-}N.ha^{-1}.day^{-1}$ were compared with the results of Saggar et al. (2004) of 33.5 ± 16.1 $gN_2O\text{-}N.ha^{-1}.day^{-1}$ for the spring period, significantly low values were observed. However, the soil type of Saggar et al. (2004) were sandy-Loam and silt-Loam and the measurements were made after intense grazing.

Table 3.3: Mean $\pm$ Standard Error N_2O flux values in $gN_2O\text{-}N.ha^{-1}.day^{-1}$ for spring. Total number of observations is shown in parenthesis and mean values are computed over the total number of observations.

Sub-plots	**Mean $\pm$ S.E. N_2O flux values in $gN_2O\text{-}N.ha^{-1}.day^{-1}$**			
	$CSAT3_p$	$Gill_p$	$CSAT3_t$	$Gill_t$
Subplot-A	$10.65\pm1.08(220)$	$10.25\pm0.97(220)$	$15.56\pm2.69(88)$	$9.92\pm1.54(88)$
Subplot-C	$11.94\pm1.18(280)$	$10.90\pm1.05(280)$	$26.14\pm6.38(45)$	$19.92\pm4.82(114)$
Subplot-E	13.94 ± 1.55 (73)	12.67 ± 1.38 (73)	$14.91\pm3.41(45)$	$12.64\pm2.77(45)$

Stability and Flux : Flux values from the parameterization and thermal methods are compared here in relation to atmospheric stability which provides the opportunity to identify differences between the estimation techniques with different atmospheric stratifications. Therefore, instead of performing a seasonal analysis, only the spring data from the Gill anemometer were used, as the total number of observations in spring was higher than autumn. Furthermore, all the flux observations from plots A, C and E were combined. Therefore, a total of 857 flux values from the parameterization method and 386 flux values from the thermal method were explored. Figure 3.10 shows N_2O flux values as a function of stability parameter ($1/L$). Most of the high flux values were observed during -0.1 $\leq (1/L) \leq$ 0.1 and the highest flux values were obtained using the thermal method. Flux values from the thermal method were always found to be higher than the parameterization method. During stable atmospheric conditions ($1/L > 0.1$), the average difference between the thermal and parameterization methods was found to be 5.8 $gN_2O\text{-}N.ha^{-1}.day^{-1}$ (p-value > 0.05) which reduces to 2.0 $gN_2O\text{-}N.ha^{-1}.day^{-1}$ during neutral atmospheric conditions ($|1/L| < 0.04$) which was also statistically insignificant (p-value > 0.05). The average difference of 17.9 $gN_2O\text{-}N.ha^{-1}.day^{-1}$ in flux values of the thermal and parameterization methods was observed during unstable periods ($1/L <$ -0.1) which was significant as p-value < 0.01.

Similarly, differences in the flux values between thermal and parameterized values were also evaluated for a range of friction velocity values. It was observed that for $u_\star < 0.2$ m s^{-1}, the average difference between the fluxes was 6.8 $gN_2O\text{-}N.ha^{-1}.day^{-1}$. Similarly for $0.2 < u_\star < 0.5$ m s^{-1} it was 5.2 $gN_2O\text{-}N.ha^{-1}.day^{-1}$, and for $u_\star > 0.5$ m s^{-1} it was 9.8 $gN_2O\text{-}N.ha^{-1}.day^{-1}$. That is, for very high friction velocity cases, flux values from the thermal method were lower than fluxes from the parameterization method. However, differences in the flux values for the low wind speed conditions ($u_\star < 0.2$ m s^{-1}) were found to be statistically significant, p-value < 0.01.

3.5.6 Uncertainties in transfer coefficients

As was mentioned in Chapter 1, one of the objectives of this study is to provide an uncertainty estimate of the measured flux values. Consequently, a random relative error analysis is performed for the micrometerological approach described in this section and later in the thesis. During the error analysis procedure, the effect of systematic errors (Mahrt, 1998) and the footprint heterogeneity error (Moncrieff et al., 1996) will be neglected. The sole purpose of this error analysis will therefore be to estimate and

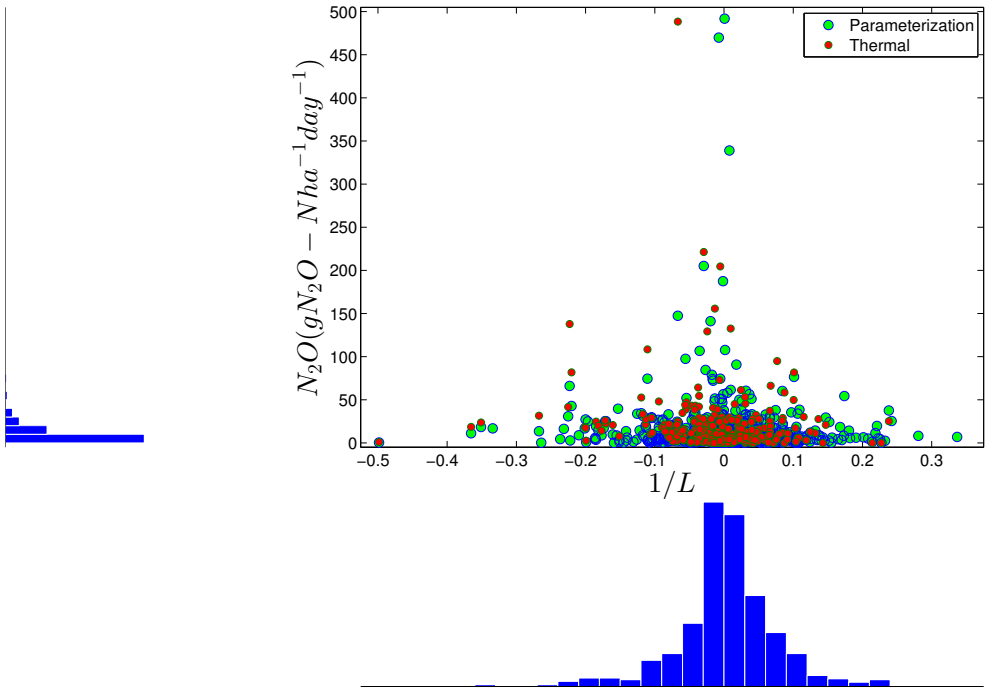

Figure 3.10: Scatter-histogram of flux values represented as a function of the stability parameter ($1/L$). Green circles are fluxes from the parameterization method and red circles are fluxes from the thermal method.

explore random error propagation in the final flux values through the transfer coefficients.

For a coupled FG-EC method of flux estimation, flux values are dependent on EC measurements as the transfer coefficients are deduced based on them. Therefore, uncertainty in the EC measurement propagates error in the final flux value through the transfer coefficients, along with the uncertainty in the concentration measurements. To assess error propagation through the transfer coefficients of the FG-EC system, in the following section, k_h^t and d_h^p will be expressed using relatively simple variables and length scales (such as $u_\star$ and L), so that these dependencies can be used to estimate absolute and relative errors in the final flux values. The final relative error estimates of k_h^t and d_h^p will be made after correcting some of the biases, such as non-stationarity of the data and density corrections which were discussed in Section 3.4.1.

Errors in the estimation of k_h^t: k_h^t is a function of the heat flux term $\overline{w'T'}$ (m s$^{-1}{}^\circ C$), the temperature difference term ΔT ($^\circ C$) and height difference term Δz (m). Therefore, absolute and relative error in k_h^t can be expressed using the absolute and relative error equations (Taylor, 1997; Abramowitz and Stegan, 2002) as:

$$\left.\begin{aligned} \delta k_h^t &= \left(\frac{\partial k_h^t}{\partial \overline{w'T'}}\right)\delta\overline{w'T'} + \left(\frac{\partial k_h^t}{\partial \Delta T}\right)\delta\Delta T + \left(\frac{\partial k_h^t}{\partial \Delta z}\right)\delta\Delta z \\ \frac{\delta k_h^t}{k_h^t} &= \left(\frac{\partial k_h^t}{\partial \overline{w'T'}}\right)\left(\frac{\delta\overline{w'T'}}{k_h^t}\right) + \left(\frac{\partial k_h^t}{\partial \Delta T}\right)\left(\frac{\delta\Delta T}{k_h^t}\right) + \left(\frac{\partial k_h^t}{\partial \Delta z}\right)\left(\frac{\delta\Delta z}{k_h^t}\right) \end{aligned}\right\} \quad (3.8)$$

Using Equation 3.2, partial terms in Equation 3.8 can be estimated, and the relative error of k_h^t can be expressed as:

$$\frac{\delta k_h^t}{k_h^t} = \sqrt{\left(\frac{\delta\overline{w'T'}}{\overline{w'T'}}\right)^2 + \left(\frac{\delta\Delta T}{\Delta T}\right)^2 + \left(\frac{\delta\Delta z}{\Delta z}\right)^2} \quad (3.9)$$

These three terms in the right hand side of Equation 3.9 represent relative errors in heat flux, temperature difference and height difference, respectively. Similarly, errors in d_h^p can be estimated for *z/L* ≥ 0 and *z/L* < 0 cases.

Errors in the estimation of d_h^p (z/L $\geq$ 0): Estimation of the absolute and relative error in d_h^p is more complicated as d_h^p can be expressed as $d_h^p = (\kappa u_\star)/J$, where *J* depends on the stability function ψ_h, which is represented differently for $z/L \geq 0$ and $z/L < 0$ cases (Equation 3.5). The regular form of d_h^p can be expressed as:

$$d_h^p = \frac{\kappa u_\star}{ln(\frac{z_2-d}{z_1-d}) - \psi_h(\frac{z_2-d}{L}) + \psi_h(\frac{z_1-d}{L})} \quad (3.10)$$

Now for $z/L \geq 0$ the above equation can be modified as:

$$d_h^p = \frac{\kappa u_\star}{ln(\frac{z_2-d}{z_1-d}) + 7.8(\frac{z_2-d}{L}) - 7.8(\frac{z_1-d}{L})} \quad (3.11)$$

Since z_1, z_2, and *d* have fixed values throughout an experimental period or individual campaign, the term $ln\frac{z_2-d}{z_1-d}$ can be represented as a constant, *C*. Similarly, two other constants can be defined as $C_1 = 7.8(z_1 - d)$ and $C_2 = 7.8(z_2 - d)$ and Equation 3.11 can be expressed as:

$$d_h^p = \frac{\kappa u_\star L}{CL + C_2 - C_1} \quad (3.12)$$

Again constant C_3 can be defined by subtracting C_1 from C_2 and d_h^p can be expressed as:

$$d_h^p = \frac{\kappa u_\star L}{CL + C_3} \tag{3.13}$$

Furthermore, constants C_4 and C_5 can be defined following $C_4 = C/\kappa$ and $C_5 = C_3/\kappa$ and d_h^p can be represented as:

$$d_h^p = \frac{u_\star L}{C_4 L + C_5} \tag{3.14}$$

Now, we can see that Equation 3.14 becomes a simplified version of Equation 3.11 and d_h^p is represented as a function of $u_\star$ and L. Hence, the relative error estimation of d_h^p becomes easier and a final form of the relative error in d_h^p can be obtained as:

$$\frac{\delta d_h^p}{d_h^p} = \left(\frac{\partial d_h^p}{\partial u_\star}\right)\delta u_\star + \left(\frac{\partial d_h^p}{\partial L}\right)\delta L \tag{3.15}$$

Finally, from the partial terms of Equation 3.15, the relative error in d_h^p can be expressed as:

$$\frac{\delta d_h^p}{d_h^p} = \sqrt{\left(\frac{\delta u_\star}{u_\star}\right)^2 + \left(\frac{C_5}{C_4 L + C_5}\right)^2 \left(\frac{\delta L}{L}\right)^2} \tag{3.16}$$

Errors in the estimation of d_h^p ($z/L < 0$) For $z/L < 0$, d_h^p can be expressed as:

$$d_h^p = \frac{\kappa u_\star}{ln(\frac{z_2 - d}{z_1 - d}) - 2ln(\frac{1+y_2}{2}) + 2ln(\frac{1+y_1}{2})} \tag{3.17}$$

where y_1 = 0.95(1-11.6$\frac{z_1-d}{L}$)$^{1/2}$ and y_2 = 0.95(1-11.6$\frac{z_2-d}{L}$)$^{1/2}$. Using the same notations for the constant values from Equation 3.12, d_h^p for $z/L < 0$ can be expressed as:

$$d_h^p = \frac{\kappa u_\star}{C - 2ln(\frac{1+y_2}{1+y_1})} \tag{3.18}$$

and finally as:

$$d_h^p = \frac{u_\star}{C_4 - C_6 ln(\frac{1+y_2}{1+y_1})} \tag{3.19}$$

where C_4 is the same as that of Equation 3.14 and C_6 = 2/κ. Further expansions of y_1 and y_2 are also possible, but the functional expression of d_h^p is restricted up to this equation and absolute error in d_h^p is expressed as a function of $u_\star$ and

$\left[C_4 - C_6 ln(\frac{1+y_2}{1+y_1})\right]$ as:

$$\delta d_h^p = \left(\frac{\partial d_h^p}{\partial u_\star}\right)\delta u_\star + \left(\frac{\partial d_h^p}{\partial(C_4 - C_6 ln(\frac{1+y_2}{1+y_1}))}\right)\delta\left(C_4 - C_6 ln(\frac{1+y_2}{1+y_1})\right) \tag{3.20}$$

Finally, substituting the partial terms with variables, the relative error of d_h^p for $z/L < 0$ can be expressed as:

$$\frac{\delta d_h^p}{d_h^p} = \sqrt{\left(\frac{\delta u_\star}{u_\star}\right)^2 + \left(\frac{\delta\left(C_4 - C_6 ln(\frac{1+y_2}{1+y_1})\right)}{C_4 - C_6 ln(\frac{1+y_2}{1+y_1})}\right)^2} \tag{3.21}$$

Equations 3.9, 3.16, and 3.21 have been used in Section 3.5.7 for estimating errors in the eddy diffusivity parameters. Since z is always positive for our study and inverse Obukhov length ($1/L$, m^{-1}) can also be used as a stability parameter, $z/L \geq 0$ and $z/L < 0$ terms are synonymously used with $1/L \geq 0$ and $1/L < 0$ cases, respectively.

3.5.7 Measure of uncertainty in transfer coefficient terms

Uncertainty in k_h^t and d_h^p terms are estimated in this section based on the relationships described in Section 3.5.6. Therefore, Equations 3.9, 3.16 and 3.21 are used. Traditionally, random relative error in the flux values are estimated following the equation provided by Mahrt (1998). However, the measurement uncertainty can also be characterized by estimating the standard deviation of multiple measurements. The initial uncertainty estimates of $\overline{w'T'}$, ΔT, $u_\star$ and L dependent terms, in this study, are made based on a realistic assumption and mostly from values provided in Laubach and Kelliher (2004). Afterward, time averaged samples of individual variables from the CSAT3 and Gill anemometer are used to estimate the final relative error in the transfer coefficients ($\delta k_h^t/k_h^t$ and $\delta d_h^p/d_h^p$). The nature of the error distribution in both $\delta k_h^t/k_h^t$ and $\delta d_h^p/d_h^p$ are also evaluated, so that they can be used in the next section for a Monte-Carlo type simulation.

Errors in k_h^t: From Equation 3.9, we know that relative error in k_h^t depends on $\delta\overline{w'T'}/\overline{w'T'}$, $\delta\Delta T/\Delta T$, and $\delta\Delta z/\Delta z$, and we also know that $\overline{w'T'}$ has a decreasing trend with increasing 1/*L*, and ΔT changes sign from positive to negative during transition from highly stable to highly unstable conditions. Therefore, for an initial un-

certainty in $\overline{w'T'}$ and ΔT, relative errors, $\delta\overline{w'T'}/\overline{w'T'}$ and $\delta\Delta T/\Delta T$, will depend on the variations of $\overline{w'T'}$ and ΔT with 1/*L*. Since uncertainty in the measurement height is fixed and very small, as $\delta\Delta z/\Delta z$ = 0.005 for Δz = 0.5 m and $\delta\Delta z$ of the order of 0.0025 m, for an entire experimental campaign, we neglect the term $\delta\Delta z/\Delta z$. For both of the sonic anemometers, if the uncertainty in $\overline{w'T'}$ is assumed to be 0.0001 m s^{-1}°C, and for the temperature sensors uncertainty in ΔT is assumed to be 0.005 °C, $\delta k_h^t/k_h^t$ can be estimated for both seasons. This initial uncertainty assumption of the covariance and temperature difference terms is only a sensible guess within a realistic range and comparable to the relative error estimates of Laubach and Kelliher (2004).

Table 3.4 shows the mean uncertainty of $\delta k_h^t/k_h^t$, including contributions from individual terms. '<>' indicates the mean values for each campaign. Irrespective of the season and sensor, and for the predefined initial uncertainty in ΔT and $\overline{w'T'}$, uncertainty in k_h^t was found to vary between 5.5 - 9.8%. Night time errors were found to be higher than day time values for both sensors and seasons. $< \delta k_h^t/k_h^t >$, irrespective of sensor, was found to be approximately 0.09 for day time and 0.11 for night time during the autumn experiment and 0.05 and 0.10 for the spring experiment, respectively. Therefore, approximately, a 2-5% increase in the total random error in k_h^t was observed for the night time periods. Furthermore, the modality of $\delta k_h^t/k_h^t$ was also tested using a Dip unimodality test of Hartigan and Hartigan (1985) so that an appropriate distribution can be fitted to the data during Monte-Carlo simulation. The Dip scores are used to test the null hypothesis of unimodality against the alternative hypothesis of multimodality of a sample. If a Dip score has a p-value < 0.05, the hypothesis of unimodality in the data is rejected. For the $\delta k_h^t/k_h^t$ values of this case, a Dip score of 0.01 was observed with a p-value > 0.99 indicating a unimodality of the data.

Table 3.4: Mean uncertainty in the diffusivity parameter k_h^t for $\delta\overline{w'T'} = 0.0001$ m s^{-1}°C and $\delta\Delta T$ = 0.005 °C. $< |\frac{\delta\overline{w'T'}}{\overline{w'T'}}| >$ and $< |\frac{\delta\Delta T}{\Delta T}| >$ represents the mean relative error in the heat flux and temperature difference term.

Seasons	$< \frac{\delta k_h^t}{k_h^t} >$		$< \lvert\frac{\delta\overline{w'T'}}{\overline{w'T'}}\rvert >$		$< \lvert\frac{\delta\Delta T}{\Delta T}\rvert >$	
	CSAT3	Gill	CSAT3	Gill	CSAT3	Gill
Autumn	0.08	0.09	0.05	0.06	0.05	0.06
Spring	0.05	0.07	0.02	0.04	0.04	0.04

Errors in d_h^p (1/L $\geq$ 0): Error in d_h^p for the $1/L \geq 0$ case was evaluated using Equation 3.16 and hence, constants of Equations 3.12 to 3.16, C and C_1 to C_5, were estimated for a displacement height, *d* = 0.066 m, and measurement heights, z_1 = 0.478 m and z_2

= 1.41 m. These values were C = 1.18, C_1 = 3.21 m; C_2 = 10.48 m; C_3 = 7.27 m; C_4 = 2.95; and C_5 = 18.175 m. Now, similar to the above case, when we assume an initial uncertainty of $\delta u_\star = 0.01$ m s^{-1} and $\delta L = 0.5$ m following Laubach and Kelliher (2004), variations in $\delta d_h^p/d_h^p$ as a function of L and $u_\star$ can be obtained. Variability of $\delta d_h^p/d_h^p$, obtained from both CSAT3 and Gill anemometer observations in autumn, is shown in Figure 3.11. Similar trends were also observed for spring measurements. Table 3.5 summarises the mean uncertainty values of individual terms of d_h^p. Irrespective of sensor and season, and for the above mentioned initial uncertainty, errors in d_h^p were found to vary between 6-8% for this case.

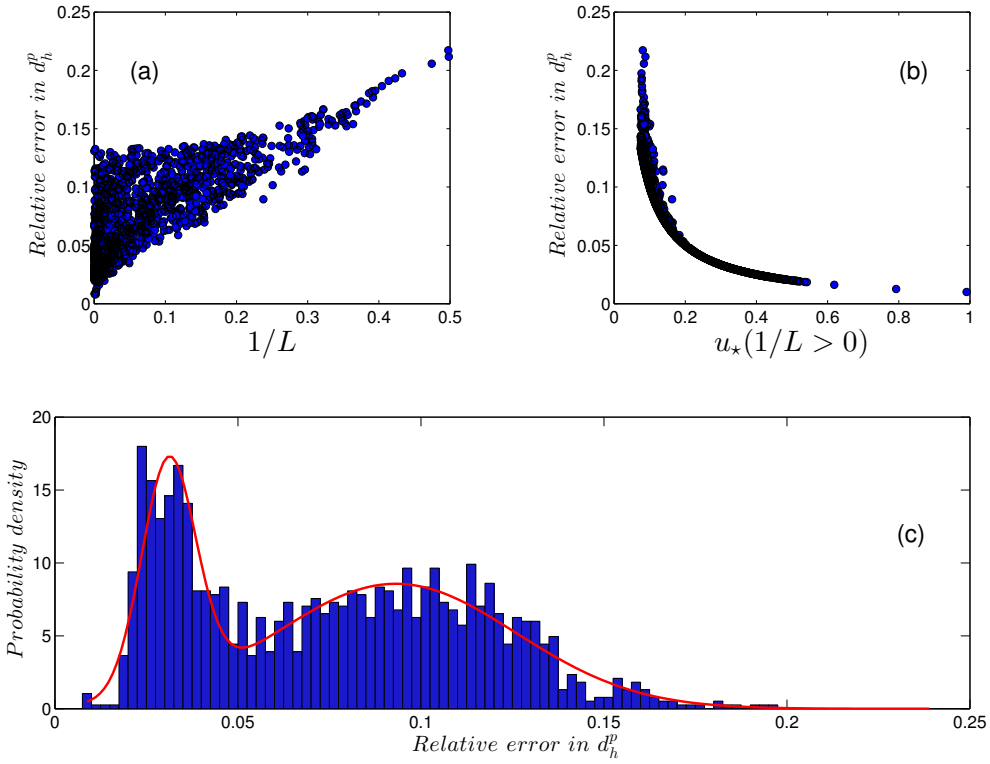

Figure 3.11: The relative error in d_h^p, $\delta d_h^p/d_h^p$, for $1/L \geq 0$ shown as a function of (a) inverse Obukhov length ($1/L$) and (b) $u_\star$ for autumn from both CSAT3 and Gill observations. A fitted pdf of the relative error in d_h^p is shown in the lower panel (c).

The probability density function (pdf) of $\delta d_h^p/d_h^p$ for all the autumn observations, shown in the lower panel of Figure 3.11, indicates that the errors are bimodal, with two distinct clusters at around 0.03-0.04 and 0.08-0.12. Now, to check the bimodality of the data distribution, the Dip unimodality test of Hartigan and Hartigan (1985) was carried out and a Dip score of 0.04 was obtained with a p-value < 0.001. Although the Dip score is smaller than a Dip score of $\approx$0.08-0.1 (p-value < 0.001) of a purely bimodal distribution, this value is good enough to show the partial bimodal character of the

data (Freeman and Dale, 2012). Since no standard probability density function (pdf) was available to fit the data, a mixture of two normally distributed pdfs were coupled. This coupled pdf was a weighted sum of the pdfs of two normal components, weighted by the mixture probability. An anonymous function was defined in the commercial mathematical software MATLAB (www.mathworks.com) with an equal mixture of normals, centred at the two quartiles of the data, with equal standard deviations. With this initial guess, maximum likelihood optimization was carried out for 200 iterations and parameters of this unique pdf were estimated. This bimodal distribution was then fitted to the relative error term and displayed with a red line in Figure 3.11c. This is a standard procedure for fitting a coupled pdf of normals to a bimodal data distribution and details can be found in McLachlan and Peel (2000).

Table 3.5: Mean uncertainty in the diffusivity parameter d_h^p for $1/L > 0$ cases for $\delta u_\star = 0.01$ m s^{-1} and $\delta L = 0.5$ m are shown here. $< |\frac{\delta u_\star}{u_\star}| >$ represents the mean relative error contribution from $u_\star$ and $< |\frac{\delta L}{L}| >$ represents the mean relative error from L.

Seasons	$< \frac{\delta d_h^p}{d_h^p} >$		$< |\frac{\delta u_\star}{u_\star}| >$		$< |\frac{\delta L}{L}| >$	
	CSAT3	Gill	CSAT3	Gill	CSAT3	Gill
Autumn	0.08	0.07	0.07	0.06	0.05	0.02
Spring	0.06	0.06	0.05	0.05	0.03	0.02

Errors in d_h^p (1/L $<$ 0): The relative error in d_h^p for $1/L < 0$ was expressed as the cumulative uncertainty between $u_\star$ and a stability dependent term $C_4 - C_6 ln((1 + y_2)/(1 + y_1))$ in Equation 3.21. Now, for the same measurement and displacement heights mentioned above, C_6 was found to be 5.0, C_4 was found to be 2.95 and the uncertainty term was represented as $[2.95 - 5ln((1+y_2)/(1+y_1))]$. Although y_1 and y_2 are non-linear functions of $(z-d)/L$, further expansion of this term is possible. In this present case, the term $[2.95 - 5ln((1+y_2)/(1+y_1))]$ was used to estimate uncertainty in the diffusivity parameter and no further expansions were carried out. Now, for an initial uncertainty of $\delta u_\star$ = 0.01 m s^{-1} and $\delta(C_4 - C_6 ln((1 + y_2)/(1 + y_1)))$ = 0.1, variation in $\delta d_h^p/d_h^p$ with $1/L$ and $u_\star$ was evaluated and is shown in the upper panel of Figure 3.12. Table 3.6 shows the mean variation of each term for both seasons and sensors. It is evident from Table 3.6 that uncertainty in the $u_\star$ is the most important source of error in d_h^p and the average $\delta d_h^p/d_h^p$ is of the order of 0.075. Again, when the modality of $\delta d_h^p/d_h^p$ was tested following the Hartigan and Hartigan (1985), a Dip score of 0.016 was obtained with a p-value > 0.9, showing an approximate unimodality of the data.

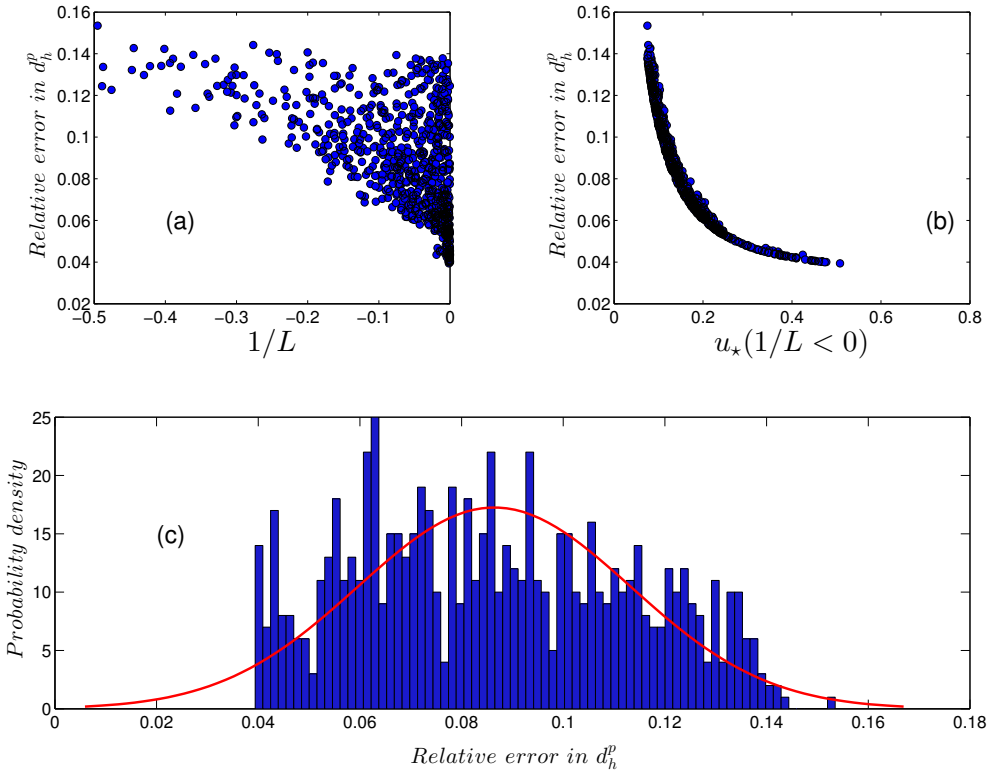

Figure 3.12: Relative error in d_h^p for $1/L < 0$ shown as a function of (a) $1/L$ and (b) $u_\star$ for autumn, obtained from both CSAT3 and Gill observations. A fitted pdf of the relative error in d_h^p for $1/L < 0$ cases is shown in the lower panel (c).

Table 3.6: Mean uncertainties in the diffusivity parameter d_h^p for $1/L < 0$ cases are shown here and are obtained using $\delta u_\star = 0.01$ m s^{-1} and $\delta(C_4 - C_6 ln(\frac{1+y_2}{1+y_1})) = 0.1$ m. Term $< |\frac{\delta u_\star}{u_\star}| >$ signifies the mean relative error from $u_\star$ whereas $< |\frac{\delta(C_4 - C_6 ln(\frac{1+y_2}{1+y_1}))}{(C_4 - C_6 ln(\frac{1+y_2}{1+y_1}))}| >$ represents the mean relative error from the stability dependent term.

Seasons	$< \frac{\delta d_h^p}{d_h^p} >$		$< \|\frac{\delta u_\star}{u_\star}\| >$		$< \|\frac{\delta(C_4 - C_6 ln(\frac{1+y_2}{1+y_1}))}{(C_4 - C_6 ln(\frac{1+y_2}{1+y_1}))}\| >$	
	CSAT3	Gill	CSAT3	Gill	CSAT3	Gill
Autumn	0.09	0.08	0.08	0.07	0.04	0.04
Spring	0.06	0.07	0.05	0.05	0.04	0.04

3.5.8 Error sensitivity study using a Monte-Carlo type method

In the previous section, error variance in k_h^t and d_h^p was estimated using only a single uncertainty estimate of the individual variables contributing to the transfer coefficients. An approximate unimodal distribution was found for $\delta k_h^t / k_h^t$ and $\delta d_h^p / d_h^p$ for the $1/L < 0$ cases, whereas a partial bimodal distribution was found for $\delta d_h^p / d_h^p$ for $1/L \geq 0$ case. Propagation of errors from the individual terms to $\delta k_h^t / k_h^t$ and $\delta d_h^p / d_h^p$ was also tested for a single initial uncertainty. However, since the initial uncertainty estimate can also

vary for the individual terms of k_h^t and d_h^p, a probabilistic estimation of error in k_h^t and d_h^p is necessary for a wider range of initial uncertainties in the contributing terms of k_h^t and d_h^p. Therefore, a Monte-Carlo type simulation has been performed in this section.

To perform this Monte-Carlo analysis, a synthetic population of $\delta k_h^t/k_h^t$ and $\delta d_h^p/d_h^p$ for $1/L < 0$ cases were produced from the stochastic combination of normally distributed random numbers assumed as initial uncertainties. These normally distributed random numbers were produced using a mean and standard deviation value of error in the individual contributing terms of each transfer coefficient. For example, an error population of $\delta k_h^t/k_h^t$ was produced by stochastically fitting 1000 normally distributed random numbers to the Equation 3.9 where random numbers were produced individually using a mean $\delta\overline{w'T'}$ = 0.0005 and $\sigma_{\delta\overline{w'T'}}$ = 0.0002, and mean $\delta\Delta T$ = 0.005 and $\sigma_{\delta\Delta T}$ = 0.002. It should be noted that each of these 1000 initial uncertainties were tested against a length of observations (n) and hence, a matrix of 1000 $\times$ n values of relative errors were produced.

Similarly, a 1000 $\times$ n population of $\delta d_h^p/d_h^p$ of $1/L < 0$ case was produced by stochastically fitting 1000 normally distributed random numbers to Equation 3.21, where random numbers were produced using a mean $\delta u_\star$ = 0.01 and $\sigma_{\delta u_\star}$ = 0.005 m s^{-1} and a mean $C_4 - C_6 ln((1+y_2)/(1+y_1))$ = 0.1, and $\sigma_{C_4 - C_6 ln((1+y_2)/(1+y_1))}$ = 0.05.

For the d_h^p from the $1/L \geq 0$ case, since a partially bimodal distribution in $\delta d_h^p/d_h^p$ was observed, a population of $\delta d_h^p/d_h^p$ was produced by stochastically fitting 1000 random numbers to Equation 3.16, where random numbers were generated from two different normal distributions with marginally different mean and standard deviation values, so that this distribution can be assumed to be the mixed pdf mentioned in the previous section. These error populations are further evaluated in the next section.

Error sensitivity of $\delta k_h^t/k_h^t$: As mentioned earlier, using a total of 784 observations, a matrix of 1000 $\times$ 784 $\delta k_h^t/k_h^t$ values were produced, and for each initial uncertainty a mean $\delta k_h^t/k_h^t$ can be estimated from the ensembles of errors. These mean errors can then be represented as a function of the observed $\overline{w'T'}$ and ΔT values to explore the dependency of the error on the individual terms. Figure 3.13 shows such a variation of the mean $\delta k_h^t/k_h^t$. It is evident from the figure that mean $\delta k_h^t/k_h^t$ increases rapidly as both $\overline{w'T'}$ and $\Delta T \mapsto 0$. Again, it was found that when $\Delta T \leq$ -0.2, $\delta k_h^t/k_h^t$ could vary between 0.005 - 0.80, while for $\Delta T \geq 0.2$, $\delta k_h^t/k_h^t$ could vary between 0.009 - 0.63. For $\overline{w'T'} \leq$ -0.02, $\delta k_h^t/k_h^t$ was found to vary between 0.009-0.15; and for $\overline{w'T'} \geq 0.02$,

it varied between 0.006-0.09.

Uncertainty in the ΔT was found to contribute more toward the relative error than the uncertainty in $\overline{w'T'}$ and an ensemble mean uncertainty of $\delta k_h^t/k_h^t$ was found to be 0.62. The ensemble mean value of $\delta k_h^t/k_h^t$ was much higher than the uncertainty estimation of other transfer coefficients and this can be attributed to some extremely high uncertainty cases produced for observations with $|\Delta T| < 0.01$ and $|\overline{w'T'}| < 0.001$. It is also evident from Equation 3.2 that as $\Delta T \mapsto 0$ and $[\Delta T, \overline{w'T'}] \mapsto 0$, $k_h^t \mapsto \infty$. Therefore, when the ensemble mean of $\delta k_h^t/k_h^t$ was estimated for those cases where $|\Delta T| > 0.01$ and $|\overline{w'T'}| > 0.001$ (79.7% cases), ensemble mean uncertainty of $\delta k_h^t/k_h^t$ was reduced to 0.15.

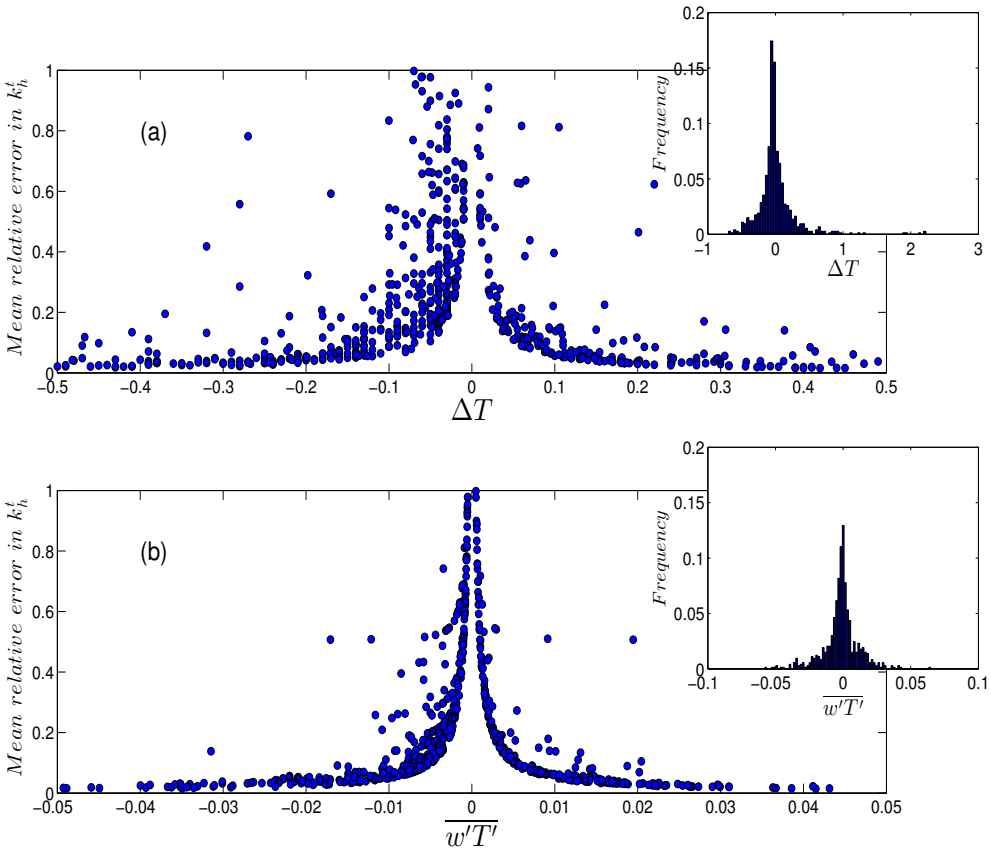

Figure 3.13: The upper panel shows the scaled relative error in k_h^t as a function of ΔT with the histogram of observed ΔT at the corner. The lower panel shows the scaled relative error in k_h^t as a function of $\overline{w'T'}$ with the histogram of the observed $\overline{w'T'}$. Observed values are from the autumn experiment.

Error sensitivity of $\delta d_h^p/d_h^p$ for the $1/L \geq 0$ case: A total of 880 observations of $u_\star$ and L were used for one set of initial uncertainty in $u_\star$ and L, and 1000 $\times$ 880 such

ensembles were constructed. As we mentioned earlier, for this case random numbers were generated by coupling two normally distributed random number series and these random numbers were assumed to be initial uncertainties in $u_\star$ and L. From the 1000 $\times$ 880 population of $\delta d_h^p/d_h^p$, 1000 mean $\delta d_h^p/d_h^p$ were estimated and the range of relative errors in d_h^p was found to be smaller than the relative error of k_h^t. Averages of the total sample of $\delta d_h^p/d_h^p$ were found to vary between 0.001-0.17, whereas maximum values were found to vary between 0.002-0.49, and minimum values were found to vary between 0.0001-0.05. Again when the frequency distribution of all the elements of 1000 $\times$ 880 matrix of $\delta d_h^p/d_h^p$ was explored, as shown in Figure 3.14a, 24.6% of the mean $\delta d_h^p/d_h^p$ were found to be within 0.02 to 0.047 and only 0.3% of $\delta d_h^p/d_h^p$ were found to be greater than 0.295. Each bin size of the histogram was 0.0078. Contribution to the total uncertainty in $d_h^p$was found to be higher for $\delta u_\star$ than δL. Finally, including all the ensembles and all the observation points, the ensemble mean of $\delta d_h^p/d_h^p$ was found to be 0.09$\pm$0.03. The standard deviation value was obtained by repeating the entire procedure 10 times.

Error sensitivity of $\delta d_h^p/d_h^p$ for the $1/L < 0$ case: For a total of 460 observations of $u_\star$ and L, a total of 1000 $\times$ 460 observations of $\delta d_h^p/d_h^p$ were produced and 1000 mean $\delta d_h^p/d_h^p$ values were estimated. The histogram of all the samples for $1/L < 0$ is shown in Figure 3.14b. The bin size of this diagram is the same as that mentioned above (0.0078) and 35.75% of the total $\delta d_h^p/d_h^p$ was found to vary between 0.023 and 0.053. The narrower range of the pdf of this case indicates a lesser degree of uncertainty. For each ensemble, the mean relative error was found to vary between 0.03-0.13. Similarly, maximum values were found to vary between 0.08-0.35, while minimum values were found to vary between 0.00009-0.01. Finally, including all the ensembles and all the observation points, average $\delta d_h^p/d_h^p$ for this case was found to be 0.067$\pm$0.02.

The pdf of the error anomalies ($\delta d_h^p/d_h^p - \overline{\delta d_h^p/d_h^p}$) for different stability cases are shown in the lower panel of Figure 3.14. It is evident that the error variance in d_h^p is higher during stable atmospheric conditions than the convective cases. Again, the kurtosis values of stable and unstable error anomalies were found to be 2.93 and 2.86, respectively. These values are close to the value of 3 for a normal distribution, although, a marginally smaller value of 2.86 of error anomaly for unstable cases implies a lesser possibility of outliers.

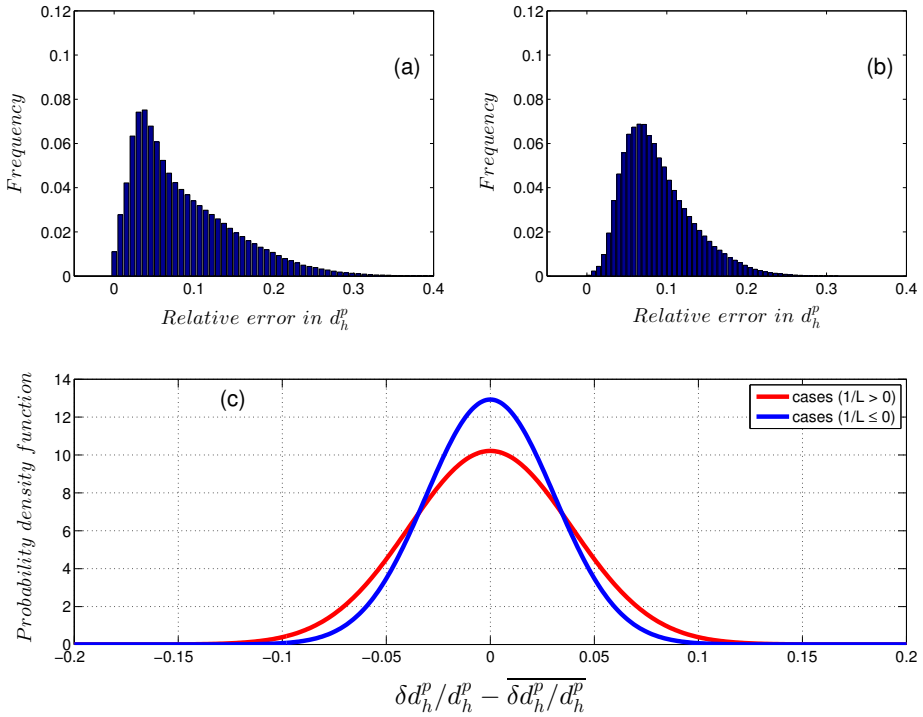

Figure 3.14: The left upper-panel (a) shows the histogram of $\delta d_h^p/d_h^p$ for $1/L \geq 0$ and right upper-panel (b) panel shows the same for $1/L < 0$ cases. Bin size for both the histograms is 0.0078. The lower panel (c) shows the pdfs of the error anomalies for different stability cases.

3.5.9 Measure of uncertainty in the nitrous oxide concentration difference term

Since one of the purposes of this study is to find the total propagated error in the N_2O flux values measured during the described field campaigns, a random error analysis of the measured concentration values of N_2O is carried out here and a total random error estimate of the measured fluxes is provided in the following section. As mentioned earlier, the procedure of error estimation mentioned here is generic and can be applied to any entity measured using the FG-EC method. However, the magnitude of the uncertainty obtained for the N_2O concentration measurement can vary for other constituents.

As mentioned earlier, two flux gradient gas inlets were used to collect air samples and concentration differences of N_2O (ΔC_{N_2O}) were obtained using the TDL. Most of these ΔC_{N_2O} values, irrespective of season, were found to be positive and less than 1 ppb (Figure 3.15 a and b). Again, the ΔC_{N_2O} values were also found to be highly sensitive to $1/L$ and the variances in the ΔC_{N_2O} values were found to gradually increase with increasing stability, as shown in Figure 3.15c.

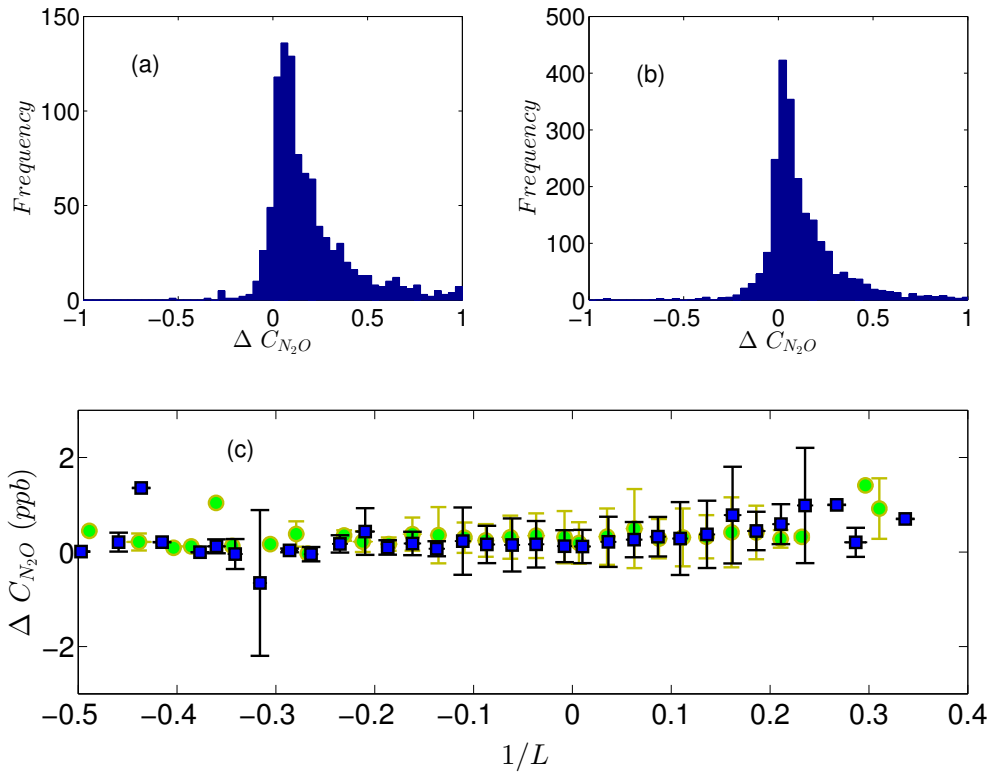

Figure 3.15: Histograms of the nitrous oxide concentration differences (ΔC_{N_2O}, ppb) are shown for the (a) autumn and (b) spring experiments. Variance of ΔC_{N_2O} is shown in (c) as a function of $1/L$ (m^{-1}) for both autumn (blue squares) and spring (green circles). The vertical and horizontal bars in (c) are the standard deviations.

Computation of the random error in the concentration difference was carried out by using a minimum resolvable difference of N_2O ($\Delta C^{min}_{N_2O}$). First, the standard error in concentration difference ($E\Delta C_{N_2O}$) was estimated by using a standard error estimation formula, given below, similar to the one mentioned in Pattey et al. (2006b) (Eqn. 12a pp 383).

$$E\Delta C_{N_2O} = \sqrt{\frac{{\sigma_{z_1}}^2}{n_{z_1}} + \frac{{\sigma_{z_2}}^2}{n_{z_2}}} \tag{3.22}$$

where z_1 and z_2 are two measurement heights and n_{z_1} and n_{z_2} are the number of random samples taken over the sampling period for z_1 and z_2, respectively. σ_{z_1} and σ_{z_2} are the standard deviations of the measured concentrations at z_1 and z_2, respectively. From the peak of the histogram of $E\Delta C_{N_2O}$ the most likely value was found to be 0.025 ppb. This value was then multiplied by the critical 2-tailed Student's-t value at a significance level of 5% to obtain a 95% confidence interval for the concentration difference resolution, and the minimum resolvable difference ($\Delta C^{min}_{N_2O}$) was found to

be 0.049 ppb. Again, a much more detailed description can be found in McMillan et al. (2012) and McMillan et al. (2013). Finally, the relative error in ΔC_{N_2O} ($R_{\Delta C_{N_2O}}$) is defined as $R_{\Delta C_{N_2O}} = \Delta C^{min}_{N_2O}/\overline{\Delta C_{N_2O}}$, where $\overline{\Delta C_{N_2O}}$ is the mean value of ΔC_{N_2O} for $1/L < 0$ and $1/L \geq 0$ periods. For $1/L < 0$, $R_{\Delta C_{N_2O}}$ was found to be 0.06 irrespective of time. Similarly, for $1/L \geq 0$, $R_{\Delta C_{N_2O}}$ was found to be 0.08. As expected, the relative error in the concentration difference was found to be higher in the stable atmosphere than the unstable one.

Total Relative error in the flux values: Finally, the total relative error in the flux value was estimated for the parameterization (R^p) and thermal (R^t) methods using the relationships $R^p = (R^2_{\Delta C_{N_2O}} + R^2_{d^p_h})^{0.5}$ and $R^t = (R^2_{\Delta C_{N_2O}} + R^2_{k^t_h})^{0.5}$. $R_{d^p_h}$ and $R_{k^t_h}$ are the simpler representations of the terms $\delta d^p_h/d^p_h$ and $\delta k^t_h/k^t_h$, respectively. Estimates of $R_{d^p_h}$ = 0.07 and 0.09 from the Monte-Carlo simulations were used with $R_{\Delta C_{N_2O}}$ = 0.06 and 0.08, respectively, for unstable and stable cases. The mean R^p for $1/L < 0$ was found to be 0.09, and for $1/L \geq 0$ was found to be 0.12. Since the mean $R_{k^t_h}$ was estimated irrespective of stability, R^t was found to be 0.62. As explained earlier, this high value of R^t can be reduced by neglecting $\overline{w'T'} < 0.001$ values and $\Delta T < 0.01$ values as 79.7% cases were observed where $\overline{w'T'} > 0.001$ and $\Delta T > 0.01$. The $R_{k^t_h}$ was found to be 0.15 for such cases. Therefore, mean R^t for this case was found to be 0.165, which is comparable to the R^p values.

3.6 Summary and conclusion

A top-down micrometeorological setup was used to measure N_2O fluxes from an agricultural paddock in Canterbury, New Zealand, in autumn and spring periods of 2010. Fluxes were estimated using a parameterization and a thermal method of the flux gradient (FG) technique, where these methods are two different approaches used to estimate the transfer coefficient. These transfer coefficients were further used to estimate the final flux values.

It was found that irrespective of the two different methods of transfer coefficient estimation from two sensors, the mean flux for the selected values varied between 7 - 26 $gN_2O\text{-}N.ha^{-1}.day^{-1}$ for both autumn and spring (Table 3.2 and 3.3). Flux values estimated by the thermal method were found to be always higher than the parameterization technique. The differences in the flux values obtained by these two methods were found to be very high, $\approx$ 5-18.0 $gN_2O\text{-}N.ha^{-1}.day^{-1}$ during very stable and very

unstable atmospheric conditions. When flux values were compared as a function of $u_\star$, fluxes from thermal transfer coefficients were found to be higher during $u_\star \leq 0.5$ m s^{-1}, whereas fluxes from the parameterized transfer coefficients were found to be higher than the thermal method only when $u_\star > 0.6$ m s^{-1}. However, only statistically significant differences in the flux values were observed for the low wind speed conditions ($u_\star < 0.2$ m s^{-1}) where p-value < 0.01. Overall, the measured flux values from the control plots compared well with the daily mean and maximum measured fluxes of already published values of Saggar et al. (2004); Di and Cameron (2003); Di et al. (2007) and Luo et al. (2008a).

When a random error sensitivity analysis was performed based on some derived numerical relationship of the FG-EC system, the following results were obtained:

- When relative error in the thermal transfer coefficient was analyzed for a single set of initial uncertainties in ΔT and $\overline{w'T'}$, relative error in the thermal transfer coefficient was found to vary between 5-9% for the Gill and CSAT3 anemometers. However, from a Monte-Carlo type analysis, it was found that for some specific initial uncertainties in the functional variables of the transfer coefficients, maximum uncertainties in the thermal transfer coefficients can vary up to 80%, irrespective of stability. It was also observed that for an ensemble of initial errors, the average uncertainty in the thermal transfer coefficients can be of the order of 15% when only $|\Delta T| > 0.01$ and $|\overline{w'T'}| > 0.001$ cases were considered.

- When the uncertainty in the parameterized transfer coefficients was compared, the maximum error was found to be as high as 49% and 35% for stable and unstable atmosphere, whereas an ensemble mean value of 9% and 7% error was observed, respectively for stable and unstable cases. The relative error in $u_\star$ was found to contribute more to the total relative error of the parameterized transfer coefficients than L, irrespective of stability.

- Unimodalities were observed in the relative error distribution of the thermal and parameterized transfer coefficients of the unstable case, whereas a partial bimodality was observed in the error distribution of the stable parameterized transfer coefficients.

- The relative error estimate in the N_2O concentration was made based on a minimum resolvable difference in concentration measurements and was found to be 0.08 and 0.06 for stable and unstable atmospheres, respectively.

- Finally, the total mean relative error in the flux values was found to be of the order of 9% and 12% for unstable and stable atmospheres using transfer coefficients from the parameterization method and 16.5% for transfer coefficients of the thermal method.

Micrometeorological flux estimation of N_2O is an alternative approach to chamber measurements with some clear advantages, but this method depends strongly on the determination of atmospheric stability and turbulent eddy properties. Therefore, rigorous data processing is necessary to estimate actual flux values. Again, cross-validation of the flux values with chamber measurements can improve the reliability of the micrometeorological method. Furthermore, since this study does not include the errors associated with footprint heterogeneity and systematic errors, further inclusion of errors from these two sources can change the final mean error estimate of the flux values.

Chapter 4

Estimation of source area emission rates using footprint methodologies

4.1 Introduction

Measurement of biogenic trace gases has gained considerable interest in the last few decades as the climate of this planet is found to be strongly affected by the abundance of these constituents in the atmosphere (Denman et al., 2007). Therefore, many experiments have been carried out to estimate the source strength of different trace gases from different ecosystems. With the improvements of measurement methods and instrumentation, micrometeorological measurement techniques, such as the eddy covariance (EC) and flux gradient (FG) system, have been widely used for such trace gas flux measurements all around the world. A combined FG and EC measurement system, where turbulent eddy diffusivity is estimated from the EC method and fitted to the FG equation, is also becoming an alternative technique of trace gas flux measurement (Phillips et al., 2007; Neftel et al., 2007; Harvey et al., 2008b). One of the important advantages of this FG-EC system over the standard static chamber flux measurement is that this system is able to measure spatially integrated flux values over long time periods continuously and, can have an upwind fetch a hundred times more than the measurement height (Horst and Weil, 1994; Horst, 1999). Such an integrated flux measurement is able to capture the spatial heterogeneity of surface emission rate which can not be covered by small number of chambers. However, a particular challenge exists when micrometeorological techniques are used in a comparative mode. The unconstrained nature of the spatial domain contributing to the fluxes requires a method to explicitly determine the area contributing to the fluxes measured at the loca-

tion of the sensors. The method will allow a reliable attribution of measured fluxes to treatment plots. Therefore, a 'footprint analysis' is carried out for the purpose of source area identification and emission rate estimation by representing the measured flux as a product of source area emission rate and a footprint function (f_p) (Gash, 1986). The f_p should have a crosswind and a streamwise component and is broadly expressed as a function of atmospheric surface layer parameters. Several different footprint functions have been developed in the last two decades (Schmid, 1994; Horst and Weil, 1994; Kormann and Meixner, 2001; Sogachev and Lloyd, 2004; Kljun et al., 2004) and the choice of any of these approaches for source area estimation depends mostly on the spatio-temporal scale of the measured flux and on the wider objectives of the study.

A comprehensive 'footprint analysis method' is a key objective for a flux measurement study because the footprint analysis alone can only provide information about source area emission and fetch-to-height ratios. This information should be used in a systematic manner so that the emission rate of a specific field can be estimated. Such a 'footprint analysis method' becomes necessary if the emission source area shape varies along with plot treatment heterogeneity, and continuous flux measurement is made. A comprehensive footprint analysis method would provide an estimate of the measured flux contaminated by the flux values originating outside the predefined source area. Furthermore, total relative error accumulation in the final flux value due to footprint heterogeneity can also be estimated.

Here, a numerical method is developed to estimate source area emission using the footprint model of Kormann and Meixner (2001) that was implemented in a VBA by Neftel et al. (2008), for a setup where fluxes are measured continuously from some control and experimental plots of similar shape and size. The control plots are defined as untreated plots having unmitigated emission of N_2O, whereas, the experimental plots are chemically treated to mitigate N_2O emission. An inverse footprint fraction approach is proposed in this study to estimate the source area emission rate where the footprint fractions are obtained from the Kormann and Meixner (2001) model. An analytical solution is also provided for the unknown background flux. A validation of the footprint fractions obtained from the analytical model is carried out using footprint fractions obtained from a forward simulation of the backward Lagrangian stochastic model (bLs) of Flesch et al. (1995). Furthermore, emission rates obtained from the proposed setup are compared with emission rates obtained from a 'backward' simulation of the same bLs model to ascertain the realistic nature of the proposed inverse footprint method.

Section 4.2 of this chapter describes the measurement setup of the field campaign, including the location and orientation of subplots and instrumentation. Section 4.3.1 describes the numerical approach to source area emission rate estimation. Brief descriptions of the analytical and bLs footprint models are provided in Sections 4.3.2 and 4.3.3. The primary footprint analysis results are presented in Section 4.4.1, while the source area emission rates are provided in Section 4.4.1.1. The bLs model results are presented in Section 4.4.2 and a conclusion is provided in Section 4.5.

4.2 Experimental setup and measurements

Although a detailed description of measurement setup and instrumentation is provided in Chapter 3, a brief description is given here. Figure 4.1 shows the location of subplots and instrument towers in a Cartesian coordinate system. The experimental paddock was aligned approximately 340° to true north. The field coordinates are defined based on the location of a 3-D Gill anemometer (Wind Master Pro, Lymington, UK), shown as EC-2 in Figure 4.1. It is assumed that the Gill is situated at coordinate (0, 0). The other sonic anemometer, EC-1 in Figure 4.1, is the 3-D CSAT3 anemometer (Campbell Scientific Inc., UT, USA). The flux gradient (FG) gas inlets are shown as G-1 to G-4 in the diagram. Air samples were collected at each of these masts using a lower gas inlet at 0.5 m and a higher gas inlet at 1.0 m. A tunable diode laser was used to measure the N_2O concentrations and their differences (ΔC_{N_2O}). The measurement field was divided into three control subplots (A, C and E of Figure 4.1) and two experimental subplots (B and D of Figure 4.1) with an approximate width of 140 m and length of 100 m each.

Fluxes were measured in a switching cycle such that for one averaging period (30 min in autumn, 20 min in spring) air was sampled only from one mast, alternating rapidly (every 9 sec in autumn and 6 sec in spring) between the two intake heights. For the subsequent averaging periods, air from each of the masts was sampled. The shorter integrating time was used in the spring experiment to obtain a greater number of samples of the N_2O flux.

As mentioned in Chapter 3, during the filtering procedure only those data were retained where (i) -0.5$\leq 1/L \leq$0.5, where L is the Obukhov length, (ii) $u_\star > 0.075$ m s^{-1}, where $u_\star$ is the friction velocity, and (iii) $u_\star/U_{mean} < 0.2$, where U_{mean} is the mean wind speed at the measurement height. Therefore, extremely stable and unstable cases were neglected. In this chapter, only turbulent eddy diffusivity estimated using the

parameterized approach (Equations 3.4 and 3.5 of Chapter 3) was considered and along with ΔC_{N_2O}, fluxes were estimated at each measurement mast following Equation D.1 of Appendix D and the procedure described in Section 3.5.5 of Chapter 3. The sonic anemometer measurements used for eddy diffusivity estimation were used in the following section to estimate footprint fractions from the analytical model.

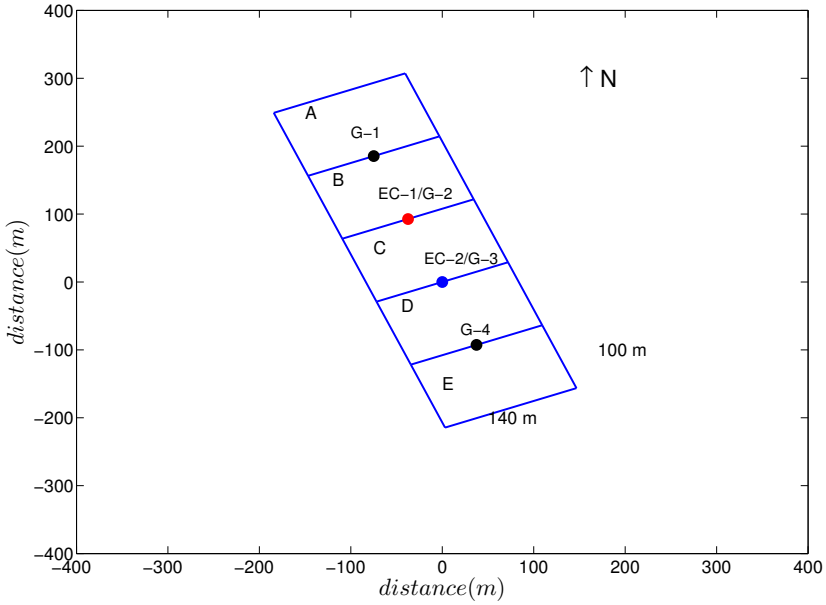

Figure 4.1: Layout of the measurement field showing subplots A-E. EC-1 is the location of the CSAT3 anemometer, EC-2 is the location of the Gill anemometer, G-1 to G-4 are the FG gas intake positions.

4.3 Methods and footprint models

The numerical approach to source area emission rate estimation for the above mentioned field setup is described in Section 4.3.1 and it largely depends on the 'footprint fraction' of each field, where footprint fraction denotes the percentage contribution of each field to the total measured flux at each mast as obtained from a standard footprint model. Here, the footprint fractions were obtained from the Visual Basic Application based footprint model of Kormann and Meixner (2001), as developed by Neftel et al. (2008) and described in Section 4.3.2. A backward Lagrangian stochastic model (bLs) was also used for comparison purposes, and is described in Section 4.3.3. It should be noted that the numerical setup of emission rate estimation described in this study is generic and can be applied to any such measurement setup that includes the problem of uncertain land type representation in the measured flux from a heterogeneous field.

4.3.1 Numerical setup for estimating source area emission rate

The goal is to compute the emission rates from the rectangular plots A to E, which are roughly aligned from north to south. We can denote the emission rates by ER^A, ..., ER^E. Vertical fluxes were measured at four masts on the boundaries between these plots and denoted by F^1, ..., F^4. Now if only the northerly wind bisector is considered, fluxes (F^1, ..., F^4) will not only depend on the corresponding emission rates from rectangles A to D, but will also depend on the emission rate north of subplot A, denoted as ER^N. We assume ER^N to be spatially uniform with infinite extent in the upwind direction. Given this definition of ER^N, it must be equal to the flux F^0 that would have been measured at the upwind boundary of subplot A, had there been a measurement mast. We can then write the emission rates and the fluxes as a 5-component vector. These vectors are related by a 5×5 matrix, the footprint fraction matrix, with elements γ^{ij} obtained from any analytical footprint model as:

$$\begin{pmatrix} F^0 \\ F^1 \\ F^2 \\ F^3 \\ F^4 \end{pmatrix} = \begin{pmatrix} \gamma^{0N} & \gamma^{0A} & \gamma^{0B} & \gamma^{0C} & \gamma^{0D} \\ \gamma^{1N} & \gamma^{1A} & \gamma^{1B} & \gamma^{1C} & \gamma^{1D} \\ \gamma^{2N} & \gamma^{2A} & \gamma^{2B} & \gamma^{2C} & \gamma^{2D} \\ \gamma^{3N} & \gamma^{3A} & \gamma^{3B} & \gamma^{3C} & \gamma^{3D} \\ \gamma^{4N} & \gamma^{4A} & \gamma^{4B} & \gamma^{4C} & \gamma^{4D} \end{pmatrix} \begin{pmatrix} ER^N \\ ER^A \\ ER^B \\ ER^C \\ ER^D \end{pmatrix} \tag{4.1}$$

or in a more compact notation

$$F^i = \sum_j \gamma^{ij} ER^j \tag{4.2}$$

Now in Equation 4.1, symbols γ^{1N} to γ^{4N} can be calculated as the outside flux contribution at each mast and γ^{0A} to γ^{0D} are equal to 0. A similar set of equations can be derived for a southerly wind bisector and the emission rate of subplot E (ER^E) can be estimated. However, the footprint analysis procedure is restricted to subplots A to D as subplot E is a terminal control plot and would have similar effects to subplot A. It is to be noted that $0 \leq \gamma^{ij} \leq 1$ for each row of the matrix and the elements must add up to 1. It is further to be noted that the diagonal elements will usually be the largest elements of a given row reflecting the dominant influence of the nearest plot on a flux measurement. For a northerly wind which is oriented relative to the field, the elements to the right of the diagonal will be 0, because the plots downwind of a mast have no influence on their flux observations. Furthermore, for a 340^0 wind, aligned with the field orientations, conditions (i) $\gamma^{2A} = \gamma^{3B} = \gamma^{4C} > 0$, (ii) $\gamma^{3B} >$

$\gamma^{3A} > 0$ and (iii) $\gamma^{4C} > \gamma^{4B} > \gamma^{4A} > 0$ are satisfied. However, if the minor axis of the footprint ellipse is considerably smaller than the major axis, which can happen depending on atmospheric stability and wind speed, and if the wind direction deviates considerably from the northerly field alignment and remains unchanged, the γ^{ij} matrix will be such that, $\gamma^{1A} = \gamma^{2B} = \gamma^{3C} = \gamma^{4D}$, $\gamma^{1N} = \gamma^{2N} = \gamma^{3N} = \gamma^{4N} = [1 - \gamma^{1A}(= \gamma^{2B} = \gamma^{3C} = \gamma^{4D})]$ and all the other elements of γ^{ij} will be 0. Such a case is not completely practical but can have theoretical implications, and the emission rate estimation procedure described here cannot be applied.

It is already mentioned that Equation 4.1 collapses to $F^0 = ER^N$, so the emission rates can be estimated following:

$$ER^j = \sum_i \eta^{ji} F^i \tag{4.3}$$

where, $\eta^{ji} = (\gamma^{ij})^{-1}$ and Equation 4.3 can be expressed as:

$$\begin{pmatrix} ER^N \\ ER^A \\ ER^B \\ ER^C \\ ER^D \end{pmatrix} = \begin{pmatrix} \eta^{N0} & \eta^{N1} & \eta^{N2} & \eta^{N3} & \eta^{N4} \\ \eta^{A0} & \eta^{A1} & \eta^{A2} & \eta^{A3} & \eta^{A4} \\ \eta^{B0} & \eta^{B1} & \eta^{B2} & \eta^{B3} & \eta^{B4} \\ \eta^{C0} & \eta^{C1} & \eta^{C2} & \eta^{C3} & \eta^{C4} \\ \eta^{D0} & \eta^{D1} & \eta^{D2} & \eta^{D3} & \eta^{D4} \end{pmatrix} \begin{pmatrix} F^0 \\ F^1 \\ F^2 \\ F^3 \\ F^4 \end{pmatrix} \tag{4.4}$$

The condition $\eta^{ji} \subset \Re$, where $\Re$ is a real number series, will only be satisfied if the diagonal elements of $\gamma^{ij} \neq 0$, although cases were observed where diagonal elements of γ^{ij} were missing for both autumn and spring experiment. Such cases where 3 or more diagonal elements of γ^{ij} were missing were completely ignored, although for cases where 2 or more diagonal elements of γ^{ij} were missing, a maximum possible weight of 0.97 was provided.

Since we know only four of the five flux vector elements of Equation 4.4, we need a reasonable assumption to solve Equation 4.4 as the problem is under determined. If it is assumed that $ER^A = ER^C$, because both of them were control plots with no treatment, ER^A and ER^C can be expressed for a purely northerly wind as:

$$ER^A = F^0\eta^{A0} + F^1\eta^{A1} \tag{4.5}$$

and,

$$ER^C = F^0\eta^{C0} + F^1\eta^{C1} + F^2\eta^{C2} + F^3\eta^{C3} \tag{4.6}$$

Equations 4.5 and 4.6 are derived for a northerly wind aligned with the field orientation so that wind direction ranges approximately equally aligned with the field. Hence, only the contributions from the immediately adjacent fields are included, although during a marginal variation in wind direction from purely northerly, Equations 4.5 and 4.6 should be changed to:

$$ER^A = F^0\eta^{A0} + F^1\eta^{A1} + F^2\eta^{A2} \tag{4.7}$$

and

$$ER^C = F^0\eta^{C0} + F^1\eta^{C1} + F^2\eta^{C2} + F^3\eta^{C3} + F^4\eta^{C4} \tag{4.8}$$

Equations 4.7 and 4.8 can be used to estimate the emission rates from subplots A and C if instantaneous flux values are available for $F^1, .., F^4$ and the F^0 values are known. Since at an instant time all the four fluxes ($F^1, .., F^4$) were not available from the measurement, synchronized time series of flux values were prepared for each mast using a linear temporal interpolation.

In the case of estimating unknown F^0, two possible approaches can be followed. One, an algebraic relationship can be obtained for F^0 by combining Equations 4.7 and 4.8 as,

$$F^0 = \frac{\eta^{C1} - \eta^{A1}}{\eta^{A0} - \eta^{C0}}F^1 + \frac{\eta^{C2} - \eta^{A2}}{\eta^{A0} - \eta^{C0}}F^2 + \frac{\eta^{C3}}{\eta^{A0} - \eta^{C0}}F^3 + \frac{\eta^{C4}}{\eta^{A0} - \eta^{C0}}F^4 \tag{4.9}$$

In theory, the solution of Equation 4.9 is unique and exact. In practice, we have to be very cautious because of the numerical uncertainty of the measured fluxes, and also because some elements of the η^{ji} matrix are not very different from 0. These are the two components of Equation 4.9 which can make the numerical solution of F^0 unstable. Inserting realistic example values one can see that F^0 is obtained as a small difference of the two almost equally strongly weighted flux terms F^1 and F^3 with a minor correction from F^2 and F^4, with much lower weights. Therefore, any measurement error or discontinuity in the difference of F^1 and F^3 will cause a huge error in F^0.

The numerical constrains for this method including the solution of Equation 4.9 has been already described above. For further application of F^0 to compute ER^A and ER^C, only those cases should be used to compute F^0 where the flux footprint is relatively large and therefore the non-diagonal elements of the γ-matrix are substantial

and $|F^1 - F^3|$ is minimal. Again, one has to note that the each F^0 values computed following this approach cannot be directly fed back to Equation 4.7 and 4.8 for individual emission rate estimation as algebraic equality between ER^A and ER^C has been assumed. Therefore, a statistically significant and physically meaningful value of F^0 obtained from Equation 4.9 should be used. The procedure for F^0 estimation has been described below and emission rates estimated using that F^0 value are represented by $ER_{F^0_{eqn}}$.

Now, if the assumption of equality of emission rates from control plots holds true throughout the experimental period, irrespective of time, then F^0 computed by the above method can be used to compute emission rates from the mitigated plots (e.g. plots B and D). Therefore, emission rate equations can be derived for subplots B and D similar to Equation 4.7 and 4.8. Hence, this approach can be applied to any other measurement setup where equality of the emission rates can be assumed for heterogeneous plots when deriving the unknown background flux.

4.3.2 Analytical flux footprint model

The analytical flux footprint model of Kormann and Meixner (2001) is a suitable model for scalar flux footprint estimation from an eddy covariance (EC) measurement system. The model uses the solution of an advection diffusion equation for a power law profile of mean wind velocity and diffusivity. The two-dimensional footprint function for a fixed measurement height obtained from this model is expressed as (Kormann and Meixner, 2001):

$$f_p(x,y) = \frac{1}{\sqrt{2\pi}Dx^E} exp\left(-\frac{y^2}{2Dx^E}\right) Cx^{-A} exp\left(-\frac{B}{x}\right) \tag{4.10}$$

Where the *A*, *B*, *C*, *D* and *E* terms are discussed in detail in Kormann and Meixner (2001) and Neftel et al. (2008). A Visual Basic Application based program of this model was developed by Neftel et al. (2008) which also included coordinates of the measurement field and instrument locations. The model approximates the footprint ellipse and footprint fraction of individual fields based on the EC measurements of $u_\star$, wind direction, *L*, standard deviation of the lateral wind component (σ_v), and horizontal wind speed (assumed to be equal to U_{mean}).

This analytical footprint model was used as the base model for our footprint analysis. The measurement height (z_m) was assumed to be the geometric mean height of the gas inlets, equal to 0.86 m above a displacement height d = 0.066 m (Details are given

in chapter 3). The emission rates were estimated based on the footprint information of this analytical model and compared with the backward Lagrangian stochastic model output.

4.3.3 Backward Lagrangian model

The bLs model used for this study was *WindTrax* version 2.0.8.4. This model is based on Flesch et al. (1995) and widely used for paddock scale flux footprint estimation (Laubach and Kelliher, 2005; Flesch et al., 2005; Bjorneberg et al., 2009; Laubach, 2010). Although a detailed description of the model can be found in Flesch et al. (1995, 2004, 2005), a brief description is provided below. The particular model setup for our field experiment is described in Section 4.4.2.

The basic model setup is divided into three major components: (i) the 'atmosphere' where the background concentration (C_b) of the measured chemical compound is provided along with the temperature, pressure and the surface elevation, (ii) the 'surface layer model' where atmospheric variables such as $u_\star$, L, roughness length (z_0), and wind statistics are provided, and (iii) the 'bLs model' which simulates particle backward trajectories. An extra component called the 'algebra engine' provides a summary and possible solution of the model setup. The gas source area with an unknown emission rate (Q) can be described inside the model. Now, the bLs model assumes an homogeneous surface source for Q, and if the measured concentration of the chemical compound at a certain location inside the source area is C_i then $\Delta C/Q$ is expressed using measurable quantities and bLs simulates backward flight paths of air parcels from the measurement height of C_i. The ΔC is expressed as C_b - C_i. To describe the varying velocities of air parcels, the *Langevin model* is used, where the velocity gradient is expressed as: $\Delta u_k = \alpha_k \Delta t + \beta_k P_k$. Here k is the number of air parcels and α and β are numerical coefficients and P is a Gaussian random number. For each time step, the position of the air parcel is described as: $\Delta x_k = u_k \Delta t$. The model is then integrated backward for as many as 50000 air parcels. During the backward integrations, some of the air parcels will touch the ground surface and will be reflected back to air, this process is called *touchdown*. Every touchdown within the source area will change the sign of the vertical velocity w_0 and contribute to the flux estimation. Thus, the bLs model finds the surface flux rate for n number of air parcels within the source area using the formula: $\Delta C/Q_{bLs} = (1/n)\sum 2/|w_0|$. The model assumes flat terrain with uniform surface roughness length and uses flux variance similarity for estimation of

the coefficient β which is a function of $C_0\epsilon$, where ϵ is the dissipation rate of turbulent kinetic energy and C_0 is a function of $\sigma_w/u_\star$ (Wilson et al., 2001). C_0 is also equivalent to the turbulent Schmidt number (Sc) and an empirical value of Sc is used in this model. A detailed description can be found in Laubach and Kelliher (2005).

4.4 Results and discussion

As already shown in Section 4.3.1 the emission rate estimation method depends on the footprint fraction values of individual subplots, so a proper footprint analysis will be carried out first, as described in Section 4.4.1. Next, this footprint information will be used in Section 4.4.1.1 for emission rate estimation from control plots. A total relative error estimate will be provided in Section 4.4.1.2 and comparison with the bLs model will be made in Sections 4.4.2 and 4.4.3.

4.4.1 Footprint from analytical models

The footprint analysis of each measurement mast was carried out based on the predominant surface wind regimes of both field campaigns. A detailed description of the surface wind regime has been provided in Section 3.5.3 of Chapter 3, along with seasonal wind roses (Figure 3.6). However, a concise review is presented here. The dominant wind regimes were found to be north-northeasterly (N-NE), north-northwesterly (N-NW) and southwesterly (S-W) for both autumn and spring experiments. During the autumn experiment, three predominant wind regimes were observed: 0-50^0 (N-NE) with 18.1% of the total data and an average wind speed of 2.60 m s^{-1}; 300-360^0 (N-NW) with 33.9% of the total data and an average wind speed of 1.94 m s^{-1}; and 200-260^0 (S-W) with 22.0% of the total data and an average wind speed of 2.63 m s^{-1}.

During the spring experimental period, an increase in the N-NE wind ranges was observed. The dominant wind direction for this period was N-NE (0-100^0) with 45.3% of the total observation and an average wind speed of 2.11 m s^{-1}. N-NW winds (300-360^0) constituted 24.1% of the total observations with an average wind speed of 3.12 m s^{-1}, and S-W winds (200-260^0) with only 9.3% of the total observation and an average wind speed of 2.69 m s^{-1}.

The time averaged values of $u_\star$, wind direction, L, σ_v, and U_{mean} were fed into the analytical footprint model along with the field coordinates and z_m. The model output constituted of: (i) z_0, (ii) footprint function (f_p), (iii) footprint fraction from

each subplot (γ), which is a fraction of the total integral of footprint function for a particular domain and estimated based on the predefined coordinates of the domain, and (iv) values of the constants *A*-*E* and distances for calculating the semi-major and semi-minor axes of the footprint area, which is assumed to be an ellipse. The ellipses mark the boundary of the emitting surface area, where the footprint function drops to 1% of its maximum value. It should also be noted that the footprint function is asymmetric in nature and therefore, source areas nearer to the measurement mast will have a higher contribution to the measured flux (Neftel et al., 2008). The peak location of the footprint function, f_p^{max}, was estimated by calculating the distance (*R*) from the measurement tower to the centre of the ellipse using output of the code provided by Neftel et al. (2008) (see the manual for the code at http://www.agroscope.admin.ch/art-footprint-tool/). Finally, the Cartesian coordinate of the centre of the ellipse (x_0,y_0) was estimated following Equation 4.11.

$$\left.\begin{aligned} x_0 &= Rcos\theta_{rad} + x_{mast} \\ y_0 &= Rsin\theta_{rad} + y_{mast} \end{aligned}\right\} \tag{4.11}$$

Where θ_{rad} is the wind direction in radians, x_{mast} and y_{mast} are the x and y coordinates of the mast. Although it is numerically simpler to assume the footprint area as approximately equal to an ellipse, in reality the footprint source area resembles an ellipsoid and the shape can change with stability and wind speed. Therefore, the f_p^{max} values computed from the above method may not necessarily be the actual representation of f_p^{max}, but a close approximation.

Footprint for the EC-1/G-2 mast Coordinates of the f_p^{max} under N-NE winds are shown in Figure 4.2(a) (left panel) for autumn and 4.2(a) (right panel) for spring. Each f_p^{max} coordinate in the diagram is, therefore, a function of instantaneous wind direction. Similarly, Figure 4.2(b) upper panel and 4.2(b) lower panel show the maximum footprint fractions (γ) for the same wind regimes and for the autumn and spring campaigns. The principal source areas (PSA) of the measured fluxes, where γ is maximum, along with the mean values of the peak distances of footprint functions, $\overline{f_p^{max}} = 1/N \sum_N^1 f_p^{max}$, at EC-1/G-2 for all the three subplots are shown in Table 4.1 for both seasons. The height-to-fetch ratios for all the stability classes were found to be within 1:100. From the f_p^{max} and $\overline{f_p^{max}}$ values it was evident that, predominantly, most of the fluxes measured at the EC-1/G-2 location were coming from within the boundaries of the subplots. The atmospheric stability conditions were mostly neutral,

40.2% and 56.9% of the time for N-NE, and 59.4% and 46.3% for N-NW, respectively, for the autumn and spring experiments. Similar results were obtained for the EC-2/G-3 mast, where the principal source area contributing the measured flux was found to be subplot C for N-NE and N-NW wind regimes and subplot D for the S-W wind regime, respectively.

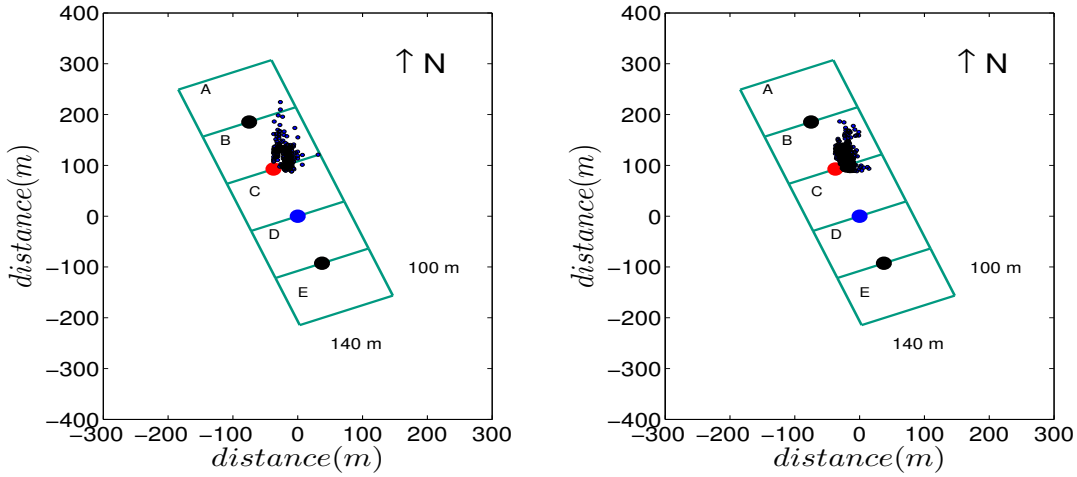

(a)

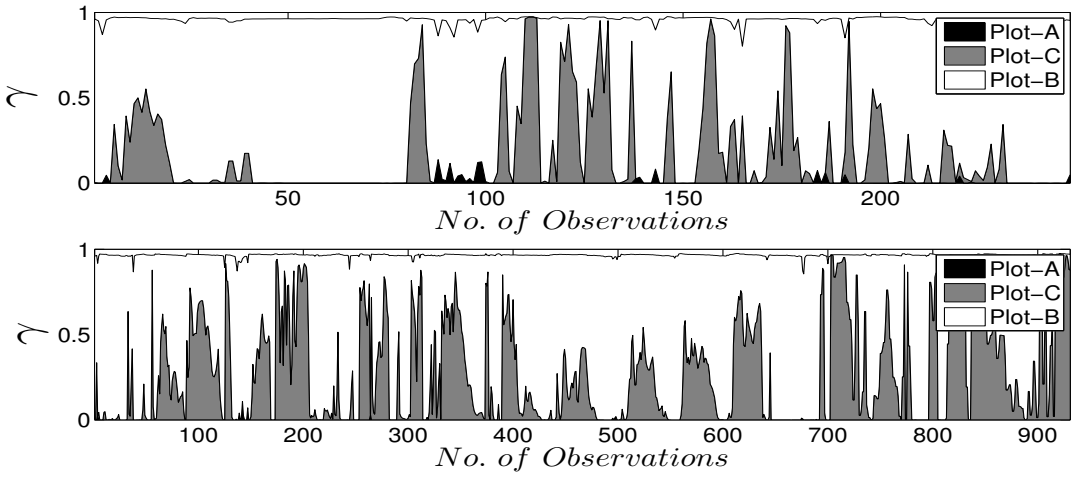

(b)

Figure 4.2: (a) The locations of 30/20 minute f_p^{max} from the EC-1/G2 measurement mast for only the N-NE wind directions (left panel for autumn and right panel for spring), (b) The γ values for subplots for only the N-NE wind regime at the EC-1/G-2 mast. Upper panel is for autumn and lower panel is for the spring campaign.

Footprint for the G-1/G-4 mast: It has already been mentioned that our sonic anemometers were placed at the locations EC-1 and EC-2, and no sonic anemometer measurements were available for the G-1 and G-4 locations, but to get an idea of the source

Table 4.1: Percentage contributions of the principal source areas (PSA) to fluxes measured at the EC-1/G-2 location are shown for different wind regimes. Mean values of peak distance of the footprint function, $\overline{f_p^{max}}$, are also shown.

Wind regime	Source area information for EC-1			
	autumn		spring	
	PSA(%)	$\overline{f_p^{max}}$ (m)	PSA(%)	$\overline{f_p^{max}}$ (m)
N-NE	subplot B (79.6%)	38.7	subplot B (68.0%)	29.7
N-NW	subplot B (90.9%)	59.4	subplot B (95.2%)	41.0
S-W	subplot C (70.4%)	44.6	subplot C (70.2%)	41.3

area contribution to the measured flux values at G-1 and G-4, the CSAT3 measurements were used at these locations. Similar to the EC-1/2 analysis, γ values from individual subplots were also estimated for G-1 and G-4 and the results were used to estimate the source area emission rate of individual subplots.

Source area outside the measurement paddock: It is evident from Figures 4.2 that $(\sum_{i=1}^{5} \gamma_i) \neq 1$, where *i* represents the number of subplots. This implies that a source area outside the predefined area of interest also contributed to the flux measurement at the individual measurement locations. Therefore, the footprint fraction outside our area of interest ($\gamma_{outside}$) was computed following $\gamma_{outside} = 1 - \sum_{i=1}^{5} \gamma_i$. Variations in the $\gamma_{outside}$ values as a function of wind direction and surface layer stability are shown in Figure 4.3. Both EC-1 and EC-2 data were used to produce this diagram. The maximum contribution of source area outside all of our experimental subplots was found to be of the order of 30%, irrespective of the measurement masts and plots (Figure 4.3.b).

One can see from Figure 4.3 that except for some occasional high values of $\gamma_{outside}$, contributions from outside the source area remained minimal. The mean $\gamma_{outside}$ value, irrespective of measurement mast and experimental campaign, was found to be 0.043(4.3%), which is significantly lower than the contribution from the principal source areas. High values of $\gamma_{outside}$ were mostly found to be associated with higher atmospheric surface layer stability ($1/L > 0.1$). Again, when the effect of geometry of the plot relative to $\gamma_{outside}$ was considered for a stable atmosphere, most of the high values were observed when the wind was diagonal to the field, and particularity high $\gamma_{outside}$ values were observed when the wind direction was between 225-255^0.

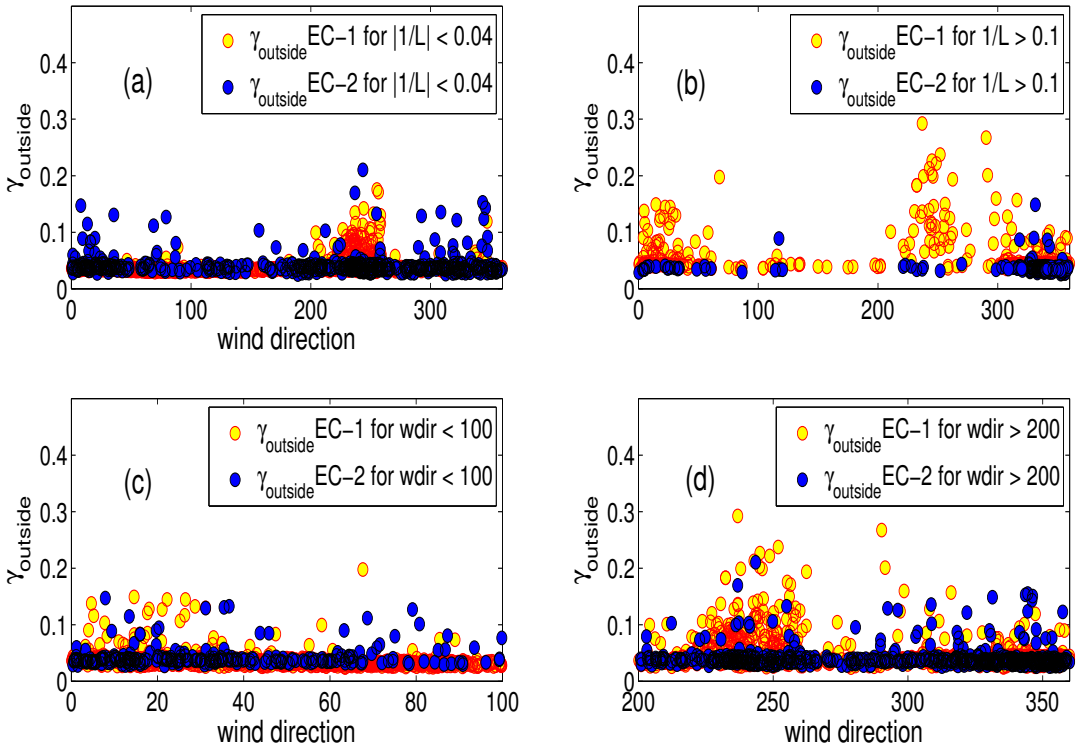

Figure 4.3: The $\gamma_{outside}$ values of both autumn and spring are plotted for (a) a neutral atmosphere ($|1/L| < 0.04$) and (b) a stable atmosphere ($1/L > 0.1$) using measurements at masts EC-1 and EC-2. Similarly, $\gamma_{outside}$ values of both autumn and spring are plotted for (c) N-NE and (d) N-NW and S-W wind regimes irrespective of stability and using measurements at masts EC-1 and EC-2.

4.4.1.1 Measured fluxes and emission rates from control plots

Flux values were measured at individual masts, where each mast was located at the interface of two subplots. Now, these measured flux values from each mast can be assigned to each plot depending on northerly or southerly wind bisectors if no footprint correction is assumed. For example, the flux measured at the G-1 mast location in Figure 4.1 can be assigned to plot A for a northerly wind bisector and plot B for a southerly wind, respectively. Such assignment of measured flux to a specific subplot based on wind directions is a good approximation of actual emission rate if the footprint ellipse covers the described source area. Such values are termed as 'measured flux (Flux_p)' in this section and computed for each subplot. Measured flux values as well as standard errors (SE) in the measurements of subplot A and C for both autumn and spring experiments are shown in Table 4.2. Cases were only chosen for comparison where both measured fluxes and emission rates were available (e.g. Flux_p and $ER_{F^0_{eqn}}$). The SE values were calculated following SE = $\sigma_{var}/\sqrt{n}$, where σ_{var} was the standard deviation of var and n is the number of the data. Flux_p of Table 4.2 repre-

sents the measured flux obtained using the parameterized transfer coefficients derived following Phillips et al. (2007) (Equation 10, pp 94).

Table 4.2: Arithmetic mean ± standard error of the selected measured flux and emission rate of N_2O in $gN_2O\text{-}N.ha^{-1}.day^{-1}$ for the autumn and spring experiments are denoted by 'arithmetic'. Emission rates are estimated using F^0 from Equation 4.9 ($ER_{F^0_{eqn}}$). Observations were only used for this comparison where both measured flux and emission rate values were available. Hence, the mean $Flux_p$ values computed here can be marginally different than the values reported in Table 3.2 and 3.3. The total number of such observations is shown in parenthesis.

Seasons	**N_2O flux $gN_2O\text{-}N.ha^{-1}.day^{-1}$**		
	Plots	$Flux_p$	$ER_{F^0_{eqn}}$
Autumn	$A_{arithmetic}$	9.4 ± 1.28 (100)	9.4 ± 1.34 (100)
	$C_{arithmetic}$	14.1 ± 2.74 (98)	14.6 ± 2.84 (98)
Spring	$A_{arithmetic}$	13.1 ± 2.16 (229)	13.6 ± 2.20 (229)
	$C_{arithmetic}$	12.5 ± 1.61 (230)	12.8 ± 1.54 (230)

Surface emission rates were computed using only those fluxes which were obtained using the parameterized diffusivity coefficients derived from the CSAT3 instrument. When F^0 was estimated using Equation 4.9, some unrealistically large negative/positive values were observed ($|F^0| > 1000$ $gN_2O\text{-}N.ha^{-1}.day^{-1}$). As mentioned in Section 4.3.1, these cases were detected when differences between F^1 and F^3 were high ($|F^1 - F^3| > 5$ $gN_2O\text{-}N.ha^{-1}.day^{-1}$) and contributions from term 2 and/or 4 of the right hand side of Equation 4.9 were significant. All such high values were discarded and only those F^0s were accepted where the numerical solution of Equation 4.9 had physical meaning. Although such observations were few, a lower and upper limit of such values were found to be between $0 \leq F^0 \leq 15.0$ $gN_2O\text{-}N.ha^{-1}.day^{-1}$. However, a mean value of F^0 = 6.77 was used in Equation 4.7 and 4.8 to estimate emission rates for both seasons. The emission rate, obtained using F^0 are shown in Table 4.2. Emission rate estimates were found to be higher than the $Flux_p$ values. The maximum variation between $Flux_p$ and $ER_{F^0_{eqn}}$ estimates was 0.5 $gN_2O\text{-}N.ha^{-1}.day^{-1}$ for the control plots, irrespective of seasons, which was on average 2.1% higher than the measured flux. However, depending on the variation of F^0, $ER_{F^0_{eqn}}$ values were found to increase upto 6%. A higher actual emission rate than the measured flux is expected under an approximately fixed background flux of N_2O as the footprint fraction will seldom have the idealistic value of 1 and corresponding η value. This will signify a fractional mapping between the measured flux and emission rate. To explore the effect of stability on the ER^A and ER^C values obtained from the numerical method, that is $ER_{F^0_{eqn}}$ and $Flux_p$ are plotted as functions of $1/L$ in Figure 4.4 for both autumn (Figure 4.4.a and b) and spring campaigns (Figure 4.4.c and d). Instead of a direct comparison

of emission rates with each other, these variables are plotted against the stability parameter $(1/L)$ to explore their variations in different atmospheric conditions. Most of the fluxes and emission rates were obtained while -0.3 $\leq$ 1/L $\leq$ 0.3 and comparatively high values were observed when $1/L \geq 0$. Since the proposed method performs a flux partitioning within several multiplots, the correlation coefficients between fluxes and emission rates were always high ($>$ 0.90). Effect of the footprint corrections to the measured fluxes of plot B and D are discussed in the next chapter.

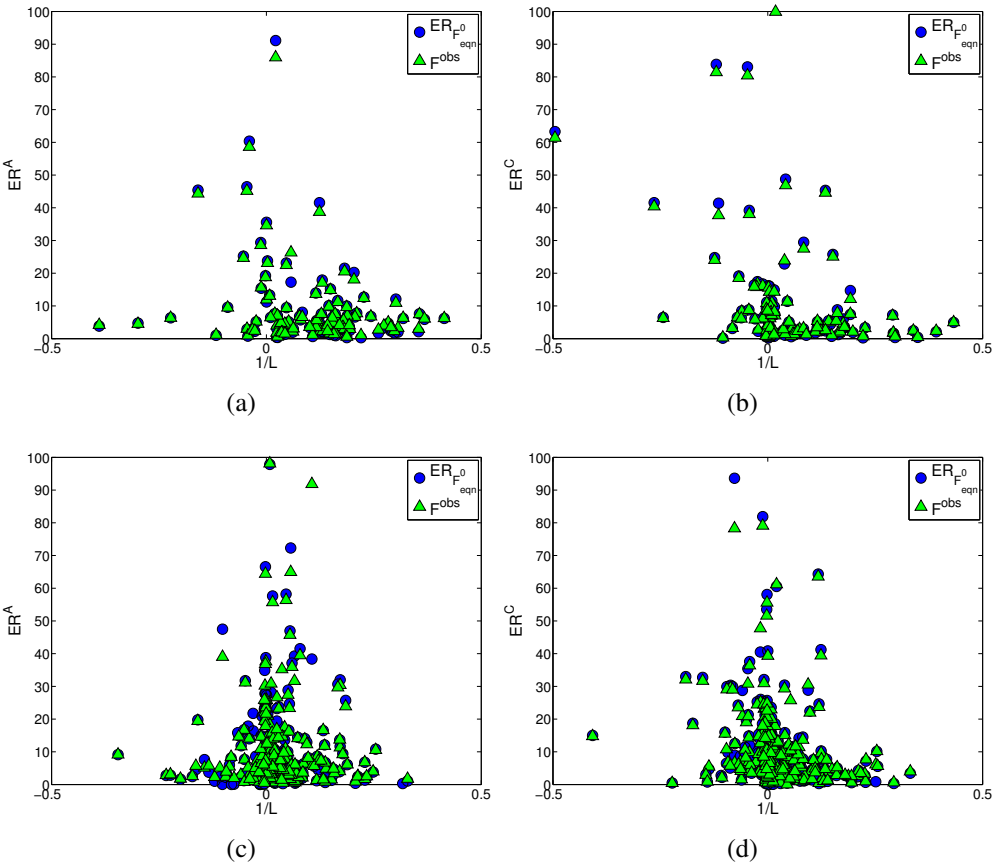

Figure 4.4: Emission rates ($ER^{A,C}$) and observed flux values (F^{obs}) in gN$_2$O-N.ha^{-1}.day^{-1} are represented as functions of inverse Obukhov lengths $(1/L)$ in m^{-1} for (a-b) autumn and (c-d) spring campaigns of subplots A and C, respectively.

4.4.1.2 Error analysis of the analytical footprint model

Uncertainty in the analytical footprint model is quantified in this section, therefore, error associated with footprint heterogeneity is assessed. Instead of deriving an algebraic equation for the relative error in the footprint function, a sensitivity analysis has been performed using the footprint tool developed by Neftel et al. (2008). The

previous study by Neftel et al. (2008) has shown that the longitudinal variation of the footprint function largely depends on the $U_{mean}/u_\star$ ratio, which reflects the strength of horizontal advection with respect to vertical diffusion. That study has also correlated the z_0 values with the $U_{mean}/u_\star$ ratios and found an approximate 25% change in the footprint values when z_0 was changed by a factor of 2, but the effect of stability was ignored as most of the analyzed cases were for a near neutral atmosphere. Comparisons of the model predicted z_0 values with observations for neutral atmospheric conditions are shown in Figures 4.5(a) and 4.5(b), respectively for autumn and spring. Instantaneous z_0 values were computed for both G-2 and G-3 masts and compared with observations. The model-simulated mean z_0 values for the southwesterly and north-northwesterly wind regimes of our experiment were found to be approximately $\pm$ 1.5 times lower/higher than the observed value, resulting in an approximately 18.75% change in f_p, whereas the model-simulated mean z_0 value for the north-northeasterly wind regime was found to be approximately equal to the observed value except for very few high cases (a total of 4 observations were higher). Therefore, the average relative error in f_p due to variation in z_0 ($R_{z_0}^{f_p}$) would be of the order of 0.125 (12.5%).

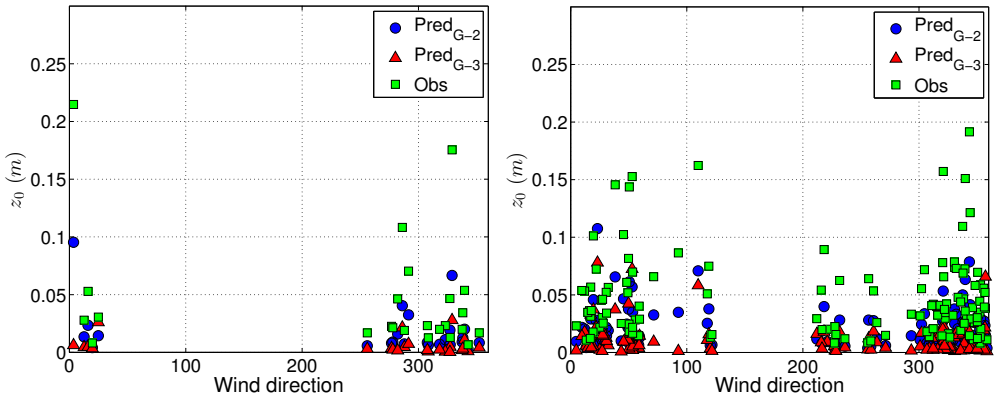

Figure 4.5: Comparison of the filtered model predicted z_0 values at the G-2 and G-3 masts with observations for the (a) autumn and (b) spring campaigns. The observed values of z_0 were obtained from the profile measurement.

Furthermore, changes in f_p were estimated by changing the input variables L, σ_v, $u_\star$ and U_{mean} of the model within a reasonable range for $1/L > 0$ and for $1/L \leq 0$ cases. The surface source area of our model was already defined, so that the sensitivity of f_p was tested over a domain of 100 $\times$ 140 m for a north-northeasterly wind (wind direction = 42.24^0 and z_m = 0.86 m) and for a fixed set of data σ_v = 0.18, $u_\star$ = 0.15 m s^{-1} and U_{mean} = 1.38 m s^{-1}.

For a stable atmospheric case of 1/*L* = 0.1, if the 1/*L* values were perturbed within a range of ±50.0%, the mean change in the f_p value was found to be between 1.3%-2.6%, indicating the mean relative error in f_p from variations in $1/L$ ($R^{f_p}_{1/L}(s)$) is of the order of 0.0195 (1.95%). The 50% error range was chosen for the L term because $u_\star$ and heat flux terms contribute substantially to L as they can have errors between 10 - 15%. Similarly when 1/L was assumed to be -0.1 (unstable) the mean relative error in f_p from $1/L$ ($R^{f_p}_{1/L}(u)$) was found to be of the order of 0.0172 (1.72%). '*s*' and '*u*' indicate stable and unstable atmospheres.

Next, the $u_\star$ values were also perturbed with a ±10.0% error for stable ($1/L = 0.1$) and unstable ($1/L = -0.1$) cases. The $R^{f_p}_{u_\star}(s)$ was found to be 0.0068 (0.68%) and the $R^{f_p}_{u_\star}(u)$ was found to be 0.0017(0.17%). Similarly for the U_{mean}, $R^{f_p}_{U_{mean}}(s)$ was found to be 0.00625 (0.625%) and $R^{f_p}_{U_{mean}}(u)$ was found to be 0.0017 (0.17%); and for σ_v, ${R_{\sigma_v}}^{f_p}(s)$ was found to be 0.0005 (0.05%) and ${R_{\sigma_v}}^{f_p}(u)$ was found to be 0.0001 (0.01%). Compared to the relative error from z_0 ($R^{f_p}_{z_0}$), errors from *L*, σ_v, $u_\star$ and U_{mean} were found to be very small, although it should be noted that the error sensitivity analysis was performed only for a ± 10.0% error range and only mean values were considered, rather than the maximum values. Finally, the mean random error in f_p was estimated as follows:

$$R^{f_p} = \left({R^{f_p}_{z_0}}^2 + {R^{f_p}_{1/L}}^2 + {R^{f_p}_{u_\star}}^2 + {R^{f_p}_{U_{mean}}}^2 + {R^{f_p}_{\sigma_v}}^2 \right)^{1/2} \tag{4.12}$$

The $R^{f_p}(s)$ value was found to be in the order of 0.1288 (12.88%) whereas the $R^{f_p}(u)$ value was found to be 0.1266 (12.66%). Now, if we consider that the total uncertainty in our emission rate values is the summation of error from the diffusivity parameter ($R_{d^p_h}$), concentration gradients ($R_{\Delta C_{N_2O}}$) and footprint function (R^{f_p}) then the mean propagated error in the emission rates (R^{Recal}_{flux}), $R^{Recal}_{flux} = \sqrt{R^{p\,2} + {R^{f_p}}^2}$, would be approximately of the order of 16.53% irrespective of stability, where R^p is described in McMillan et al. (2012), Mukherjee et al. (2013) and Chapter 3. Irrespective of stability, the mean R^p value is considered to be 0.105 (10.5%), as R^p for stable and unstable atmospheric condition was found to be 0.12 (12%) and 0.09 (9%), respectively.

4.4.2 bLs model setup

The WindTrax model was setup only for subplot A as this plot was a control and terminal plot and required only a single continuous simulation for source area emission

rate estimation. The measurement plot was defined by a rectangle of width 140 m and length 100 m. The field orientations were 340^0 with respect to true north. A fixed z_0 of 0.03 m was used in all the simulations. Instead of using the sonic anemometer turbulent intensity measurements directly in the WindTrax setup, pre-filtered time averaged wind speed, wind direction and temperature were provided directly to the model. Similarly, *L* measurements were used directly in the WindTrax surface layer model.

Since the proposed approach to estimation of source area emission rate largely depends on the footprint fraction values obtained from the Kormann and Meixner (2001) model, at first, the analytical footprint fractions were compared with values obtained from a 'forward' simulation of the bLs setup (see Section 4.4.3.1 for detail). This would also verify the consistency of the analytical footprint model of Kormann and Meixner (2001) under different atmospheric stability conditions and corroborate that the module is realistic. Next, the source area emission rates of the control plots obtained from the proposed numerical setup ($ER_{F^0_{eqn}}$) were compared with the emission rates obtained from the 'backward' simulations of the bLs model (ER_{model}). Since a proper background concentration (C_b) was not measured during both of our field experiments, and the bLs predicted emission rates (ER_{model}) can vary substantially depending on the background concentrations of N_2O (Flesch et al., 2004), the ER_{model} values were estimated by using concentration measurements at the 0.5 m and 1 m height of each mast for a single source area. The measurement masts were fixed upwind to the plots and no C_bs were prescribed, instead the C_bs were obtained as model output (details are given in Section 4.4.3.2).

A total of 20,000 particles were released for each simulation and the particle dispersion track was followed up to 600 and 300 m in the experiments described in Sections 4.4.3.1 and 4.4.3.2, respectively. This particle track distance covers the entire field in all directions.

4.4.3 Comparison with analytical model

4.4.3.1 Comparison of the footprint fraction values

The bLs model for this case was simulated in a 'forward mode' to estimate footprint fractions (γ) from the concentration gradients elevated above the background. The WindTrax model was simulated only for subplot A, defined as the emitting area, of the autumn and spring experiments. Similar to Figure 4.1, all the rectangular subplots were described in the model along with four measurement masts having concentration

sensors at 0.5 m and 1.0 m. The measured concentrations were defined as unknown at each mast and the C_bs were fixed to 0 for subplot A. The measured emission rates for subplot A were defined as equal to 1. The observed wind and turbulence data were provided to the 'Surface layer model' and to the 'Atmosphere model' of WindTrax. The forward simulation of this setup would then produce the elevated concentrations at 0.5 m and 1.0 m height at each mast and the concentration gradients (ΔC) were estimated for each mast. As a result, the footprint fractions of subplot A were estimated from the bLs model at each mast following:

$$\gamma_1^A(bLs) = \Delta C_1 / \left(\Delta C_1 + \Delta C_2 + \Delta C_3 + \Delta C_4 + \Delta C_0\right) \tag{4.13}$$

where $\gamma_1^A(bLs)$ is the footprint fraction measured at G-1 for subplot A from the bLs model and ΔC_0 is the extra gradient term unaccounted for by the masts. Similarly, $\gamma_{2,..,4}^A(bLs)$ can be estimated. Now, it has to be kept in mind that Equation 4.13 and the above mentioned condition would be satisfied if the wind direction is aligned with the field, when the ΔC_0 term should approach 0. Therefore, for simplicity, only those cases were considered below where the wind direction was between 320^0 and 360^0 to represent an approximate northerly aligned wind. However, when the γ_1^A values were compared with the $\gamma_1^A(bLs)$ values from the above mentioned condition, a systematic bias was observed in $\gamma_1^A(bLs)$. Therefore to compensate for this error, $\gamma_1^A(bLs)$ values were further computed using $\Delta C_0 = 0.1\Delta C_1$. This 10% estimate was obtained after a small sensitivity study and new values were compared.

Ratios of the γ_1^A and $\gamma_1^A(bLs)$ as a function of $1/L$ are shown in Figure 4.6. The mean absolute differences in footprint fraction values ($|E| = |\overline{\gamma_1^A} - \overline{\gamma_1^A(bLs)}|$) are shown in the lower panels of the same figure. For the autumn experiment, marginally higher $|E|$ values were observed for $1/L > 0$ cases with an overall high observed correlation coefficient (0.58 with p-value < 0.001) between $\gamma_1^A(bLs)$ and γ_1^A, whereas a correlation coefficient value of 0.66, with p-value < 0.001, was observed in spring between $\gamma_1^A(bLs)$ and γ_1^A. On average, a 10% enhancement in these correlation coefficient values were observed when only the near neutral ($|1/L| < 0.1$) cases were considered.

4.4.3.2 Comparison of the surface emission rates

Emission rates from each control plot were obtained using a similar set up to that described in Section 4.4.3.1, except for the fact that both 0.5 m and 1 m concentrations

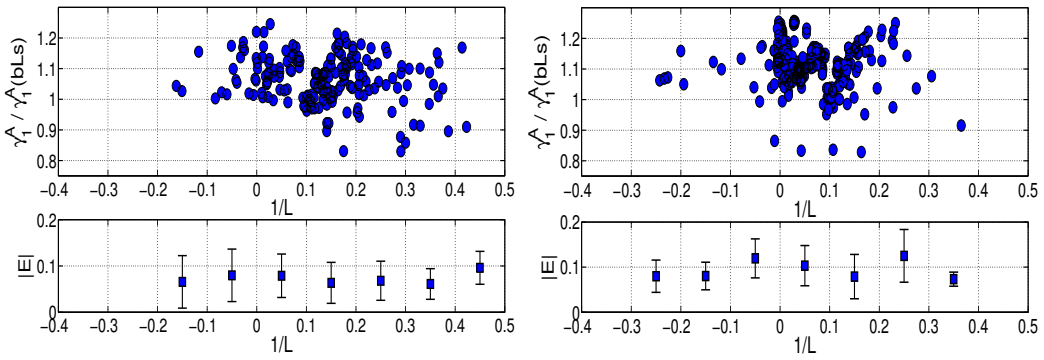

Figure 4.6: Comparison of the footprint fraction values obtained from the analytical footprint model and the bLs model for subplot A of (a) autumn and (b) spring experiment. The observed mean and standard deviation of errors between the two footprint fractions are shown in the bottom panels for respective seasons.

were used as known concentrations and no C_bs values were provided. Rather C_bs were produced as model output from the 'backward' run of the model. Since measured concentrations were provided at two heights with unknown emission rates from a single plot, a unique solution for this setup was available. Emission rates obtained with this setup are shown in Figure 4.7 for the autumn and spring experiments, respectively. During the comparison, 10 and 30 ER_{bLs} values of autumn and spring were neglected as they were unrealistically large ($ER_{bLs} > 1500$ $gN_2O\text{-}N.ha^{-1}.day^{-1}$). These values were mostly associated with $1/L \geq 2.0$ and/or high windspeed (U $\geq$ 4.0 m s^{-1}). The correlation coefficients between $ER_{F^0_{eqn}}$ and ER_{bLs} for both seasons were found to be 0.70 and 0.61 respectively, with p-value < 0.0005. Similarly the slopes of the regression lines were found to be 0.91 and 0.43, respectively for autumn and spring.

Now, to find out the significant difference between $ER_{F^0_{eqn}}$ and ER_{bLs}, a second linear regression was performed between them by reversing the variables. Then slopes were estimated. Next, inverses of the slopes were computed and found to be 1.32 and 1.20 for autumn and spring, respectively. Finally, the arithmetic means were computed between the two different slopes, e.g. arithmetic mean of 0.91 and 1.32 = 1.115 and arithmetic mean of 0.43 and 1.20 = 0.815. Since, these arithmetic mean values were not significantly < 1 (or > 1), it can be concluded that the ER_{bLS} values were approximately equivalent to $ER_{F^0_{eqn}}$ values.

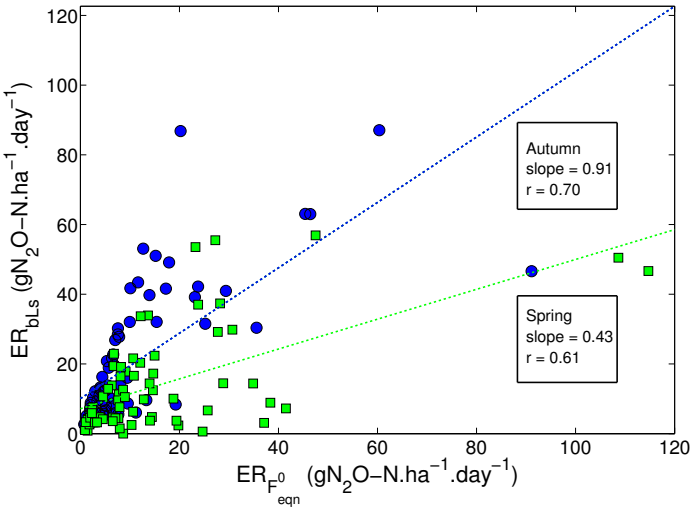

Figure 4.7: Comparison of emission rates from numerical method ($ER_{F^0_{eqn}}$) and bLs model (ER_{bLs}) for subplot A of autumn (shown in blue circles) and spring (shown in green squares) campaign. The red and blue lines indicate the fitted linear regression between $ER_{F^0_{eqn}}$ and ER_{bLs}. The intercept, slope and correlation coefficient (r) values for each campaign are shown inside the textboxes.

4.5 Conclusion

We developed a method to account for varying footprint functions in a multiplot micrometeorological comparison of N_2O fluxes. The framework incorporated a calculation of footprint fractions using the model of Kormann and Meixner (2001), together with solving a set of linear equations to estimate source area emission rate for a specific field treatment. A mathematical solution of background flux has been provided for those situations where no background flux measurement was made. Since this new approach of emission rate estimation is fundamentally dependent on the footprint fraction values of a particular field, footprint fractions, obtained from the analytical footprint model, were tested with values from a bLs model. The analysis revealed that 4.3% of the fluxes attributed to treatment plots (without footprint correction) were contaminated with fluxes from outside the plot boundaries. The maximum amount of contamination was 30%. The background flux when computed using the numerical solution provided in this study was found to be sensitive to the measured flux and atmospheric surface layer flow property. However, the proposed emission rate estimation formulas has been found to work well. The actual emission rates from the proposed method were found to be on average 2.1% higher than the measured flux values for the control plots which can increase up to 6% based on the realistic computation of F^0. These enhancements in the emission rate values are due to the footprint correction

which includes the surface layer flow property and geometry of the field. A higher actual emission rate than the measured flux is expected under an approximately fixed background flux of N_2O as the footprint fraction will seldom have the idealistic value of 1 and corresponding flux value.

To verify the consistency of the analytical footprint model for varying atmospheric stabilities, a forward simulation of a backward Lagrangian stochastic model was used to derive footprint fractions which were compared. A good agreement (correlation coefficients of 0.58 and 0.66) between the analytical and the bLs model footprint affirms the realistic nature of the analytical model. The correlation coefficients were found to increase by 10% when only the near neutral cases were considered. Finally, when the emission rates obtained from this new approach were compared with the bLs simulated emission rates of a control plot, it was found that the proposed method worked well when the atmospheric stability $|1/L| \leq 0.2$.

This study is focused on the development of a method of estimation of surface emission rates from the measured flux and footprint fractions which also includes the field geometry and atmospheric surface layer flow. Therefore, an in-depth analysis of the effect of mitigation on the treated plot was not performed. Again, it has to be remembered that rigorous data processing is necessary before one uses this approach for actual source area emission rate estimation. Extra precaution should be taken for computing the background flux following our proposed mathematical formula as it is highly sensitive to the measured fluxes at different locations.

Chapter 5

Assessment of grazing and mitigation effects on nitrous oxide flux

5.1 Introduction

Animal grazing is carried out over the green pastures of New Zealand throughout the year, and animal excreta is assumed to be one of the major sources of soil nitrogen to these green pastures. About 70% to 90% of the consumed nitrogen by the cattle is returned back to the grazing field in form of urine and dung (Di and Cameron, 2002b; Bolan et al., 2004), and depending on stocking rate[1], approximately 30% of a grazed field is found to be covered with urine patches (Qui et al., 2010). As a consequence of the excessive nitrogen deposition through urine and faeces, a considerable amount of inorganic-N is found to be unused in the dairy farm soils of New Zealand (De Klein and Eckard, 2008), which enhances the N_2O production and NO_3^- leaching through nitrification and denitrification processes. However, N_2O has a substantial potential for emission reduction. Efforts have already been made world-wide to reduce the N_2O emission by using different management practices and mitigation techniques, some of which can be found in Bolan et al. (2004). Primarily, these mitigation approaches try to increase the efficiency of nitrogen fertilizer use and optimize the spatio-temporal nitrogen content of the agricultural fields (Saggar et al., 2008). In New Zealand, application of a nitrification inhibitor is gaining interest as a means to mitigate the nitrous oxide flux from paddocks. Specifically, usage of DCD (abbreviation of a chemical called dicyandiamide (2-Cyanoguanidine)) is gaining interest as it inhibits the oxidation of NH_4^+ to NO_2^- and can be used as a slow nitrogen fertilizer (Di and Cameron, 2002a).

[1] It is defined as the number of cattle grazing per hectare of paddock.

Several field trials of DCD were found to be promising in reducing the N_2O emission as decreases of approximately 40-80% in the N_2O emission rates were noted (Di and Cameron, 2002b,a, 2003; Di et al., 2007; Qui et al., 2010). However, the effectiveness of DCD largely depends on the soil texture, pH, temperature and climatic conditions and some soil property based N_2O emission study can be found in Singh et al. (2008).

The aforementioned studies have also revealed that the mitigation of N_2O flux through DCD application has higher effectiveness in autumn, winter and early-spring as compared to summer, which raised the question of ineffectiveness of DCD in summer. However, Qui et al. (2010) have explored the effectiveness of DCD over control and urine patches of a paddock in summer and showed that DCD can potentially reduce 40% of the N_2O emission rate. In a broader sense, most of the previously mentioned studies have found a reduction in the N_2O flux values from paddocks of New Zealand when treated with DCD over urine patches irrespective of season, but apparently, all of the aforementioned studies were conducted using chambers and Lysimeters over a controlled environment, neglecting the larger meteorological influences and diffusion processes of the atmosphere. However, such meteorological influence and/or diffusion process can be an important control factor of emission rate and should be taken into consideration.

Therefore, the present study is aimed at using a top-down micrometeorological method to verify the effect of mitigation on N_2O emission rates, which includes the meteorological controls into consideration and hence, has a larger spatio-temporal scale and enhanced degrees of freedom. Furthermore, effects of grazing and irrigation on the measured N_2O flux values are also explored. We have already mentioned in Chapter 4 that the measured flux values have a functional relationship with the actual source emission rate, which implies a high possibility that the actual source emission rate from the mitigated plots could be different from the measured values. This should also be investigated. Therefore, emission rates from the mitigated plots are also computed using the analytical footprint method described in the previous chapter, and compared with the control plots.

Section 5.2 of this chapter describes the field activities during the autumn and spring campaigns. The effect of grazing has been discussed in Section 5.3.1. Measured flux values from the mitigated plots are described in Section 5.3.2 and compared with the control plots in Section 5.3.3. The effect of mitigation on the actual emission rates of the mitigated plots is explored in Section 5.3.4 and a discussion of the results has been provided in Section 5.4.

5.2 Description of field activity

The N_2O flux measurement and mitigation experiments were carried out in autumn, between 9 May 2010 to 21 June 2010, and in spring, between 24 September 2010 to 22 November 2010. The mitigative experiments were carried out using the nitrification inhibitor DCD with different concentrations of urea and cow-urine. The soil type of our field site was Lismore Silt Loam[2]. As mentioned in Chapters 3 and 4, the experimental paddock was divided in to 5 subplots of which subplots B and D were used as experimental plots, e.g. treated with DCD, and the rest were used as control plots, e.g. untreated plots.

The entire paddock was grazed by 450 cows twice during the autumn experiment. The first grazing took place between 11-14 May, 2010 and the second one between 30 May and 2 June, 2010. Consecutively, measurements were unavailable during these periods. A total of 65 kg/ha of ammonium urea fertilizer was applied over the paddock on 13th May 2010 and DCD was applied to plots B and D on 19th May 2010. The field activities of the autumn experiment are shown in Figure 5.1a along with daily total rainfall values in mm.

During the spring campaign, the paddock was grazed by 428 cows three times between 28-29 September, 20-22 October and 6-8 November, 2010. DCD was applied to plot B on 7th October 2010. The whole paddock was treated with liquid urea on 12th October 2010 with an extra 30 kg/ha of urea applied to plot D. Figure 5.1b shows the field activity along with the total rainfall for the spring experiment.

5.3 Results

5.3.1 Effect of grazing on the measured flux values

It has been already mentioned in Chapter 4 that the measured flux values at F^1 to F^4 could be assigned to subplots A to D and B to E, respectively for northerly and southerly wind bisectors, and can be termed as 'measured flux' for the adjacent plot, although, such measured flux would not be the actual emission rate as the actual emission rate has to be computed after a footprint correction. However, such measured flux for an individual plot can provide useful information if it is assumed that the footprint ellipse covers most of the predefined area, irrespective of time and surface layer sta-

[2]This type of soil is common in mid Canterbury and can be found as a thin layer (approximately 30 cm) over the gravel. Properties of the Lismore soil can be found in Di and Cameron (2002a).

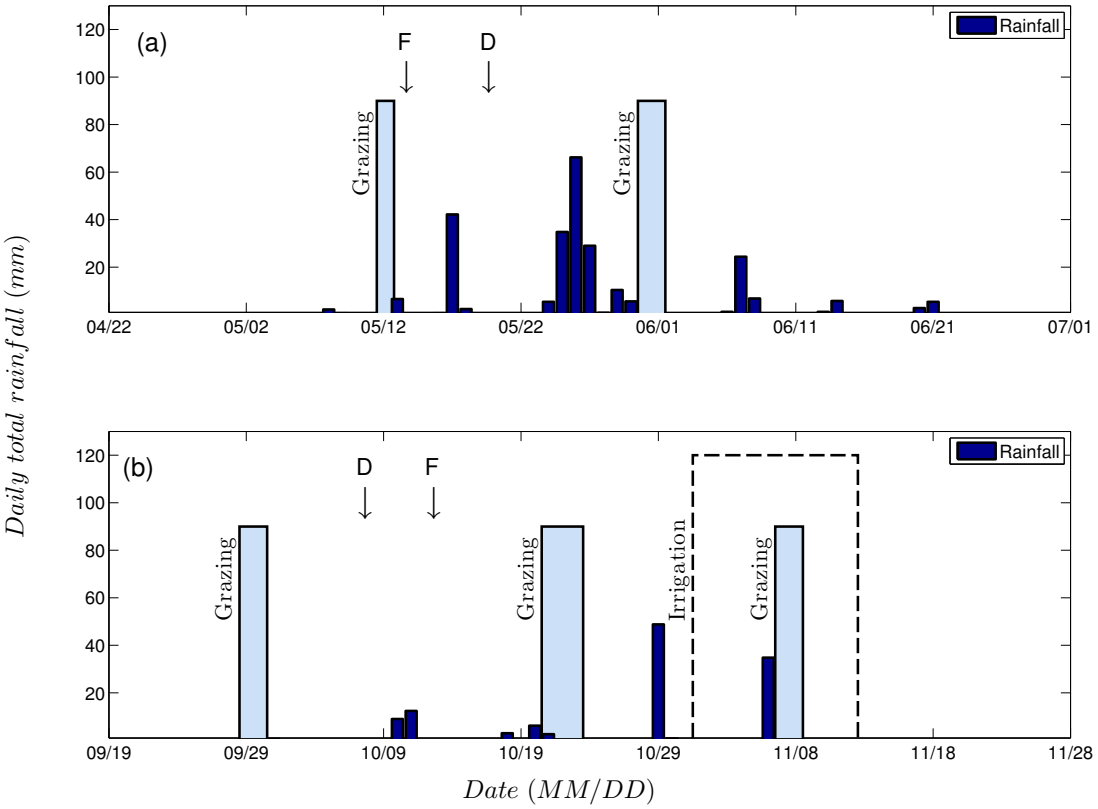

Figure 5.1: Field activity for the (a) autumn and (b) spring campaign is shown with the daily total rainfall. 'F' and 'D' represents those dates when fertilizer and DCD were applied. Grazing days are marked with the rectangles. The irrigation period for the spring campaign is shown with a dotted rectangle. Heights of these rectangles do not provide any information.

bility. Again, in the last chapter it was shown that the height-to-fetch ratios for most of the measurements were within 1:100 and the footprint corrected actual emission rates were less 5% higher than the 'measured flux' values, which implied that the assignment of the measured flux at any mast to the nearby plot based on wind direction was realistic (excluding percent corrections). Therefore in this chapter, the measured flux values are explored to investigate the effect of grazing and mitigation on the N_2O emission.

Since the number of observations was few for the pre and post-grazing periods of the autumn campaign, only the spring campaign data from the control plot A and experimental plot B were used to investigate the effect of grazing on N_2O emission rates. Flux values were compared for the period 13 October 2010 at 0010 hrs to 19 October 2010 at 2350 hrs as pre-grazing (7 days) and 23 October 2010 at 0010 hrs to 29 October 2010 at 2350 hrs as post-grazing (7 days). Since fertilizer was applied over the entire paddock on 12 October 2010, measured flux values from the pre-grazing period represent the emission rate enhanced by fertilization. The daily mean measured

flux along with SE[3] values for these pre and post-grazing periods are shown in Figure 5.2. During the pre-grazing period, the mean measured flux was found to be 20.36 and 11.96 $gN_2O\text{-}N.ha^{-1}.day^{-1}$ for subplot A and 10.56 and 8.26 $gN_2O\text{-}N.ha^{-1}.day^{-1}$ for the subplot B, respectively for the CSAT3 and the Gill measurements. These mean values were obtained as averages of 7 days of fluxes. The large difference in the flux values of subplot A between CSAT3 and Gill is attributed to unavailability of the diffusivity parameters from the CSAT3 for the first three days before grazing. One can also see from Figure 5.2a that fluxes from both subplots increased significantly after the fertilizer application on 12 September and achieved a maxima of $\approx$ 25 and 20 $gN_2O\text{-}N.ha^{-1}.day^{-1}$ for subplots A and B, respectively, after 3 to 4 days. Such enhancement in the N_2O gas emission after fertilizer application has also been reported previously by Saggar et al. (2004) and Luo et al. (2008b), and modeled by Grant et al. (2006).

A continuous decreasing trend in the measured flux was followed in both subplots after grazing, as shown in Figure 5.2b, with an exception on day 6 of subplot A for the CSAT3 flux. This high value was attributed to a higher estimation of diffusivity parameter by the CSAT3 anemometer. The post-grazing mean measured flux values from the CSAT3 and Gill anemometers were found to be 24.90 and 23.40 $gN_2O\text{-}N.ha^{-1}.day^{-1}$ for subplot A and 16.84 and 23.32 for subplot B, respectively. Irrespective of the sonic instrument, the measured flux was found to increase 58.9% for subplot A and 120.8% for subplot B for the post-grazing periods. Irrespective of the measurement plot, an approximate 90% enhancement in the flux values was observed after grazing (p-value < 0.01). A similar result was also obtained by Saggar et al. (2004) who found the N_2O emissions from the ungrazed pastures were less than 10% of those of the grazed pastures. Therefore, it can be inferred that this FG-EC measurement system has the ability to distinguish certain biogenic changes in the flux values.

5.3.2 Measured flux from the experimental plot

Similar to Chapter 3, only those observations were chosen for subplots B and D where both the CSAT3 and Gill flux values were available. The mean N_2O flux values with SE for subplots B and D are shown in Table 5.1. One has to note that these mean values were calculated over the total selected population and, therefore, do not represent the daily mean fluxes. The daily mean measured fluxes are shown in Figure 5.3 for both

[3]Standard error is already defined in the previous chapter as: SE = $\sigma_{fluxes}/\sqrt{N}$, where σ_{fluxes} is the standard deviation of fluxes and N is the number of observations.

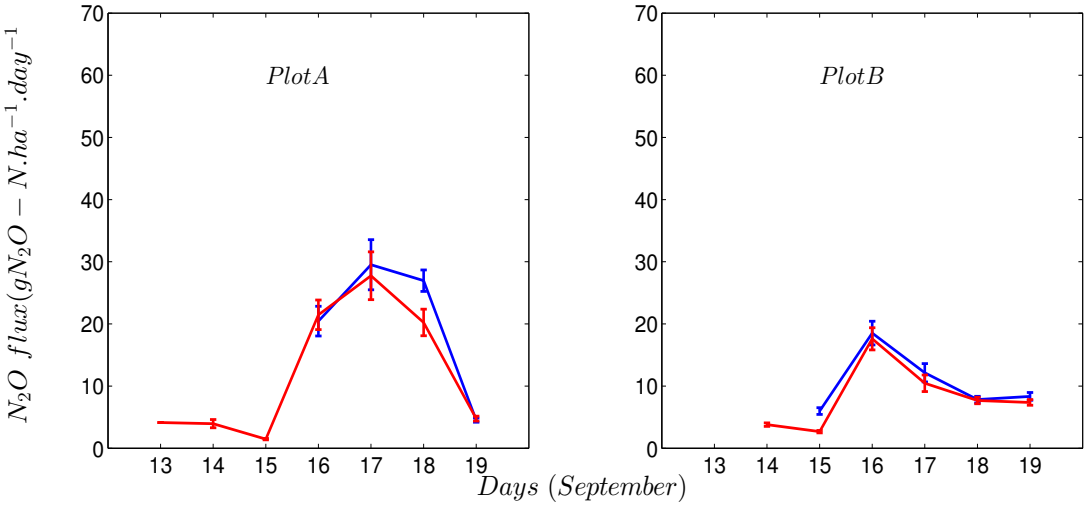

(a)

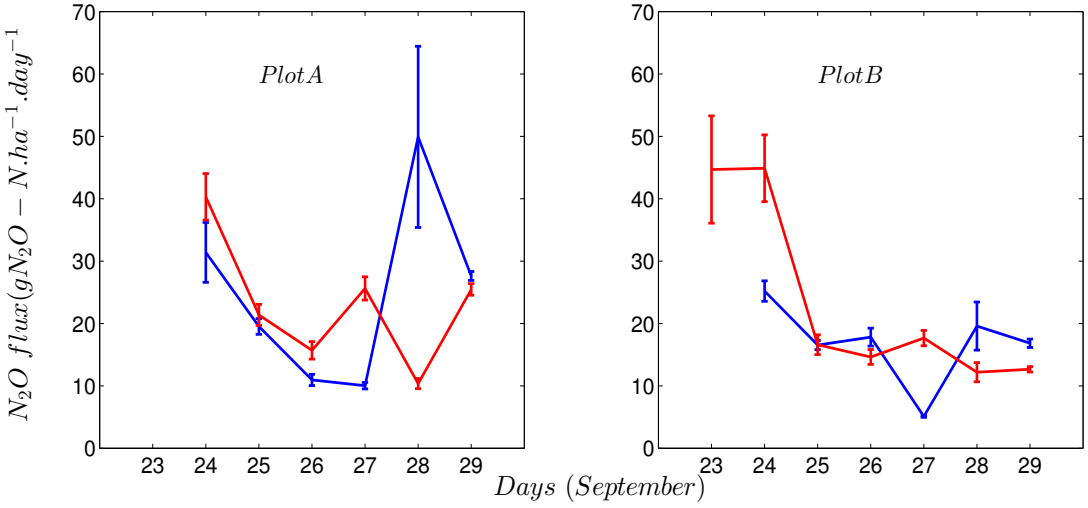

(b)

Figure 5.2: Daily mean nitrous oxide flux values (mean ± SE) for (a) Pre (13-19 September, 2010) and (b) post (23-29 September, 2010) grazing are compared between subplot A and B of spring experiment. Blue lines are for flux values using CSAT3 diffusivity and red lines are from Gill diffusivity.

campaigns and show no reduction in the measured flux values for mitigated plots. However, fluxes obtained using transfer coefficients from CSAT3 and Gill anemometer were found to be highly comparable as correlation coefficients were higher than 0.80 (with 99.9% confidence level) for all the cases mentioned in Table 5.1.

The maximum flux values for subplots B and D within the total accepted samples (shown in parenthesis) were found to be 137.8 and 268.2 $gN_2O\text{-}N.ha^{-1}.day^{-1}$ in autumn and 491.8 and 275.0 $gN_2O\text{-}N.ha^{-1}.day^{-1}$ in spring, respectively. These maximum daily fluxes were estimated comparing both the CSAT3 and Gill observations,

Table 5.1: Comparison of flux values estimated using parameterisation (p) and thermal (t) methods from CSAT3 and Gill data. Mean ± Standard Error values of N_2O flux ($gN_2O\text{-}Nha^{-1}day^{-1}$) are shown for the autumn and spring campaigns. Total numbers of observations are shown in parenthesis.

Season	Plots	N_2O flux ($gN_2O\text{-}N.ha^{-1}.day^{-1}$)			
		$CSAT3_p$	$Gill_p$	$CSAT3_t$	$Gill_t$
Autumn	*Plot-B*	13.4±1.68 (139)	13.2±1.54 (139)	11.9±2.92 (46)	11.8±4.47 (46)
	Plot-D	9.9±1.05 (132)	10.5±1.05 (132)	9.3±1.74 (34)	6.9±1.40 (34)
Spring	*Plot-B*	7.3±0.72 (151)	7.4±0.82 (151)	10.7±1.91 (53)	7.4±1.29 (53)
	Plot-D	7.2±0.86 (144)	7.3±0.90 (144)	16.6±5.08 (44)	11.6±4.08 (44)

and were found to be within the same range of previously published reports of Saggar et al. (2010), although the average maximum flux from chamber measurement was reported to be lower, at 150 $gN_2O\text{-}N.ha^{-1}.day^{-1}$ (Saggar et al., 2004; Luo et al., 2008a).

5.3.3 *Effect of mitigation on the measured flux and comparison with the control plots*

During the autumn experiment DCD was applied to plots B and D on 19 May and the second grazing started on 30 May, so that measured fluxes from all the subplots were compared for the period 20 May, 0015 Hrs to 28 May, 2345 Hrs (9 days). Panels (b) and (c) of Figure 5.4 show the daily mean of measured flux values for subplots B, C and D using transfer coefficients from the CSAT3 and Gill anemometers, respectively. The total daily rainfall for the described period is shown in panel (a). A decreasing trend in the N_2O flux values was observed for both control (subplot-C) and experimental subplots (subplot-B and D), but compared to the control subplot C no reductions in the fluxes were observed for subplots B and D. The 9-day arithmetic mean flux values of subplots B, C and D were found to be 32.6, 30.4, and 31.7 $gN_2O\text{-}N.ha^{-1}.day^{-1}$ from CSAT3 diffusivities, and 26.4, 28.6 and 20.6 $gN_2O\text{-}N.ha^{-1}.day^{-1}$ from Gill diffusivities, respectively. These 9-days mean and the daily mean values (as shown in Figure 5.4) are comparatively higher than the experimental periodical mean. Such enhanced emission of N_2O between 17 May and 22 May might probably be associated with the occasional burst of N_2O which has also been reported in Harvey et al. (2008b) and many others.

Similar to the autumn experiment, 12 days of the spring experiment data between

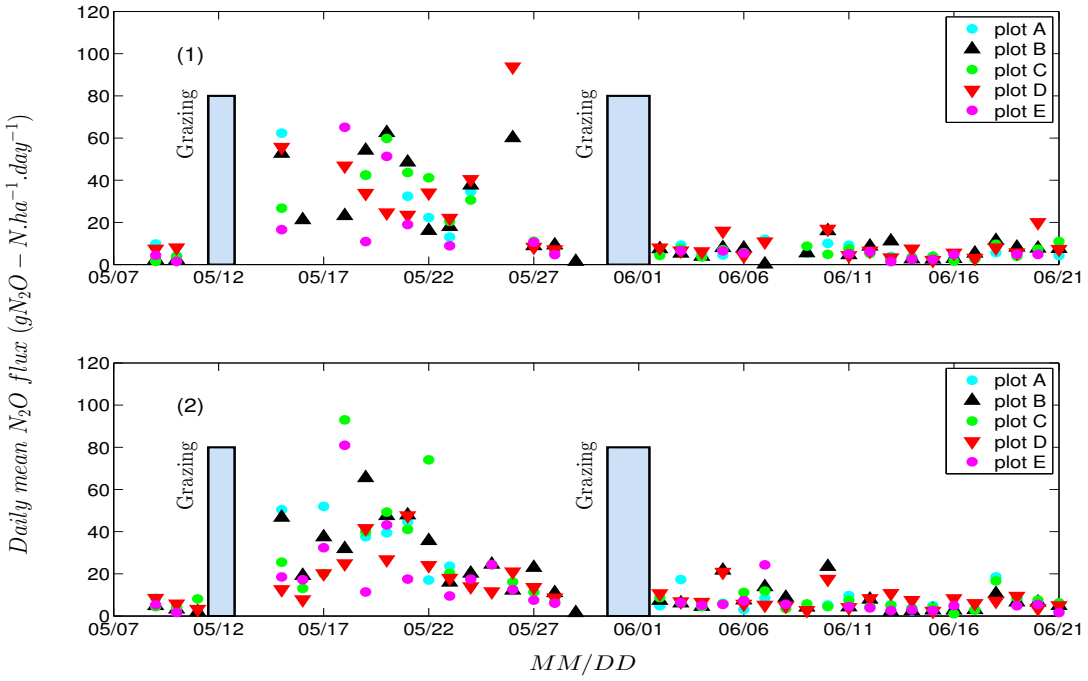

(a)

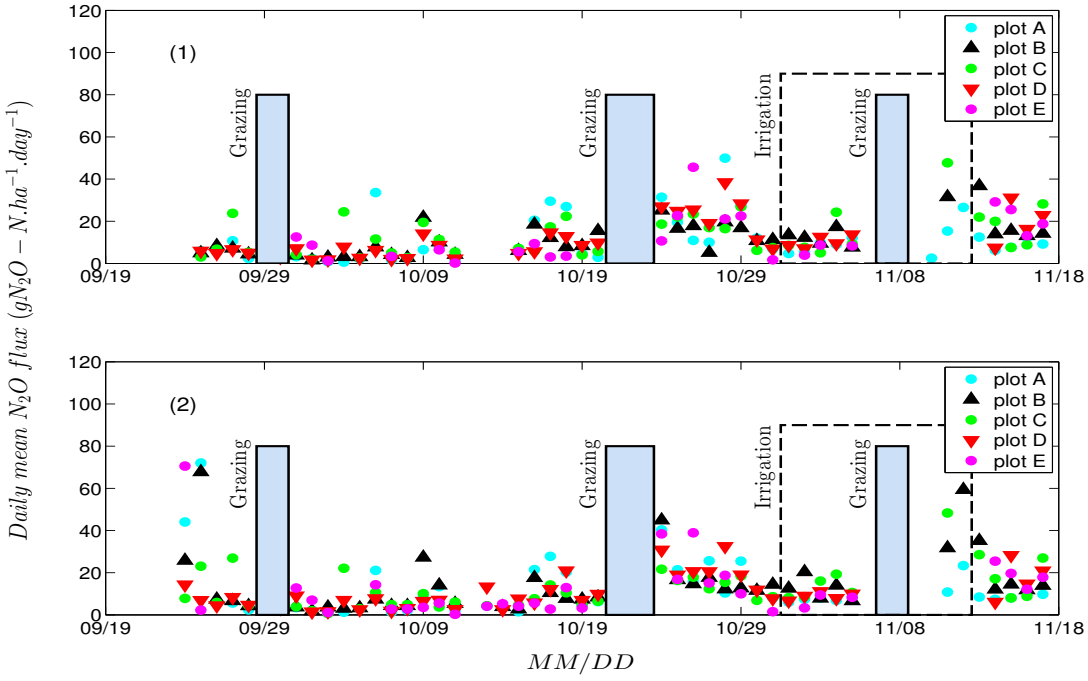

(b)

Figure 5.3: Daily mean nitrous oxide fluxes for all the subplots from the (a) autumn and (b) spring experiments. Panels (1) and (2) indicate flux values using transfer coefficients from the CSAT3 and Gill measurements, respectively. Heights of these rectangles do not provide any information. Comparatively high daily flux values were observed for all the subplots during 17 to 28 May of autumn campaign and has also been shown in Figure 3.8.

8 October 2010 at 0010 Hrs to 19 October 2010 at 2350 Hrs were analyzed to explore the effect of DCD on the measured flux values. DCD was applied over subplots B on 7 October and extra fertilizer was applied over subplot D on 12th October, and comparison of the daily arithmetic mean of the measured fluxes from subplots B, C and D are shown in Figure 5.5. Panel (a) of Figure 5.5 shows the daily total rainfall for the 12 day period. Similar to autumn, no significant reduction in the flux values were observed for this experiment. The 12-day average flux values of subplots B, C and D were found to be 10.17, 10.63 and 8.23 $gN_2O\text{-}N.ha^{-1}.day^{-1}$ from CSAT3

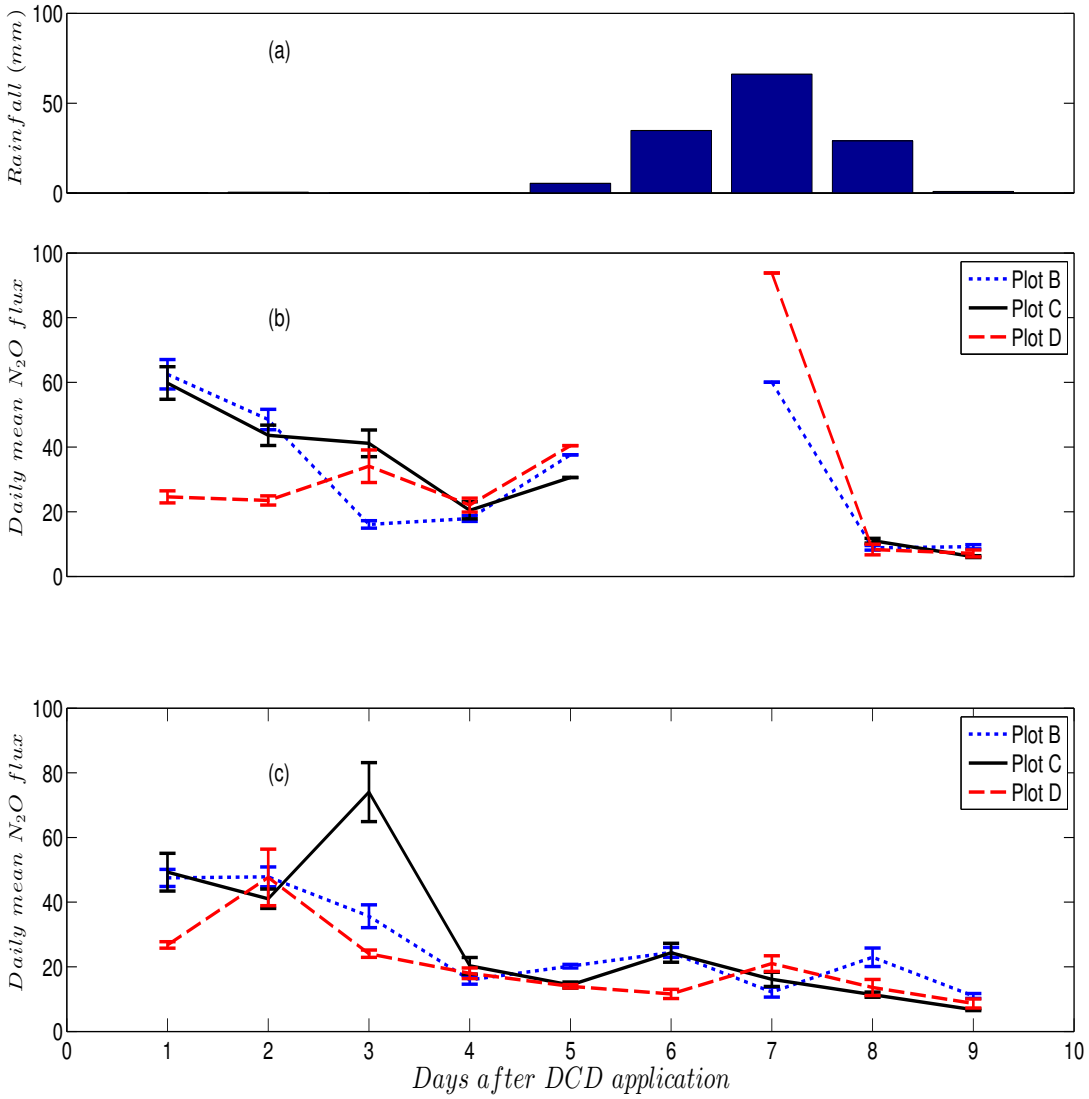

Figure 5.4: Panel (a) shows the total rainfall of each day after DCD application. Changes in the daily mean N_2O flux values (mean±SE) in $gN_2O\text{-}N.ha^{-1}.day^{-1}$ are compared for all subplots of the autumn experiment after DCD application. Panels (b) and (c) show N_2O flux values from CSAT3 and Gill measurements, respectively.

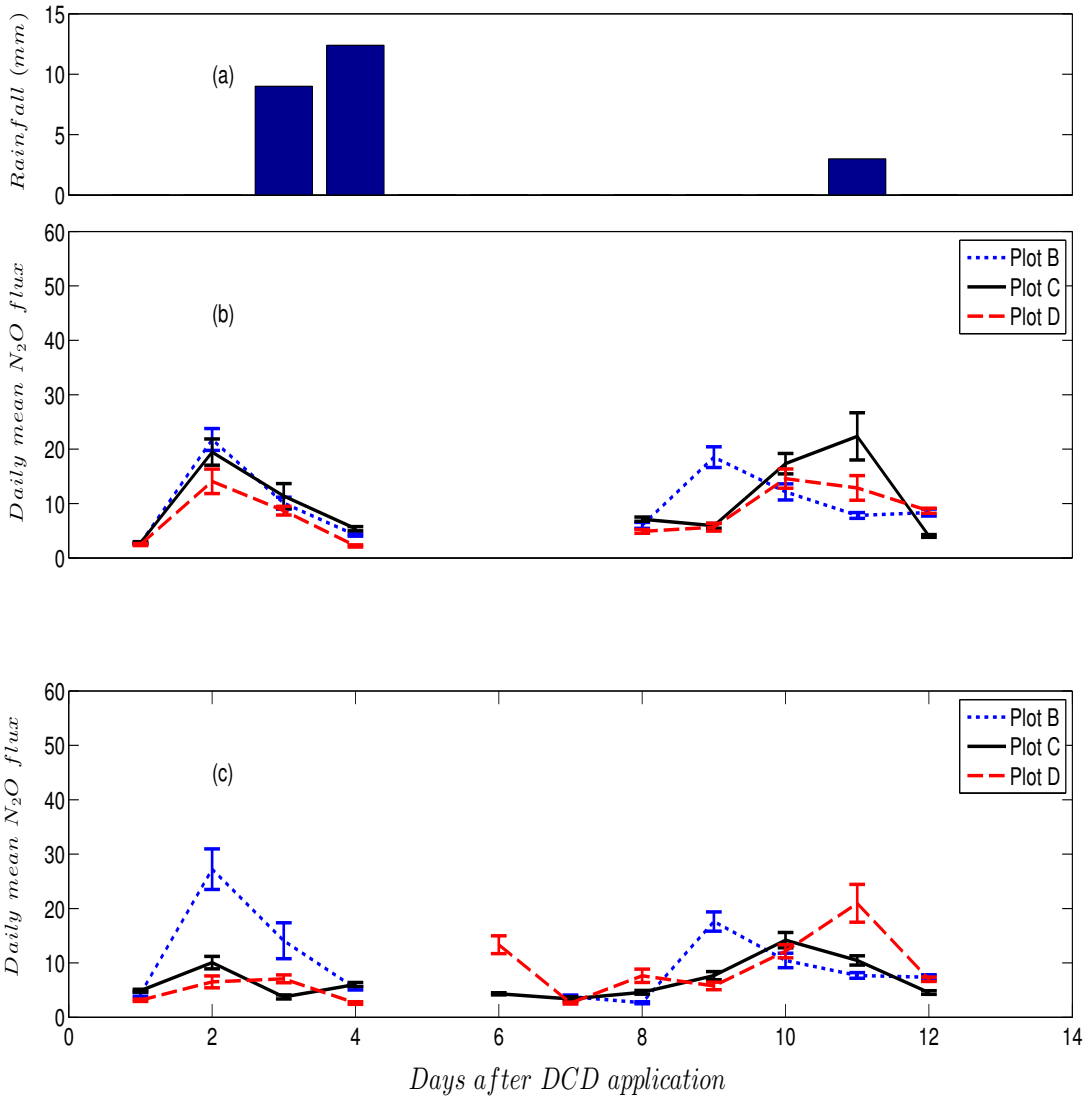

Figure 5.5: Same as Figure 5.4, but for the spring experiment.

diffusivities, and 10.04, 6.71 and 8.07 $gN_2O\text{-}N.ha^{-1}.day^{-1}$ from Gill diffusivities, and no substantial effect of mitigation was observed. Furthermore, when the daily mean flux values of 13 to 19 October were compared for subplots B, C and D, an increasing trend the in the emission rates of subplot D was observed in the Gill data, but was significant (with p-value < 0.05).

5.3.4 Effect of mitigation on N_2O emission rates from the experimental plots after footprint correction

In Chapter 4, surface emission rates of N_2O from control plots were obtained using a relationship between an analytical footprint function and the measured flux values. The background flux values (F^0) were obtained by solving Equation 4.9 of Chapter 4. A mean value of the stable solution of F^0 was used as fixed F^0 and the emission rates were estimated. Comparison of the emission rates obtained from the footprint fraction approach ($ER_{F^0_{eqn}}$) with bLs model simulated values (ER_{bls}) showed a good agreement within a wide range of atmospheric surface layer stability ($|1/L| < 0.2$). That has corroborated the realistic nature of the proposed numerical framework over a wide range of atmospheric stability. Since comparison of the measured flux values between the control and mitigated plots showed no significant reduction of N_2O emission after the DCD treatment, the $ER_{F^0_{eqn}}$ values are explored in this section for the mitigated plots, as it is assumed that the $ER_{F^0_{eqn}}$ will reflect the actual source area emission rate and might contain some practicable information.

It should be noted that a similar mitigative treatment to two different plots can invoke different results in N_2O emission rate as N_2O production is highly spatio-temporally variable in the soil and the N_2O production rate varies with different soil types. Therefore, values obtained here may differ from those in some of the earlier published reports.

The actual emission rates ($ER_{F^0_{eqn}}$) were computed using only those diffusivities derived from the CSAT3 anemometer of autumn and spring campaigns for the same periods mentioned in the above section. Arithmetic mean along with standard error of the emission rate values are compared in Table 5.2. Only those values were used to compare the emission rates where both $ER_{F^0_{eqn}}$ and Flux_p were available. The emission rate values were found to increase between 2.7% to 15.9% for subplots B, C and D. The maximum enhancement were observed for the subplot D of spring experiment. No effect of mitigation was observed for the experimental plots of autumn, however, a 2.7% decrease in the emission rate values of subplot B was observed in spring in comparison to subplot C but not significant with p-value < 0.05. Again, extra fertilizer was applied to subplot D but the emission rates were not higher than other plots, however, a 15.9% enhancement was noted. Overall, few changes were observed in the footprint corrected values of emission rates but no significant effect of mitigation was found.

Table 5.2: Mean measured flux and emission rate values of N_2O in $gN_2O\text{-}N.ha^{-1}.day^{-1}$ for the autumn (9 days) and spring (12 days) experiment after DCD application on subplots B and D. The results are compared with the control plot C. $Flux_p$ values are from the CSAT3 anemometer observations as mentioned in Section 5.3.3. Emission rates are estimated using F^0 from Equation 4.9 of Chapter 4. High mean values of autumn than spring experiment for this selected period has been discussed in Chapter 3.

Seasons	**N_2O flux $gN_2O\text{-}N.ha^{-1}$**		
	Plots	$ER_{F^0_{eqn}}$	$Flux_p$
Autumn	*B*	33.7 ± 7.22	32.6 ± 7.48
	C	31.4 ± 6.19	30.4 ± 6.41
	D	32.5 ± 9.17	31.7 ± 9.17
Spring	*B*	10.5 ± 1.87	10.2 ± 1.84
	C	10.8 ± 2.11	10.6 ± 2.11
	D	9.5 ± 1.38	8.2 ± 1.38

5.4 Discussion

The effect of grazing and mitigation on the N_2O emission rates were analyzed in this chapter. The N_2O flux values from a control subplot were compared for a pre and post-grazing period of the spring campaign, and a $\approx 90\%$ enhancement in the flux values was observed after grazing, irrespective of the source of the diffusivity coefficient. A gradual decreasing trend in the measured flux was observed after grazing in both seasons. The percentage increase in the N_2O flux values after grazing was found to be of the same order as mentioned in Saggar et al. (2004).

When the measured fluxes from the control subplots were compared with the DCD treated plots, no decrease in emission rate was observed for the treated plots during the autumn experiment. However, a 2.7% decrease in the emission rate values of subplot B was observed in spring in comparison to subplot C but not significant with p-value < 0.05. Extra fertilizer was applied to subplot D of spring experiment and a 15.9% enhancement was noted in the emission rates compared to measured fluxes, although, the mean emission rate was lower than other plots.

Therefore, findings from both autumn and spring experiments were contradictory to the already existing ideas of the effect of nitrification inhibitor over New Zealand's agricultural fields, which claims nearly 90% reduction in the emission rate of N_2O under the influence of DCD over urine patches (Di and Cameron, 2002b,a, 2003; Di et al., 2007; Qui et al., 2010). Now, such anomalous result of the autumn experiment can be explained by two possible reasons: (i) one could be the excessive rainfall event during 25-27 May 2010 when a total of 135 mm rainfall was observed within these 3 days, which was much higher than the seasonal normal. This might have washed away all the DCD; (ii) the other reason could be related to the nature of the soil which might

have had a lower nitrous oxide production rate (McMillan et al., 2012). For the spring campaign, DCD was applied 10 days after grazing. According to the standard procedure of DCD application over paddocks of New Zealand (Di and Cameron, 2003), DCD should have been applied within 7 days of grazing. However, partial reduction of the N_2O flux was still expected, but not observed within a statistically significant range.

As a consequence of the above observations, questions will certainly rise about the measurement precision and error of the paddock scale micrometerological system. A rigorous error analysis of the FG-EC system has already been performed and the mean error from sources such as diffusivity and concentration gradient measurement been identified. The mean total error in the flux values (R_{flux}^{mean}) from these sources was found to be 9.0% and 12% using the parameterization method for unstable and stable atmospheric conditions. Similarly, the maximum total error in the flux values (R_{flux}^{mean}) was found to be 35% and 49% for unstable and stable atmospheric conditions. The minimum resolvable concentration gradient ($\Delta C_{N_2O}^{min}$) was kept fixed at 0.049 ppb for the R_{flux}^{mean} estimation. Therefore, most of the error was contributed by the diffusivity parameter. Now, if it is assumed that the mean effect of mitigation on the nitrous oxide flux is $< 10\%$ for the given soil type, then given the mean error of our measurement of 9-12%, no effect of mitigation will be observed, irrespective of stability. However, only $\approx 0.3\%$ of the total error spectrum of R_{flux} was higher than 0.30 (30%) and, on average no effect of mitigation was observed. This implies that either there was no effect of mitigation for our site or the effect of mitigation was $< 10\%$. Again, when the emission rates derived from the footprint method were compared with the measured flux values, irrespective of seasons, marginally higher emission rates were observed indicating the fact that the measured flux is mostly reflecting the actual emission rate. Another possible explanation may include a theoretical verification of the FG-EC method itself as some recent studies have questioned the validity of the local scaling properties of atmospheric surface layer (McNaughton, 2004b, 2006). Under these circumstances, it can be concluded that the acceptability of this paddock scale micrometerological system can be improved by undertaking many more field measurement trials under different soil and meteorological conditions with rigorous flux foot-printing practices. Again from the theoretical perspective of turbulence, if some alternative turbulence models are found to be working well in the surface layer than the present Monin-Obukhov similarity theory based FG-EC model, then development and verification of a new flux gradient model can also be a future prospect.

Chapter 6

Analysis of the spectral properties of turbulence and some alternative scaling parameters

6.1 Preface

In the previous chapter, it was found that the FG-EC micrometeorological method was unable to detect any significant effect of mitigation on the N_2O emission rate and measured flux. Out of several different possibilities that were conjectured to be a reason for this failure, one important issue appeared to be the verification of the fundamental concept of Monin-Obukhov similarity theory itself. Such a proposal was made because of some recent findings of atmospheric surface layer turbulence scaling properties that were challenging the current standard model of turbulence. Therefore, in this chapter, atmospheric surface layer turbulence has been investigated in light of some newly proposed scaling properties.

6.2 Introduction

There are two general approaches for addressing turbulence energy in the convective boundary layer (CBL). First is the traditional approach based on statistical fluid mechanics (SFM) which involves the Reynolds-averaged-Navier-Stokes equation and a further development to Monin-Obukhov similarity theory (Monin and Obukhov, 1954). Second is the complex dynamical system (CDS) approach of turbulence following the initial work of Townsend (1956) and references given in McNaughton (2012). The

SFM approach leads to a local understanding of the boundary layer with classification of different layers, whereas in the CDS approach, flow processes are considered non-local and developed as emerging patterns of motions.

Now, according to the SFM approach, during day time, the atmospheric boundary layer (ABL) can roughly be divided in to a 'surface layer (SL)', a layer of 'local free convection (LFC)' and the 'mixed layer (ML)' or 'CBL above SL' (Holtslag and Nieuwstadt, 1986). The SL is the lowest part of atmosphere ($\approx 10\%$ of ABL) where flow structure is independent of the Coriolis force and dependent mostly on surface friction. Within the SL heat flux can be assumed constant with height (to within 10%). During a convective period, the CBL is dominated by the strong vertical temperature gradient and heat is transported within this layer through smaller coherent plumes which ultimately merge into a larger plume (Kaimal and Finnigan, 1994). The dynamics of these three layers, which has been conceptualized by Monin-Obukhov and Deardroff similarity theory (Monin and Obukhov, 1954; Deardroff, 1972), has been established by the field experiments of Kaimal et al. (1972) and Kaimal et al. (1976). Since then, the Monin-Obukhov (MO) and Deardroff model has become a standard model of SL and LFC turbulence.

Now, based on the standard model of turbulence, the height of transition from the surface level to the outer level can be represented by a MO similarity parameter $|L|$ which also signifies the transition from shear driven flow in the surface layer to buoyancy driven flow in the outer layer. Therefore, height of the surface layer is represented as $z < |L|$, where MO similarity theory seems to be valid. However, atmospheric observations were not always consistent from one report to the other as, Kader and Yaglom (1990) found no level where the temperature profile has zero gradient, and they did not identify height $|L|$ with any significant features of the profiles. Similarly, Smedman et al. (2007) noted a double-peaked spectra for temperature and heat flux of a slightly unstable boundary layer above the SFL, which lead to the hypothesis of existence of two different turbulence regimes in 'moderately unstable' and 'unstable very close to neutral' conditions. Furthermore, both turbulent regimes were found to be co-existent in an intermediate range of stability. Since there is no assurance that the data from various sources refer to the same turbulence regime (cellular convection, roll convection, near-neutral convection, etc.), lack of identification contributes to the confusion of the SFM approach of analyzing CBL turbulence.

Again following the SFM approach, the assumption of a sudden transition from a shear driven layer (SL layer) to a buoyancy driven layer (CBL above SL) is not

feasible. Therefore, the LFC is assumed to be present between the SL and the ML or CBL above SL (Holtslag and Nieuwstadt, 1986; Wyngaard, 1992; Garratt, 1992). This assumption of a LFC layer is found to be in harmony with the MO similarity theory as buoyancy is assumed to be dominating in this layer rather than the shear (Holtslag and Nieuwstadt, 1986) and therefore, the scaling properties from the outer layers do not interact with the SL turbulence, resulting in the SL turbulence being a function of only the local parameters. McNaughton (2004b) has raised questions about this model of SL turbulence by arguing that it is unlikely during a very highly convective period, when SL height is very low, as air plumes from the SL converge to form large updrafts as the scale gap is high. Furthermore, the temperature spectrum at a very low level is also found to be associated with the free convection.

Therefore, following these discrepancies of the SFM approach of addressing ABL turbulence, a new alternative model following the CDS approach and based on the Theodorsen ejection amplifier like (TEAL) structure has been proposed (McNaughton, 2004b,a, 2006; McNaughton et al., 2007; Laubach and McNaughton, 2009), abbreviated as the MNL model here after. In this new approach, turbulence is assumed to be a self-organizing, pattern forming system where a recurring pattern of coherent structures is assumed to be 'interacting eddies', where the smaller scale eddies and thermal structures combine to form the large eddies which in turn carry the small ones with them. Furthermore, the CDS approach assumes a 'surface friction layer' (SFL) rather than a SL near the ground, which unlike the definition of SL of the SFM approach, describes the types eddies present within this layer. Therefore, the SFL layer describes the scaling parameters for each class of eddies. Evidence of this new scaling model was provided in McNaughton et al. (2007) where the velocity spectra were assumed to be developing from the interaction of the outer eddies with the ground surface. Furthermore, when the peaks of the temperature spectra were collapsed in to a wavenumber (k) axis, a new length scale $z_i^{1/2} z^{1/2}$ was needed, where the upper limit of the CBL height during day time was represented by z_i. The requirement of this new parameter z_i contradicts directly with the MO similarity theory as it is not a local parameter and supports the argument of the nonlocal nature of turbulence flow processes.

However, as mentioned by McNaughton (2009), the MNL model is a nonlocal model and a profile measurement of atmospheric variables will be needed to verify the new approach. Therefore, as a first attempt, the McNaughton-Laubach scaling parameters (MLsp), such as TKE dissipation rate at CBL (ϵ_0), dissipation velocity (u_ϵ) and SFL height (z_s), of the MNL model are deduced from the profile values of

turbulent kinetic energy (TKE, b) and TKE dissipation rate (ϵ) for convective outer layers. The profile values of b and ϵ are derived using the wind profile observations from a SODAR and the parameterization scheme provided in Kramar and Kouznetsov (2002). The derived ϵ_0 values from the SODAR measurements are then compared with the parameterized ϵ_0 values. Similarly, SFL variables of the MNL model, i.e. z_s and u_ϵ, are compared with the existing SL parameters such as Obukhov length (L) and friction velocity ($u_\star$), respectively. Finally, the SFL spectra of the w-component of wind, temperature and heat flux cospectra are analyzed using these derived MLsp as a verification of this alternative scaling model.

6.3 Theory

In the following sections, a brief description of the MNL model is provided along with the parameterization schemes used for the computation of profile values of TKE and TKE dissipation rate. Since the MNL model assumes turbulence near ground is developed by the interaction between two types of eddies, namely inner and outer eddies, the MNL model described below is only focused on discussing the scaling parameters associated with these two types of eddies.

6.3.1 Inner and outer eddies and their interactions

According to Laubach and McNaughton (2009) "The inner eddies are attached eddies directly created by velocity shear near the ground, together with smaller eddies created by their break-up". Large, semi-permanent coherent eddies from above (which can be roll vortices or cellular structures) provide energy to the inner eddies (Figure 1 of McNaughton (2012)), and this process is associated with wind shear, although wind shear doesn't provide energy to the inner eddies. Inner eddies are associated with the transport of momentum within the SFL and attached inner eddies near the ground grow in a cyclic process and have the inner length scale of z. Finally, most of these eddies dissipate in the SFL and some are transported upward within the warm pools and dissipate at a greater height (McNaughton et al., 2007). However, no-one has yet confirmed the TEAL cascade mechanism in the SFL.

The outer eddies can be of two types. One is the coherent structures that are in the form of roll vortices or cellular in nature, and which can be extended up to the CBL. These outer eddies are aligned with the mean wind speed in the mid-CBL. However,

there is a problem with describing the alignment of long roll vortices in terms of the surface wind and shear stress because the helical rotation of rolls will cause the direction of the surface stress to vary $\pm 15^{\circ}$ or so with respect to the axial direction of the rolls from place to place, and if the rolls are semi-permanent this will carry over into the half-hour averages. This has caused confusion amongst turbulence experimentalists.

The second kind of outer eddies are those from the outer Richardson Cascade (Figure 1 of McNaughton (2012)). They are carried along within the larger structures, and when carried down into contact with the ground they form arrays of roll vortices aligned with the local stress at the ground. It is the blocking by the ground and the local stress that creates this form of the outer Richardson eddies which become attached.

The characteristic height of this large semi-permanent outer eddies are defined as z_i. Near the ground these large eddies can be detected from the spectra of the u and v components of the wind velocity, similar to one reported in Zhang et al. (2010), at small wave numbers where $kz_i \approx 1$. Now the energy dissipation rate in the CBL through these outer eddies is assumed as ϵ_0, which is usually constant above the SFL and represented by a single value (McNaughton et al., 2007), and from Kolmogorov law we know that the energy density of any eddy of particular size is $(\epsilon_0 k)^{2/3}$, where k is the wave number. The ϵ_0 can be estimated using a sonic anemometer above the SFL using a tall tower or by direct measurements, otherwise it can be estimated using the alternative method of the MNL model given as:

$$\epsilon_0 = \psi_0 g H_0 / T \tag{6.1}$$

Where, ψ_0 is the dimensionless dissipation factor with an empirical value of 1.1 (Laubach and McNaughton, 2009). H_0 is the buoyancy flux = $\overline{w'T_v'}$ and g is the gravitational acceleration. The inner eddies interact with the outer eddies at the top of the SFL and still remain attached. Therefore, the depth of the SFL, z_s, is assumed to be the height of the inner eddies, whereas the outer eddies can have a greater range of heights. z_s is also the averaged height where the inner eddies interact with the outer eddies and can be estimated using the parameterized form (Equation 7 of McNaughton et al. (2007)):

$$z_s = u_\epsilon^3 / (\kappa \epsilon_0) \tag{6.2}$$

Where κ is von Karmann's constant = 0.40 after Yaglom (1977) and u_ϵ is dissipa-

tion velocity in m s^{-1}. u_ϵ is related to friction velocity ($u_\star$) following $u_\epsilon \geq u_\star$. The u_ϵ can be estimated following Equation 13 of Laubach and McNaughton (2009) as:

$$u_\epsilon = (\kappa z \epsilon)^{1/3} \tag{6.3}$$

where z is the measurement height. One has to remember that Equation 6.3 will be satisfied only when $z/z_s \to 0$.

6.3.2 *Profiles of TKE and TKE dissipation rate*

Profiles of the TKE (b) and TKE dissipation rate (ϵ) can be estimated using a SODAR and fluctuations in the vertical wind component (σ_w) can be used for this purpose. A simple parametric relationship between b and ${\sigma_w}^2$ for part of the ABL, developed by Kouznetsov et al. (2004), shows that

$$b = 3.4{\sigma_w}^2 \tag{6.4}$$

where profile values of σ_w can be obtained directly from the SODAR measurements. The relative uncertainty of b estimated using this parameterization was found to be of same range of the measured ${\sigma_w}^2$. Now, b can be related to ϵ following Kramar and Kouznetsov (2002):

$$\epsilon = b(\partial U/\partial z)/C_{KP}^2 \tag{6.5}$$

Where U is the mean wind speed and C_{KP} is the Kolmogorov-Prandtl constant. In a further note, the vertical profile of the eddy viscosity (K_v) and Prandtl Scale (l_{PR}) can also be estimated following Kramar and Kouznetsov (2002):

$$\left.\begin{aligned} K_v &= b/(C_{KP}^2 \partial U/\partial z) \\ l_{PR} &= b^{1/2}/(C_{KP}^2 \partial U/\partial z) \end{aligned}\right\} \tag{6.6}$$

Where the C_{KP} values for the CBL were found to be 2.84 and 2.59, respectively, at 6 m and 56 m height, and for the neutral ABL C_{KP} values were found to be 2.09 and 2.12 (Kramar and Kouznetsov, 2002).

As mentioned in Kramar and Kouznetsov (2002) and Kouznetsov et al. (2004), one major drawback of this parameterization scheme is that these relationships (Equation 6.4 to 6.6) were developed by including only the shear term of the TKE budget equation and, therefore, these schemes are very much simplified and applicable to a near

neutral atmosphere. Furthermore, ϵ, K_v and l_{PR} largely depend on C_{KP} and not much information is available about C_{KP} for different atmospheric stabilities, except only the observations made by Kramar and Kouznetsov (2002). However, a comparison made by Fench (2004) of the profile values of ϵ obtained from a SODAR and using the parameterization schemes, showed good agreement with a LIDAR during near-neutral and stable atmospheres, but higher variations were observed during unstable periods. A possible scaling parameter was proposed by Fench (2004) to address this problem but untill now, as far as is known, it is not available. Therefore, no scaling is applied to the profile values of ϵ, K_v and l_{PR} in this study, but convective cases are investigated using the C_{KP} value of 2.59 (Kramar and Kouznetsov, 2002). For night time periods, a C_{KP} value of 3.04 is used.

6.4 Experimental site, instrumentation and data description

Data used in this study were originally collected in a field campaign of nitrous oxide flux measurement from an agricultural paddock of Canterbury. The field campaign took place in a commercial dairy farm, located south-west of Christchurch, near Methven, Canterbury, New Zealand. Figure 6.1 shows the field site with locations of the measurement masts. The field site was exactly the same as described in Chapter 3 but a different paddock was used. The yellow rectangle shows the external boundary of the field site. The width of the rectangular field is 1.3 km and length is 1.76 km. T-1 shows the location of a 10 m instrument mast in Figure 6.1. The N_2O gas measurement inlets are shown with white dots and denoted by T-2. Temperature and relative humidity sensors (Thermister CS-107 and Vaisala HMP-45 from Campbell Scientific Inc.) and cup anemometers were fitted at 2, 4, 6 and 8 m heights on the 10 m tower. The CSAT3 sonic anemometer (Campbell Scientific Inc., UT, USA) was fitted at 10 metre height. Sampling frequency for this sonic anemometer was 5 Hz. The SFAS acoustic SODAR (Scintec AG, Germany) was used for vertical profile measurement and its position is shown by the blue dot, T-3, in Figure 6.1. The SODAR was operational in between 14 Sept. 2011 18:30 to 27 Sept. 2011 10:15. However, observations for the period of 16 - 25 September were used for the spectral analysis. The SODAR data averaging period was set to 15 min and vertical profiles of u, v and w components of wind were measured continuously up to 500 m above the surface at 5 m resolution. Polyphonic sound pulses having frequency between 2525-4850 Hz were used for sampling. Approximately 175 m to the left of T-1 was a cow-milking shed and a shel-

ter belt was also present close to the northern end of the site. There was a tree-fence 455 m to the east of T-1 and it extended from north to south of the field. The entire experimental site was covered with short grass with canopy height varying between 0.1-0.2 m depending on grazing. However, the experimental paddock, shown with a red rectangle in Figure 6.1, was free of grazing during the measurement period.

Figure 6.1: Field layout of the spring 2011 campaign. T-1 is the approximate location of the 10 m tower shown with a red dot. The N_2O gas measurement inlets are shown with white dots and represented by T-2. T-3 shows the location of the SODAR. The yellow rectangle is the boundary of the extended field. The red rectangle shows the experimental paddock. The background field image was retrieved from Google Earth on 1 December, 2012.

Data from the 10 m tower were collected from 16 September 2011 at 0000 hrs to 27 September 2011 at 0930 hrs. However, observations for the period of 16 - 25 September were used for the spectral analysis. Wind component and temperature data from the sonic anemometer were corrected for the sonic orientation. Despiking of a variable, *var*, was carried out following Vickers and Mahrt (1997) by neglecting $var > 3.5\sigma_{var}$, where σ_{var} was standard deviation of the data. The 3D wind field of our data was trigonometrically rotated to force $\overline{w} = \overline{v} = 0$ (McMillen, 1988). Finally,

30 min averaged values were produced, and the SODAR data were processed using 'APRun v1.19' software from Scintec AG.

6.5 Results

6.5.1 Analysis of the profile measurements

Average wind speed profiles for the 'day time' and 'night time' observations are shown in Figure 6.2. 'Day time' was considered to be the period between 1000 hrs to 1600 hrs and observations from 16 - 25 September were used to produce Figure 6.2. 'Night time' was considered to be the period between 2000 hrs to 0400 hrs and 'Days' in the lower panel of Figure 6.2a indicates 'night times' of 16-17 September to 25-26 September. Since some of the upper air observations were missing, profile values were plotted up to 250 m height above the ground. The average wind speed during the convective period of 'day time' was found to vary between 5-12 m s^{-1} within the surface to 250 m level, except for 20, 22 and 23 September. The average wind speeds for these days were found to vary between 1-4 m s^{-1} within the CBL. Very high wind speed values ($>$7 m s^{-1}) were observed on 24th Sept. throughout the CBL and a passing frontal system from southwest caused 11.2 mm rainfall over our site on the same day. The average night time wind speed was less than the day time period, 1-5 m s^{-1}, and very little wind speed, 0.1-3 m s^{-1}, was observed throughout the nocturnal boundary layer of 20-21 and 22-23 Sept. The day and night time wind directions from the 10 m sonic measurements are shown in Figures 6.2(b) and 6.2(c), respectively. These figures are produced from the averages of wind speed and directions for the period mentioned above. One can see from Figures 6.2(b) and 6.2(c) that the day time surface winds were predominantly northerly, whereas, the night time winds were southerly. The average wind speed of the day time period was also higher than the night time.

Profiles of b and ϵ were estimated using the profile values of σ_w and following the parameterizations given in Equations 6.4, 6.5 and 6.6. Figures 6.3 a and b show the average vertical profiles of b and ϵ, respectively, for day and night time periods.

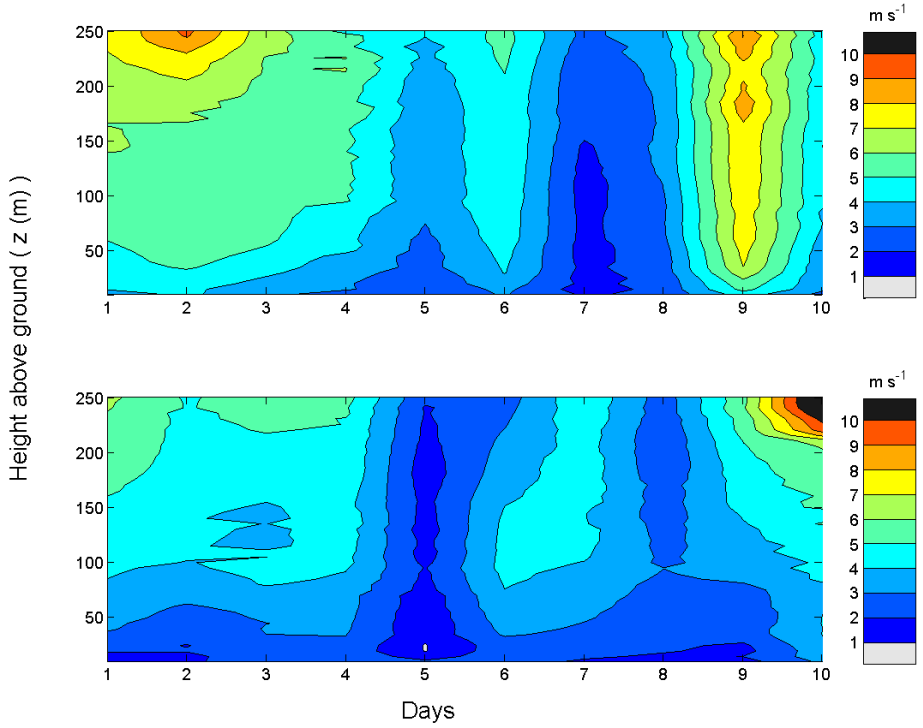

(a)

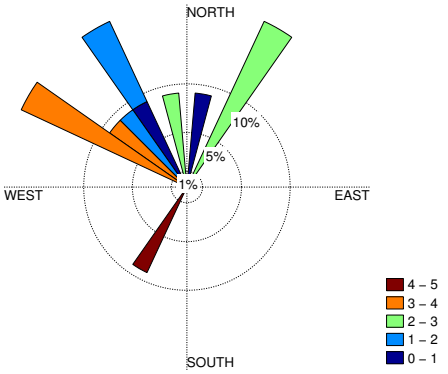

(b)

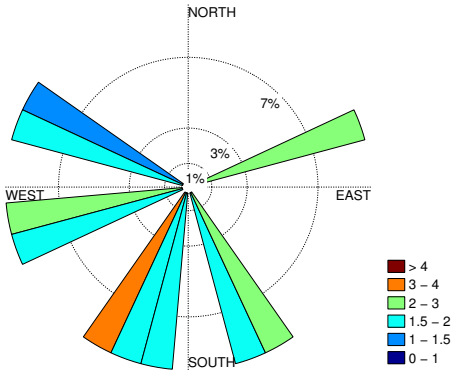

(c)

Figure 6.2: (a) Average wind speed (m s^{-1}) profiles from SODAR data are shown for day (upper panel) and night time (lower panel). Observations for the period of 16 to 25 Sept. are used to produce this diagram. Figures (b) and (c) show the wind direction for day and night time, respectively, obtained from the 10 m mast. Wind sectors (shown in different colours) are subdivided based on wind speed (m s^{-1}).

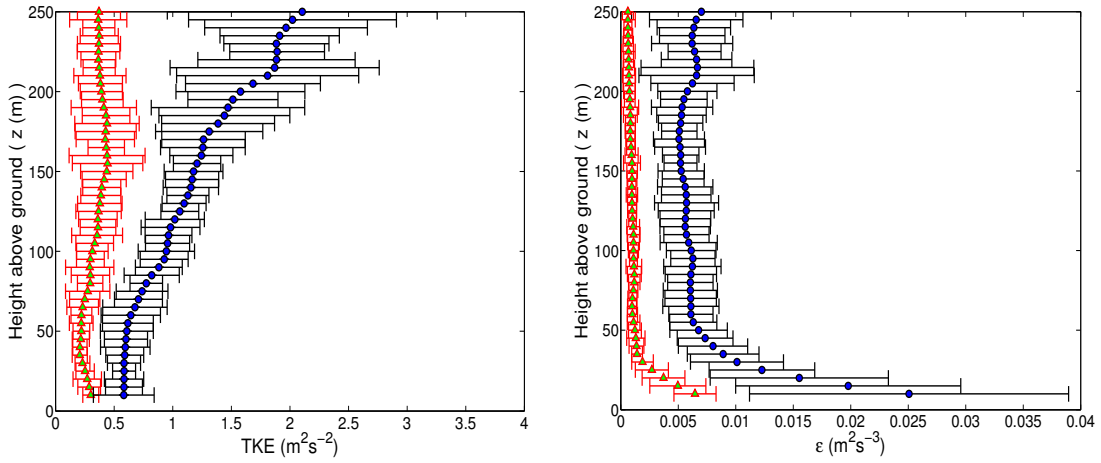

Figure 6.3: Observed averages of the profiles of (a) TKE (m^2 s^{-2}) and (b) TKE dissipation rate (m^2 s^{-3}) from SODAR data. The σ_w observations (obtained with a 15 min interval) from the SODAR are used with Equations 6.4 and 6.5 to compute TKE and TKE dissipation rate. The term 'average of averages' signifies the day-time averages of each day which are further averaged over 10 day period of the experiment. The green triangles and blue dots are for night and day time periods, respectively. The horizontal bars are showing the standard deviations.

6.5.2 MLsp from the 10 m mast

The sonic anemometer observations were further filtered by removing those values where $u_\star < 0.075$ m s^{-1} and $u_\star/U > 2.0$ following Laubach (2010). Therefore, conditions of extremely stable and unstable surface layer with high $u_\star$ values were removed. Next, to choose only the day time convective periods, additional filtration was carried out by removing those runs where the heat flux (H), $H < 20$ W m^{-2} (Laubach and McNaughton, 2009). Therefore, all the filtered cases were observed for the day time convective periods and three cases of very deep convection, $1/L < -1.0$, were also observed. Similarly, most of the $u_\star$ values (80.3%) were found to vary between 0.1-0.4 m s^{-1} with maximum frequency at 0.255 m s^{-1}.

6.5.2.1 Estimation of TKE dissipation rate in the CBL

TKE dissipation rate in the CBL (ϵ_0) values were estimated using the parameterization method (ϵ_0^{param}) of Equation 6.1 and observations from the SODAR, including Equation 6.5 (ϵ_0^{sodar}). The buoyancy flux parameter, H_0, was estimated using the sonic temperature and the w component of wind. Minor differences between the sonic temperature and the virtual temperature were neglected.

The ϵ_0^{sodar} values were estimated based on the assumption that ϵ_0 remains almost constant in the upper level. Therefore, ϵ_0^{sodar} values were assumed to be the mean of all values in the 50 - 500 m layers. However, cases with unsmooth variation in the profiles of ϵ_0, and missing data above the 350 m level were observed frequently and were neglected. When these ϵ_0^{sodar} values were compared with the ϵ_0^{param} values, few cases were found where $\epsilon_0^{param} > 5\epsilon_0^{sodar}$ and these cases were also neglected. Finally, a correlation coefficient of 0.72 was observed between these two estimations at the 99% confidence level where the lower and upper envelopes for the point cloud have slopes of 0.5 and 2.0, which is also a spread similar to the uncertainty of ψ_0 of Equation 6.1 estimated by Laubach and McNaughton (2009) from the literature data. When a one to one comparison was made between these two filtered ϵ_0 parameters, the SODAR values were found to be on average 1.10 times higher than the parameterized values (Figure 6.4(a)).

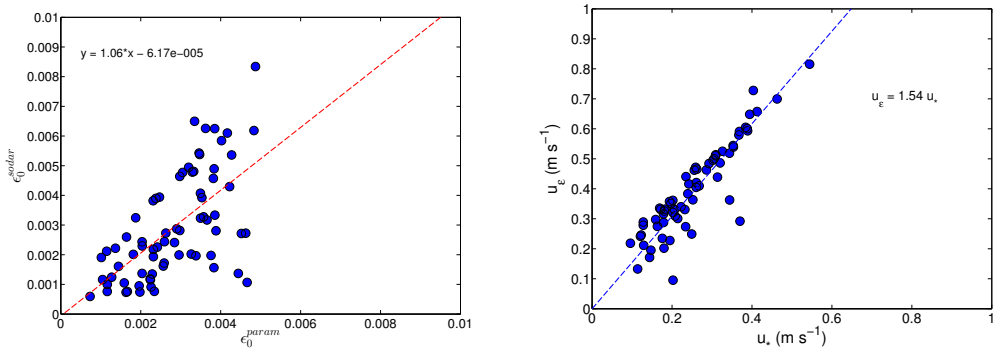

(a) (b)

Figure 6.4: (a) Comparison of ϵ_0 values ($m^2 s^{-3}$) from the parameterization method (x-axis) and observations from SODAR (y-axis). ϵ_0^{param} is obtained from the sonic anemometer observations and using Equation 6.1. ϵ_0^{sodar} is obtained using σ_w from SODAR measurements and using Equation 6.5. The linear fit is shown with a red line. The y and x variables in the equation are the y and x axis parameters. (b) Comparison of u_ϵ (m s^{-1}) with $u_\star$ (m s^{-1}) values. u_ϵ is obtained using Equation 6.3. The blue dotted line is the linear fit through origin.

6.5.2.2 Estimation of SFL height and dissipation velocity

The SFL heights (z_s) were estimated from the filtered sonic anemometer observations (z_s^{sonic}). Using Equation 6.2 and a total of 62 filtered cases of ϵ and ϵ_0^{sonic}, values of z_s^{sonic} were computed. The z/z_s^{sonic} of the 10 m tower observations were found to range between $0.018 \leq z/z_s^{sonic} \leq 0.86$ with a median value of 0.18. These z/z_s^{sonic} values were used in the MNL model as the basis of the new impinging eddy model as the

turbulent spectra were analyzed based on the categorization of z/z_s^{sonic}. In this study, the categorization of the z/z_s^{sonic} values was made following a similar classification of Laubach and McNaughton (2009) as: Class A: $z/z_s^{sonic} > 0.5$; Class B: $0.22 \leq z/z_s^{sonic} \leq 0.5$; Class C: $0.14 \leq z/z_s^{sonic} \leq 0.22$; Class D: $0.09 \leq z/z_s^{sonic} \leq 0.14$ and Class E $z/z_s^{sonic} < 0.09$.

Since the MNL model of turbulence assumed that $z/L \approx z/z_s$, a comparison of z/L with z/z_s is necessary. If ϵ_0 is parameterized (Equation 1), then the relationship between -L and z_s is $-z_s/L = (u_\epsilon/u_\star)^3\psi_0^{-1}$ (Equation 6 of Laubach and McNaughton (2009)), so for the majority of our runs, which have $u_\epsilon/u_\star \approx 1.54$, it follows that $z/z_s \approx$ -0.27 z/L, or a factor of 2 stemming from the variability of ψ_0. In practice, a linear relationship of $z/z_s^{sonic} = 0.10(-z/L)$ was observed for our data which modified to $z/z_s^{sonic} = 0.23(-z/L)$ when 4 cases of very high $|z/L|$ values ($|z/L > 5.0|$) were ignored. Again, a relationship of z/z_s^{sonic} = -0.73z/L was observed when $-z/L < 0.2$, which fits very well with the previous proposition.

Next, the dissipation velocities (u_ϵ) were computed for each categorization using Equation 6.3 and compared with the friction velocities ($u_\star$) (Figure 6.4(b)). The relationship between u_ϵ and $u_\star$ was found to be very close ($u_\epsilon/u_\star$ = 1.54) to the one provided in Laubach and McNaughton (2009) ($u_\epsilon/u_\star$ = 1.2). Consistently higher mean values of u_ϵ were observed than the mean $u_\star$ values of each class of z/z_s^{sonic} and the maximum difference between u_ϵ and $u_\star$ was found to be 0.25 m s^{-1} for class E.

6.5.2.3 Estimation of CBL depth

There were no direct measurements of the CBL depth (z_i) as a considerable amount of data were missing from the SODAR above 250 m from the surface and the vertical data limit of the SODAR was restricted to 500 m. Therefore, z_i was estimated using the maximum frequency of the horizontal wind component spectrum with mean wind speed following Kaimal and Finnigan (1994), $z_i = U/(1.5f_{max})$. The f_{max} was estimated from the averages of the first six highest values. Mean values of z_i were computed for each class of z/z_s^{sonic} and are provided in Table 6.1. As described in Laubach and McNaughton (2009), this parameterization method of estimating the CBL height can have some ambiguities and therefore, precautionary measures should be taken. To ascertain the acceptability of parameterized z_i values, planetary boundary layer heights (PBL) obtained from the WRF model (Weather Research and Forecasting model v3.1, NCAR-NCEP, USA) simulated values for each class of the data, described in Table 6.1, were compared with the corresponding z_i values (Figure 6.5). It should be kept

in mind that theoretically the PBL height from WRF is approximately equal to z_i during the convective period, but in practice values may differ substantially. Details of the WRF modeling setup is not provided here, although, it should be noted that the PBL heights were obtained using the Mellor-Yamada Nakanishi and Niino 2.5 level PBL scheme (Nakanishi and Niino, 2004) as this scheme can reduce common biases produced in the Mellor-Yamada-Janjic scheme (Olson and Brown, 2009). When the z_i values were compared with the PBL values, a linear relationship of PBL = $0.86z_i$ was observed with a total of 11 such cases where $z_i > 5$PBL heights.

Table 6.1: Description of the MLsp obtained according to the surface layer classification of 6.5.2.2. The standard deviations are provided in parenthesis.

Class	No. of samples	z_s^{sonic} (m)	z_i (m)	z_i/z_s	$u_\star$ (m s^{-1})	u_ϵ (m s^{-1})
A	7	15.6 (3.0)	213 (114)	13.0	0.19 (0.04)	0.27 (0.06)
B	19	32.8 (7.6)	298 (110)	9.3	0.29 (0.05)	0.32 (0.06)
C	10	56.9 (8.4)	327 (131)	5.7	0.25 (0.08)	0.38 (0.10)
D	10	87.5 (8.6)	470 (134)	5.1	0.29 (0.09)	0.46 (0.11)
E	16	209.4 (129.7)	585 (137)	2.1	0.36 (0.08)	0.57 (0.11)

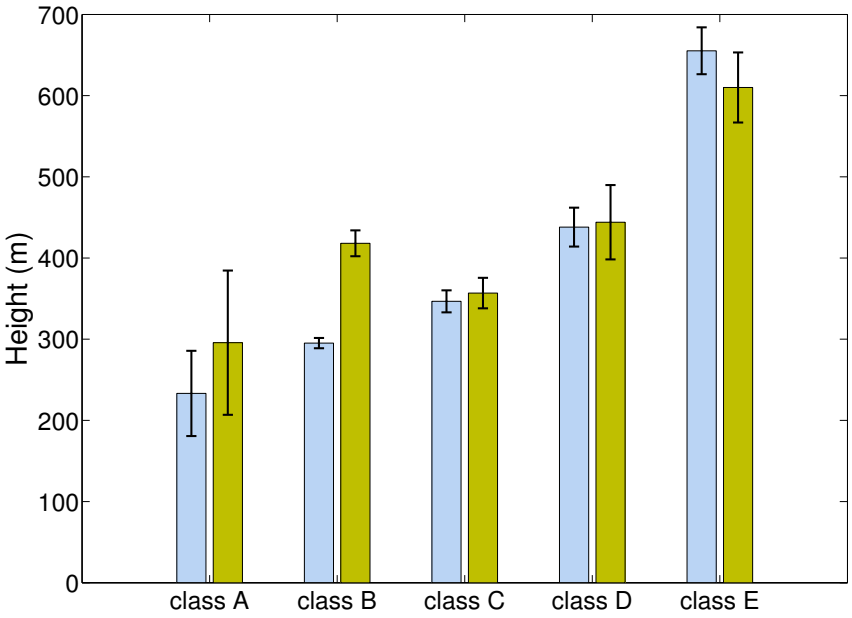

Figure 6.5: Comparison of the CBL depths (z_i) with the PBL heights obtained for each class of data described in Table 6.1. The mean z_i values with normalized standard deviations are shown by blue bars, whereas, the mean PBL heights with normalized standard deviations are shown by green bars.

6.5.3 Spectra from the 10 m mast

In the following sections, spectral analysis of the w-component of wind, temperature and heat flux has been carried out based on each class of data mentioned in Table 6.1, except for Class E as considerably higher random error has been noticed for this class. A linear de-trending and a 10% bell tapering was performed over individual data to remove the red-noise and to prohibit leakage, following Stull (1988). The power spectral density produced in this study were obtained using the p-Welch method (Welch, 1967) where each data sample was divided into eight segments with 50% overlapping and the frequency response was estimated from the average of these segments. A similar method was used in Katurji et al. (2011). The frequencies were then converted to wavenumbers (k) following: $k = 2\pi f/U$ where f is frequency, k is wavenumber and U is the mean wind speed (m s^{-1}) as described in Equation 6.5. The spectrum for each selected run of each class was produced and then averaged for each z/z_s class.

6.5.3.1 w - wind component spectra

The MNL model predicts that for the lower part of the CBL the z_i scale outer eddies will be blocked by the ground and therefore, z_i will be irrelevant to the analysis of the w-spectra, rather eddies with a height of $2z$ will contribute more to the w-spectra. Therefore, z should be used as the principal scaling parameter during the spectral analysis of the w-component of wind. Thus, instead of using z_i to scale the spectra, z was used to collapse the w-spectra of our data using the scaling parameter $(\epsilon_0 z)^{-2/3}$. If a satisfactory collapse of the w-spectra is obtained with this scaling then the new velocity scale would imply that the transitions between the surface friction layer and the outer layer are governed by the flow in the entire CBL (McNaughton et al., 2007). The spectra obtained with this normalization was found to fit the -2/3 slope well in the inertial subrange for all classes (Figure 6.6(a)), except for a little deviation for class D. The average spectral peak was found to be kz = 0.91 with standard deviation of 0.08; correspondingly, the average spectral wavelength ($\lambda_m = 2\pi/k$) for the highest contributing eddy was found to be 6.98. This value is close to $\lambda_m = 6z$ of Kaimal et al. (1972, 1976), although, $\lambda_m = 9z$ was obtained by McNaughton et al. (2007). Again, the energy of each class of eddy was found to reduce gradually for class A to D and became 2.7 times less for class D than class A. Altogether, the spectral properties for this scaling were found to support the MNL model well.

McNaughton et al. (2007) has explained that the spectra of the w-component at smaller wavenumber will reflect the energy of large eddies spanning up to the top of CBL, and therefore, should be scaled with z_i and z/z_i. The exponential relationship of $(z_i\epsilon_0)^{-2/3}(z/z_i)^{-4/3}$ was derived without any prior knowledge and found to collapse the spectra well. However, in this case, $(z/z_i)^{-5/3}$ was found to collapse the data well for wavenumbers less than 10. This was found to be a 24.8% enhancement from the values of $(z/z_i)^{-4/3}$. As mentioned by Laubach and McNaughton (2009), this percent enhancement in the exponential term of z/z_i is well within the error range of z_i as it can have a possible maximum uncertainty of 30%.

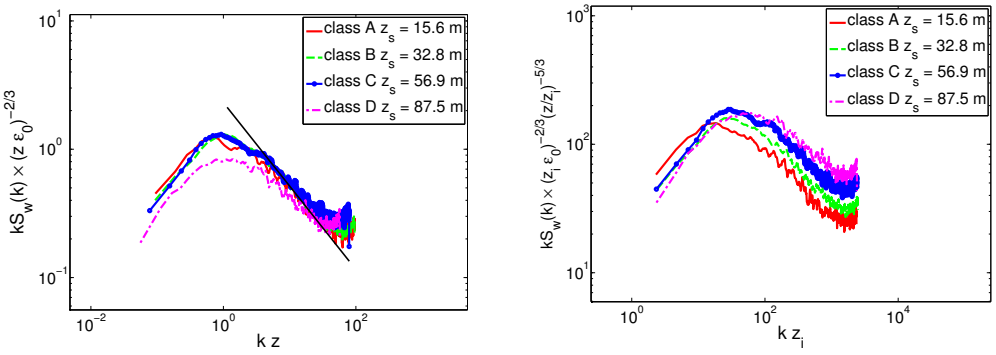

(a) (b)

Figure 6.6: The normalized vertical velocity spectra multiplied with respect to (a) $(\epsilon_0 z)^{-2/3}$ and (b) $(\epsilon_0 z_i)^{-2/3} \times (z/z_i)^{-5/3}$. The velocity scale $(\epsilon z)^{-2/3}$ of (a) has been obtained from the MNL model and found to represent the slope of -2/3 of inertial subrange well and collapses well near the peak. The velocity scale of $(\epsilon_0 z_i)^{-2/3} \times (z/z_i)^{-5/3}$ is also obtained with the MNL model with marginal modification.

6.5.3.2 Temperature spectra

When the temperature spectra were investigated by McNaughton et al. (2007), they found that an intermediate scaling of wavenumber axis with $z_i^{\alpha} z^{1-\alpha}$ performs better in collapsing the peak of the spectra than the individual scaling parameter z or z_i. The α was found to be equal to 0.50 for an optimum collapse. Introduction of this new mixed length scale was conjectured to be, as quoted from McNaughton et al. (2007), ".. though the eddies that carry the individual plumes have lengths proportional to z, the spectra reflect both these individual plumes and their coalescence into larger plumes in the flow. The coalescence must depend on z_i/z." This would again reaffirm the notion that the CBL is acting as a self organizing system where both local and large

scale controls are responsible for transporting heat to the larger part of the CBL. In a similar approach, Laubach and McNaughton (2009) analyzed the temperature spectra for SFL and a mixed length scale of $(z_i z_s)^{1/2}$ was found for the orderly collapse of temperature spectra on the wavenumber axis within SFL. Therefore, instead of producing the pre-multiplied spectra with traditional parameters like ϕ_ϵ or $T_\star$, the z_i and z were used to collapse the T-spectra for wavenumber. In two different cases, the T-spectra were produced by multiplying with (a) $(z\epsilon_0)^{2/3}H_0^{-2}$ and (b) $(zz_s)^{1/3}\epsilon_0^{2/3}H_0^{-2}$ on the amplitude axis and (a) $(z_i z)^{1/2}$ and (b) $(z_i z_s)^{1/2}$ on the wavenumber axis, as shown in Figure 6.7(a) and 6.7(b), respectively.

These spectra were found to approach the peak as z/z_s cases were increasing (Figure 6.7(a)) and this trend was predominant up to $k(z_i z)^{1/2}$ = 4.5. Again, 4.5 was where the spectral peak was found by Laubach and McNaughton (2009) for the same case (dashed line of Figure 6.7(a)). However, in this case the peak was obtained at a $k(z_i z)^{1/2}$ = 2.9 (bold line of Figure 6.7(a)) and the gradual increasing trend of different classes of z/z_s became fuzzy after $k(z_i z)^{1/2}$ = 4.5. The percent deviation of the average spectral peak from the Laubach and McNaughton (2009) model was 39.5%. Now, when the scaled amplitudes were explored for case (a) scaling, it was observed that except for class D, which had a peak amplitude of 0.88, scaled amplitudes of all other classes were significantly higher (1.56, 1.40, 1.56 for class A, B and C, respectively) than the reported values of 0.7 of the MNL model. For case (b) scaling, the average spectral peak on the $k(z_i z_s)^{1/2}$ axis was found to be 5.7 $\pm$ 1.3 (bold line of Figure 6.7(b)) compared to 4.5 $\pm$ 1.5 (dashed line of Figure 6.7(b)) of Laubach and McNaughton (2009) which was a good match. However, similar to case (a), the average spectral energies were found to be significantly higher ($(zz_s)^{1/3}\epsilon_0^{2/3}H_0^{-2}$ = 1.95 $\pm$ 0.18) than the mean value obtained by Laubach and McNaughton (2009).

Now, when these spectral characteristics were analyzed in comparison to the standard spectral model of Kaimal et al. (1972, 1976), one can see that peak locations of the temperature spectra can indeed be located on the wavenumber axis when the mixed length scales of the MNL model are used, which describes the organization and interaction of z_s scale eddies to the z_i scale eddies spanning up to the CBL top. However, the systematic increase in amplitude of decreasing the z/z_s class for the $k(z_i z_s)^{1/2} > 30$ range was not certain in this analysis (Figure 6.7(b)) as found in Figure 7 of Laubach and McNaughton (2009).

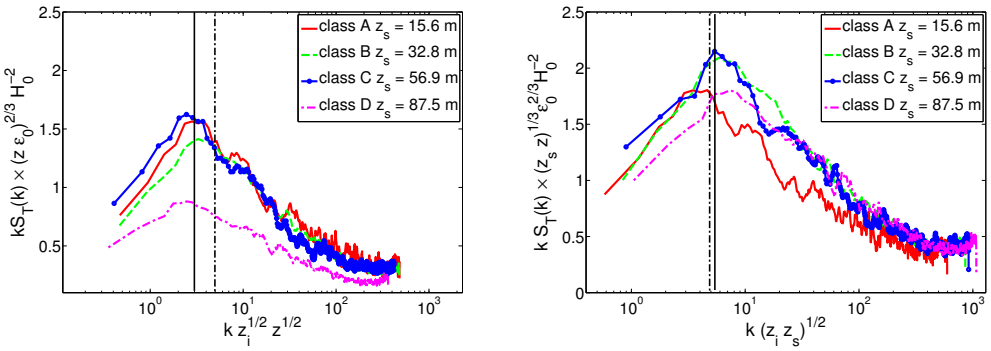

Figure 6.7: The normalized temperature spectra multiplied with respect to (a) $(\epsilon_0 z)^{2/3} \times H_0^{-2}$ and (b) $\epsilon_0^{2/3}(z_s z)^{1/3} \times H_0^{-2}$. The vertical dashed lines of (a) and (b) are obtained from the MNL model. The bold vertical lines of (a) and (b) are the spectral averages.

6.5.3.3 Heat flux co-spectra

Similar to temperature spectra, the heat flux cospectra were explored for two different cases of scaling described in Laubach and McNaughton (2009) as: case (a) the wavenumber axis was multiplied by $(z_i z_s)^{1/2}$ and; case (b) the wavenumber axis was multiplied by $(z_i z_s)^{1/4} z^{1/2}$. In both cases, the amplitude axis was multiplied by H_0^{-1}. As mentioned by Laubach and McNaughton (2009), since there was no alternative scaling of the ordinate of the heat flux cospectra at the ground, no unanimous peak was observed for both cases. Again verification of case (a) scaling would ascertain the conjecture that the length of flux carrying structures is the same as that of the temperature structures. Similarly, the existence of the doubly-mixed scaling parameter was assumed to explain the heat transport through embedded eddies of z scale within z_s scale within z_i scale eddies. Therefore, verification of the doubly mixed length scale would satisfy the proposition of 'top-down organization of bottom-up heat flux'. Now, one can see from the case (a) spectra (Figure 6.8(a)) that the peak wavenumber of the scaled spectra is increasing as z/z_s changes from A to D. A similar trend was also observed in the Aorangi data by Laubach and McNaughton (2009). However, an extra peak near to the first dominant wavenumber peak of class A turbulence was observed for this data which was not observed in Figure 11 of Laubach and McNaughton (2009).

The wavenumber scaling parameter $(z_i z_s)^{1/4} z^{1/2}$ was introduced by Laubach and McNaughton (2009) to collapse the large wavenumber regions of the T-spectra and heat-flux co-spectra. A good collapse was reported for both of their data sets and a peak was found at approximately 1.2 ($\pm$0.3). The average peak wavenumber for our

data was found to be 5.6 ($\pm$ 1.3).

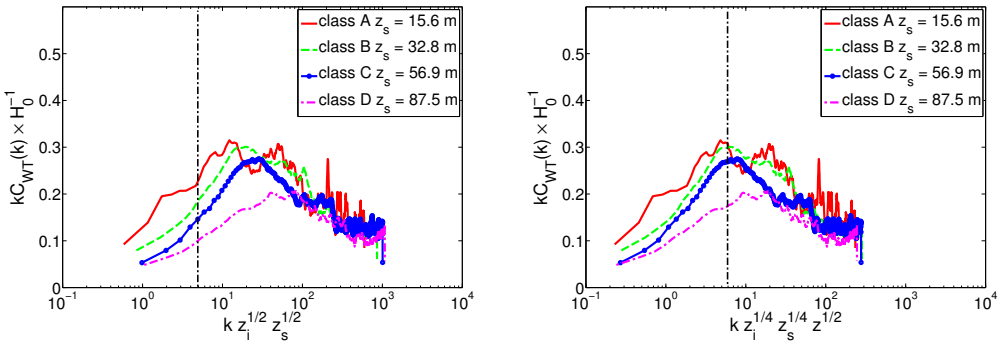

(a) (b)

Figure 6.8: The normalized heatflux co-spectra multiplied with respect to (a) H_0^{-1} and plotted against $z_i^{1/2} z_s^{1/2}$; (b) H_0^{-1} and plotted against $z_i^{1/4} z_s^{1/4} z^{1/2}$. The vertical line of 6.8(a) shows the peak location of the T spectrum from McNaughton et al. (2007), whereas, the vertical line of 6.8(b) shows the average peak location of all the classes at a normalized wavenumber 5.6.

6.6 Summary and conclusion

The objective of this research was to verify an alternative turbulence model of the convective boundary layer developed by Laubach and McNaughton (2009) with previous results from McNaughton (2004a,b, 2006) and McNaughton et al. (2007). This new model, abbreviated as the MNL model, was developed on the basis of a chaotic dynamical system approach rather than the traditional statistical fluid mechanics approach. Hence, some new nonlocal scaling parameters (such as z_s, u_ϵ, ϵ_0, etc.) were used to collapse the wind, temperature and heat flux spectra particularly at the wavenumbr axis. However, direct measurements of some of these nonlocal scaling parameters have never been used before, which were needed to verify this new model. Therefore in this study, vertical profile measurements of the atmosphere along with the parameterization schemes provided by Kramar and Kouznetsov (2002) were used to derive some of these nonlocal parameters, which in turn were used to verify the MNL model. A brief description of results obtained from this verification study is as follows:

- When the TKE dissipation rate in the CBL obtained from SODAR measurements (ϵ_0^{sodar}) were compared with the values obtained from the sonic anemometer (ϵ_0^{param}), a correlation coefficient of 0.72 was observed (p-value < 0.001) within

the prescribed upper and lower uncertainty range of 2 and 0.5 of ψ_0 of Laubach and McNaughton (2009).

- Similarly, when the u_ϵ values were compared with the observed $u_\star$ data, a linear relationship of $u_\epsilon = 1.54u_\star$ was found for our data which compared well with the values of $u_\epsilon = 1.2u_\star$ of Laubach and McNaughton (2009).

- From the spectra of the w-component of wind (Figure 6.6), it was observed that classes A, B and C collapsed well in Figure 6a under the new scaling parameters, but class D was slightly different. However, the average spectral peak was found to be kz = 0.91 with a standard deviation of 0.08, and the average spectral wavelength for the highest contributing eddy was found to be λ_m = 6.98 in comparison to λ_m = 6.0 of Kaimal et al. (1972, 1976). From Figure 6b, it was also found that the MNL model scaling parameter ${z/z_i}^{-4/3}$ works well in collapsing a smaller wavenumber region within an uncertainty range of 30%.

- From the spectra of temperature for different z/z_s classes using the MNL model parameters $(zz_i)^{1/2}$ and $(z_iz_s)^{1/2}$ (Figure 6.7 a and b, respectively), it was found that the conjecture of ".. though the eddies that carry the individual plumes have lengths proportional to z, the spectra reflect both these individual plumes and their coalescence into larger plumes in the flow. The coealescence must depend on z_i/z .." (quoted from McNaughton et al. (2007), pp 266.) of the MNL model holds true as a gradual increasing trend in energy for each z/z_s class was observed (Figure 6.7a). Furthermore, within the SFL when z was replaced by z_s to represent interactions between the z_i and z_s scale eddies, peaks of classes A to C collapsed well. However, the spectral energies were found to be significantly higher which may be caused by the 'p-Welch method' of data partition and spectral energy estimation.

- Similarly, when the heat flux co-spectra were analyzed using the MNL model parameters $(z_iz_s)^{1/2}$ and $(z_iz_s)^{1/4}z^{1/2}$ (Figure 6.8 a and b, respectively), the spectral peaks were found to collapse well for Figure 6.8a. However, for the scaling parameter $(z_iz_s)^{1/4}z^{1/2}$, the peak of spectral collapse was found to be approximately around 5.6 ($\pm$1.3) in contrast to 1.2 ($\pm$0.3) of the MNL model.

We found that the new scaling parameters described by the MNL model work well within the CBL. The parameterization schemes provided by Laubach and McNaughton (2009) to derive some nonlocal parameters, which are essential to this model, were also

found to work well within a predefined error range. This implies that this new model of explaining CBL turbulence using a chaotic dynamical system approach has a more acceptable fundamental framework than the traditional statistical fluid mechanical approach, and therefore, this new model should be used widely. However, it is to be noted that the formulas provided by Kramar and Kouznetsov (2002) and used in this study need further rigorous validation for convective periods. The selected few cases, where ϵ_0^{param} matched well with the ϵ_0^{sodar} data, may not necessarily reflect a good agreement for wide range of atmospheric observations. Again, as described in bullet three of this summary, the high amplitude values of temperature spectra should be investigated thoroughly in a future study.

Chapter 7

Summary, discussion and future work

A micrometeorological approach to pastoral N_2O flux estimation was verified in this thesis for agricultural paddocks of New Zealand. Two separate field experiments were carried out in a commercial agricultural field near Methven during autumn and spring of 2010. N_2O fluxes were measured from some control and experimental plots using a Monin-Obukhov similarity theory based combined flux gradient - eddy covariance (FG-EC) method. This central idea of verification of a FG-EC measurement system for N_2O flux estimation involved several subsequent qualitative and quantitative analyses to provide a comprehensive assessment of this procedure. These analyses addressed the following important questions:

- How does random error accumulate in the final measured flux value through turbulent eddy diffusivity and what would be the probabilistic nature of the accumulated error?
- If fluxes were measured continuously from some control and treated plots, how do we know the exact contribution of a particular plot to the measured flux? Is it possible to develop a new method to address this problem?
- Does this proposed method has the efficacy to distinguish the effect of animal grazing and mitigation on the measured flux? If not, then why and what can be done to improve the efficacy?

As an extension of the last question, an alternative turbulence model was verified to address the question whether the Monin-Obukhov similarity parameters are particularly effective for modeling the atmospheric surface layer turbulence properties. A brief summary of findings is given below.

- **Verification of the N_2O flux values:**

  - Flux values estimated by the thermal method (where eddy diffusivity k_h^t was used to compute flux) were found to be higher than the parameterization technique (where diffusion velocity d_h^p was used to compute flux) on average. Irrespective of two different flux computation methods (parameterized and thermal) from two sensors and seasons, the mean flux of control plots varied between 7 - 26 $gN_2O\text{-}N.ha^{-1}.day^{-1}$. The maximum flux values from the control plots were found to be 191.9 and 491.8 $gN_2O\text{-}N.ha^{-1}.day^{-1}$ for the autumn and spring period, respectively, and compared well with the values of Di et al. (2007) and Di and Cameron (2003). Similarly, the daily mean flux values were found to be 10.9 $\pm$ 0.98 and 11.7 $\pm$ 0.57 $gN_2O\text{-}N.ha^{-1}.day^{-1}$ for the autumn and spring seasons, respectively. Statistically significant (p-value < 0.01) differences in the flux values between the parameterized and thermal methods (6.8 and 17.9 $gN_2O\text{-}N.ha^{-1}.day^{-1}$) were observed for low wind speed conditions ($u_\star < 0.2$ m s^{-1}) and during very unstable atmospheric surface layer conditions ($1/L <$ -0.1), respectively. Overall, the measured flux values from the control plots compared well with the daily mean and maximum measured fluxes of already published values of Saggar et al. (2004) and Luo et al. (2008a).

- **Error propagation in the measured flux and probabilistic estimates:**

  - Some new mathematical relationships were derived between the transfer coefficients (k_h^t and d_h^p) and the atmospheric surface layer variables and a Monte-Carlo type analysis was performed to explore the probabilistic nature of the error propagation. From the Monte-Carlo analysis, the maximum relative error in the thermal transfer coefficient was found to be up to 80%, irrespective of the nature of stability which reduces to the order of 15% when $|\Delta T| > 0.01$ and $|\overline{w'T'}| > 0.001$ cases were considered. For the parameterized transfer coefficients, the maximum error was found to be as high as 49% and 35% for stable and unstable atmospheres, whereas an ensemble mean value of 9% and 7% error was observed, respectively, for stable and unstable cases. The relative error in $u_\star$ was found to contribute more to the total relative error of the parameterized transfer coefficients

than L, irrespective of stability. Unimodalities were observed in the relative error distribution of k_h^t and d_h^p of the unstable case ($1/L < 0$), whereas a partial bimodality was observed in the error distribution of the stable d_h^p values ($1/L \geq 0$). The relative error estimate in the N_2O concentration was found to be 0.08 and 0.06 for stable and unstable atmospheres, respectively. Total mean relative error in the measured flux values was found to be of the order of 9% and 12% for unstable and stable atmospheres using transfer coefficients from the parameterization method and 16.5% for transfer coefficients of the thermal method.

- **Identification of source area and estimation of emission rate from a multi-plot flux measurement system:**

  - A new footprint method was developed using an inverse footprint fraction approach to estimate emission rate from a particular field. An analytical solution of the background flux (F^0) has also been provided. Emission rates obtained from the proposed method were found to be on average 2.1% higher than the measured flux values for the control plots, with a realistic mean value of F^0 = 6.77 $gN_2O\text{-}N.ha^{-1}.day^{-1}$ as the range of F^0 was found to vary between $0 \leq F^0 \leq 15.0$ $gN_2O\text{-}N.ha^{-1}.day^{-1}$. An average of 4.3% of the measured fluxes was found to be contributed by source areas outside of the field domain, which attained a maximum of 30% in one occasion. Correlation coefficients of 0.58 and 0.66 between the analytical and the bLs model footprint fraction (p-value < 0.001) affirms the realistic nature of the analytical model. The correlation coefficients were found to increase by 10% when only the near neutral cases were considered. When the emission rates obtained from this new approach were compared with the bLs simulated emission rates of a control plot, it was found that the proposed method worked well when the atmospheric stability $|1/L| \leq 0.2$. The mean random error or uncertainty in the measured flux values, which included footprint heterogeneity error and random measurement error, was found to be of the order of 16.53% for those fluxes which were computed using d_h^p as a transfer coefficient.

- **Effect of grazing and mitigation on the measured flux**

  - It was found that the FG-EC method worked well to distinguish the effect

of grazing in the measured N_2O flux values as an approximately 90% enhancement in the post grazing period was observed. This value was in good agreement with values computed by Saggar et al. (2004) using chambers. On the other hand, when the effect of DCD on N_2O flux was investigated, no significant difference in the measured fluxes was observed between the treated and control plots. A 2.7% reduction in the N_2O emission rate was observed for subplot B compared to subplot C of spring experiment after footprint correction, but was not significant with p-value < 0.05. Extra fertilizer was applied to subplot D of spring experiment and a 15.9% enhancement was noted in the emission rates compared to measured fluxes, although, the mean emission rate was lower than other plots.

- **Investigation of a new CBL turbulence model**

  - The new turbulence model of Laubach and McNaughton (2009) following McNaughton (2004a,b) and McNaughton et al. (2007) was investigated for the convective atmosphere. Instead of using the traditional local parameters of atmosphere (such as $u_\star$, L, etc.), some nonlocal parameters (such as ϵ_0, u_ϵ, z_s, etc.) were used to scale the spectra along the wavenumber axis. When the TKE dissipation rate in the CBL obtained from SODAR neasurements (ϵ_0^{sodar}) were compared with the values obtained from the sonic anemometer (ϵ_0^{param}), a correlation coefficient of 0.72 was observed (p-value < 0.001). Similarly, when the u_ϵ values were compared with the observed $u_\star$ data, a linear relationship of $u_\epsilon = 1.54u_\star$ was found for our data which compared well with the values of $u_\epsilon = 1.2u_\star$ of Laubach and McNaughton (2009). Again, it was found that the nonlocal scaling parameters described by this new model work well within the CBL to collapse the w-component of wind, temperature and heatflux spectra near the peak at the wavenumber axis. That implies that unlike the Monin-Obukhov similarity interpretation of the local nature of turbulence, convective boundary layer turbulence is a nonlocal, self-organizing dynamical system.

7.1 Discussion

During the implementation of this top-down N_2O flux measurement project it was realized that a precise measurement of N_2O concentration is only a small part of the

verification process of FG-EC method as greater challenges lie in finding an accurate emission rate from a particular field. An already established local scale turbulence model was used to compute flux values. Fluxes from the control plots were found to agree well with the previously reported values from some chamber/Lysimeter measurements. Now, it is to be noted that a micrometerological measurement system includes more degrees of freedom than a chamber in terms of agro-meteorological conditions. Therefore, a good agreement of measured fluxes from these two different systems is indeed encouraging. However, when the emission rate was computed by the proposed inverse footprint approach, actual emission rates were found to be on average 2.1% higher than the measured flux for the control plots which increased up to a maximum of 15.9% for subplot D. Since the overall footprint corrected emission rate values are not significantly different than the measured flux values assigned to each plot based on wind bisectors, readers might ask why such a detailed footprint correction is of interest. The answer to this question lies in the fact that geometry and location of sensors plays a very important role in a multiplot measurement setup as "Unfortunately, emission rate estimates for multi-source problems are often badly behaved, with spurious predictions obtained comparably often to appropriate values (Raupach, 1989)." (quoted from Crenna et al. (2008), pp 7373). Therefore, a rigorous footprint analysis is necessary for multiplot flux measurement, irrespective of the end product.

Again, when the effect of mitigation on the N_2O flux was explored using the micrometerological data, no significant change in the measured fluxes was observed for the mitigated plots. Such a result was in conflict with the already existing knowledge of the reducing effect of a mitigant, DCD, on N_2O emission rate over pastures of New Zealand. Within a wider range of random error in the measured flux, it was concluded that either there was no effect of mitigation at all or the effect of mitigation was less than 10%. Again, it should also be kept in mind that all the reported values of a reduced emission rate of N_2O under the influence of DCD for pastoral condition of New Zealand were observed when measurements were made using chambers/lysimeters over urine patches. As a consequence, it was conjectured that either the soil of the proposed site had lesser nitrous oxide production potential or there were irregularities in the application of DCD or a further verification of the fundamental concept of the eddy diffusivity based micrometeorological setup was needed.

Therefore, during another experiment of 2011 FarmGas campaign (partly desribed in Chapter 6), a 10 meter tall tower observation of atmospheric surface layer turbulence was analyzed to investigate a new convective boundary layer turbulence model

of Laubach and McNaughton (2009) which was developed based on the chaotic dynamical system approach of McNaughton (2004a,b) and McNaughton et al. (2007). The verification experiment showed that the proposed scaling parameters of the new model work well and can explain most of the discrepancies of the standard Monin-Obukhov similarity theory based turbulence model. Such an inference has enormous future possibilities as a completely new practical model of CBL can be developed.

7.2 Possible future work

A micrometerological method of N_2O flux measurement has been verified in this research and observations from only two different field experiments have been analyzed. Durations of the field experiments were short and measurements were hindered by occasional grazing. Hence, the dataset was not big enough for an indepth study of seasonal variation of the N_2O flux. Therefore, possible future work should include such an experimental setup, where fluxes can be measured continuously for longer periods so that seasonal variations can be explored.

No effect of mitigation was observed with this present setup of N_2O flux measurement. This might be because of the low soil N_2O production rate of the particular site, and therefore, this setup of flux measurement should be tested over other soil types of New Zealand as well.

Again, during the footprint analysis it was realized that the alternative measurement of fluxes from four measurement masts had made the footprint correction difficult. A simplistic experimental setup with one mitigated and one control plot would have helped both measurement and footprint correction. Therefore, it should be noted that a simplistic experimental setup is desirable for such a micrometeorological flux measurement system.

Finally, the present research was performed over an agricultural field near to the Southern Alps of New Zealand and no effect of synoptic scale meteorological events (such as the effect of large eddies or katabatic wind) on the surface layer turbulence was investigated. Since the large scale eddies or roll vortices can have signatures in the atmospheric surface layer flows as mentioned in Zhang et al. (2010), a future study may include investigation of this interaction from a meteorological perspective.

Appendix A

WPL Correction

Webb correction or WPL (Webb, Pearman and Leuning) correction is necessary for eddy covariance measurement of chemical species flux in the presence of simultaneous fluxes of sensible heat and water vapour. The vertical surface flux (F_g) for a constituent gas g is described as: $F_g = \overline{w}.\overline{c}_g + \overline{w'c'_g}$, where w is the vertical wind velocity and c_g is the gas concentration. $\overline{w}$ was assumed to be equal to zero, but Webb proposed that because of the density variation associating the simultaneous fluxes of sensible heat and water vapour, $\overline{w} \neq 0$. Although $\overline{w}$ is small in magnitude and difficult to estimate, Webb described a method of calculation of $\overline{w}$ from heat and water vapour flux and from the background concentration of a specific gas. Webb et al. (1980) started by assuming dry air conditions, which was later modified to include moist air as well. The mean vertical wind velocity is included in the correction term which is represented as (Foken and Nappo, 2008):

$$F_g = \overline{c_g}\frac{Q_H}{c_p\overline{T}}[1 + \frac{(1.61c_p\overline{T})}{\lambda}\frac{(1 - 0.61\overline{q})}{\beta_0}] + \overline{w'c'_g} \tag{A.1}$$

Q_H is sensible heat flux, λ is the latent heat of evaporation, c_p is the specific heat of air, $\overline{T}$ is mean air temperature, $\overline{q}$ is mean water vapour concentration, and β_0 is the Bowen ratio.

Appendix B

Coordinate rotation

The coordinate rotation or the tilt correction method is applied to make the mean vertical wind component equal to zero ($\overline{w} = 0$). This is one of the basic requirements of the eddy covariance system. Different methods have been proposed for the tilt correction and the procedure described by McMillen (1988) is followed here. A brief description of the method used for our calculation is as follows:

If u_m, v_m and w_m are the measured wind components with mean values of $\overline{u_m}, \overline{v_m}$ and $\overline{w_m}$, then a derived angle, α, can be expressed as:

$$\alpha = tan^{-1}(\frac{\overline{v_m}}{\overline{u_m}}) \tag{B.1}$$

and β can be expressed as:

$$\beta = tan^{-1}(\frac{\overline{w_m}}{\overline{u_{horz}}}) \tag{B.2}$$

where, $\overline{u_{horz}} = (\overline{u_m}^2 + \overline{v_m}^2)^{1/2}$ is the horizontal wind speed. Finally, the rotated wind components ($u_{rot}, v_{rot}, w_{rot}$) can be expressed as:

$$\begin{aligned} u_{rot} &= u_m.cos\alpha.cos\beta + v_m.sin\alpha.cos\beta + w_m.sin\beta \\ v_{rot} &= u_m.sin\alpha + v_m.cos\alpha \\ w_{rot} &= -u_m.cos\alpha.sin\beta - v_m.sin\alpha.sin\beta + w_m.cos\beta \end{aligned} \tag{B.3}$$

Appendix C

Essential findings of McMillan et al. (2012)

The important results of McMillan et al. (2012) in terms of nitrous oxide gradient (ΔN_2O) measurements from the field campaigns of 2010 (autumn and spring experiments) are excerpted below.

C.1 Performance of the micrometeorological system in determining N_2O gradients

"During the Autumn Experiment, ΔN_2O was sampled over a 30 minute period at each tower. Each 30-minute determination comprised 100 individual comparisons of a 9 s N_2O determination at a height of 0.5 m and a 9 s N_2O determination at 1.0 m. During the Spring, the sampling consisted of a 20-minute period comprising 100 comparisons of 6 s N_2O determinations at 0.5 and 1.0 m.

For illustrative purposes, two selected gradient measurements are shown for well mixed daytime conditions (Figure C.1a) and stable night time conditions (Figure C.1b). Under well-mixed conditions, ΔN_2O was usually low ($<$0.1 ppb) but repeated measurements allowed the value to be resolved to high precision, and ΔN_2O as low as 0.035 ppb could be resolved. Under stable conditions, which generally occurred at night, ΔN_2O was generally much higher. However, fluxes associated with these ΔN_2O were associated with a high level of uncertainty due to errors associated with determining the eddy diffusivity."

C.2 Frequency distribution of ΔN_2O

"N_2O concentration gradients were estimated by measuring the difference in N_2O concentration between 0.5 m and 1.0 m above the ground surface. This quantity is referred to as ΔN_2O with units of parts per billion (ppb). A positive value of ΔN_2O indicates that the concentration at 0.5 m is greater than the concentration at 1.0 m. We considered the plausible range of ΔN_2O to be between $\pm$15 ppb although the vast majority

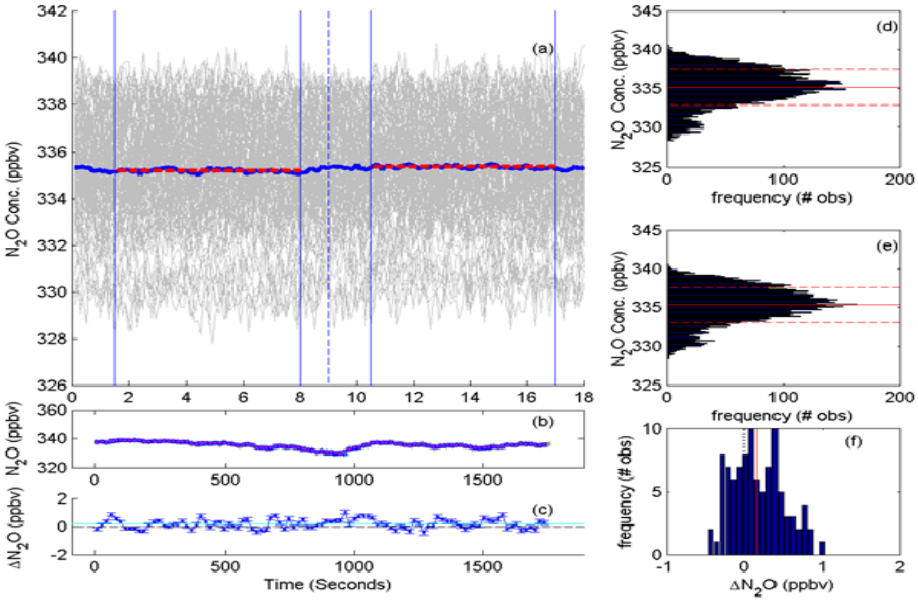

(a) Autumn

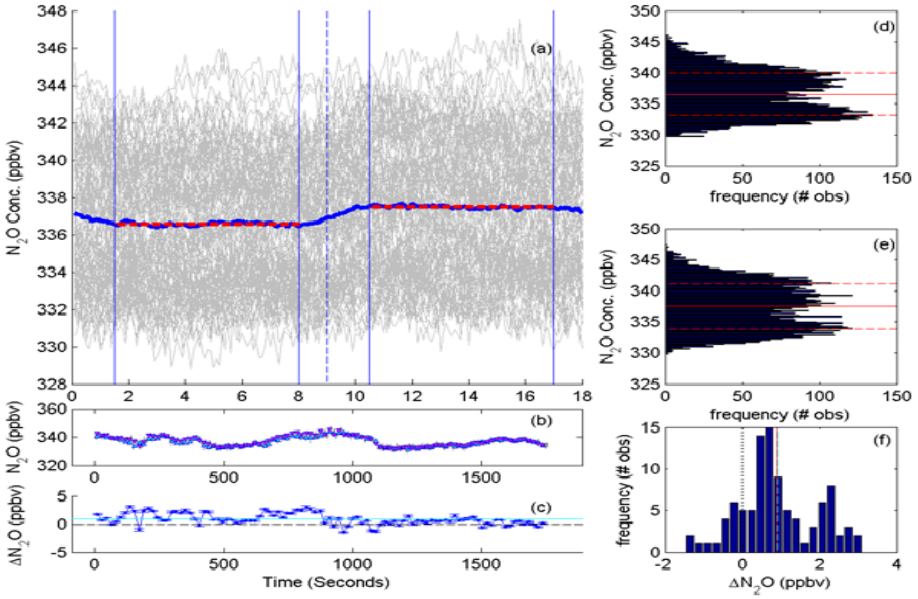

(b) Spring

Figure C.1: (Autumn) ΔN_2O measurement under neutral conditions (Stability Parameter $|z/L|$ = 0.01) on 25/5/2010 12:30-13:00. (a) 100 individual 18 s gradient determinations (grey lines), means at each 0.1 s measurement interval (blue lines) and average of blue lines (red dashed line) during valid measurement interval between each pair of vertical blue solid lines; (b) time series of concentration and (c) measured gradients over the entire measurement interval (1800 s). Histograms of individual 0.1 s N_2O determinations for the (d) upper inlet and (e) lower inlet. (f) Histogram of the 100 determined gradients (f) the black dashed line is the zero concentration gradient and the red line is the gradient determined from the difference between the averaged concentrations depicted by the red lines in plot (a). The gradient for this period is 0.163$\pm$0.041 ppb, a difference that is significant at the P$<$1% level. The windspeed was 3.5 m/s and $u_\star$ = 0.22 m/s. (Spring) ΔN_2O measurement under stable conditions on 10/6/2010 00:00-00:30. The gradient for this period is 0.920$\pm$0.062 ppb, a difference that is significant at the P$<$1% level. The wind speed was 1.6 m/s, $u_\star$ = 0.03 m/s, and z/L = 1.01 (stable).

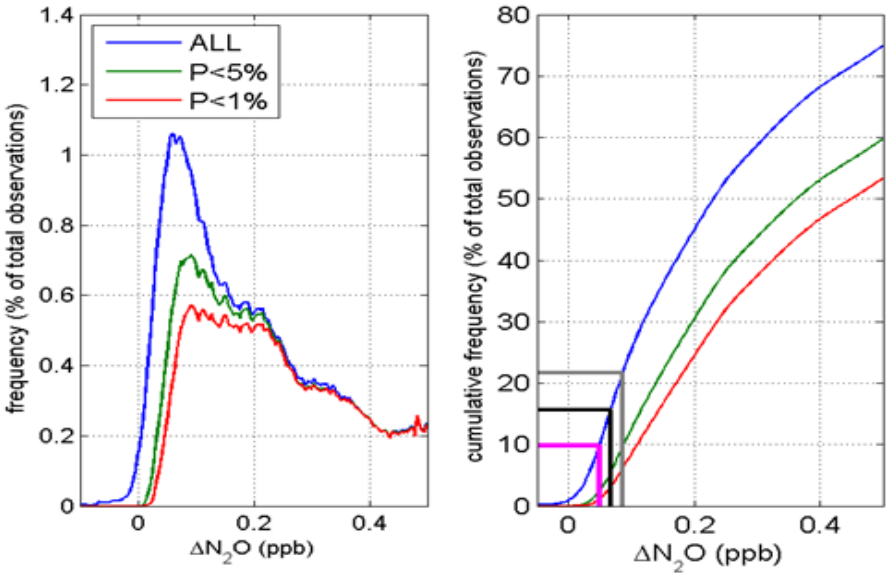

Figure C.2: Frequency distribution (left) and cumulative frequency distribution (right) of all measured gradients. The grey line on panel (b) indicates that 21.7% of ΔN_2O values were less than 0.088 ppb, which is the P<1% resolution limit for the Autumn Experiment. Similarly, the black line indicates that 15.6% of ΔN_2O values were less than 0.066 ppb, which is the P<1% resolution for the Spring Experiment. The magenta line indicates that 10.0% of ΔN_2O values were less than $\Delta N_2O min_{best\,est}$ (which is 0.049 ppb).

of ΔN_2O were positive and smaller than 1 ppb (Figure C.2).

The largest ten gradients ranged between 15 and 88 ppb, and generally occurred under very stable conditions. The lowest ten gradients significant at P<1% ranged from 0.035 to 0.046 (ppb). The most commonly observed (modal) gradient was 0.057 ppb (Figure C.3). The frequency distribution of ΔN_2O was approximately log-normal."

C.3 Diurnal variation of ΔN_2O

" ΔN_2O was higher during daytime than at night and the magnitude of this difference was generally greater during the Autumn Experiment than during the Spring Experiment (Figure C.4). The principal driver for diurnal variation in ΔN_2O was the diurnal variation in surface layer mixing. The influence of the soil flux intensity on ΔN_2O will be superimposed upon this diurnal pattern. Calmness during night time periods leads to the build-up of large vertical gradients of N_2O. During the Autumn Experiment, night time conditions were calmer than during the Spring Experiment. Consequently, much larger gradients occurred at night in Autumn. While the minimum value of ΔN_2O was similar in both seasons (about 0.15 ppb), the minimum of ΔN_2O lasted for a longer time in Autumn than in Spring. Night time values during autumn were generally a lot more variable than in Spring. This is due in part to the greater transfer coefficients during the spring, which are associated with lower N_2O gradients."

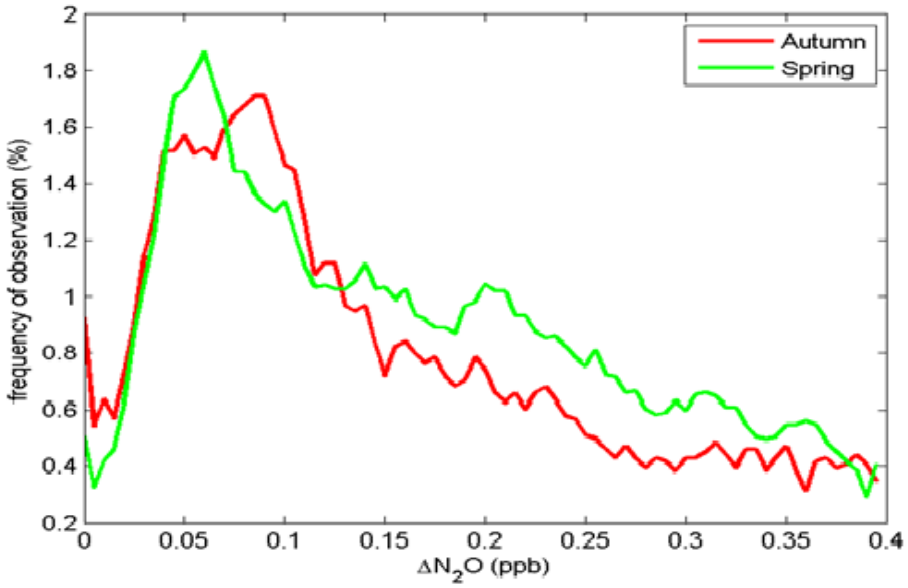

Figure C.3: Frequency distribution of gradient observations for the autumn and spring experiments.

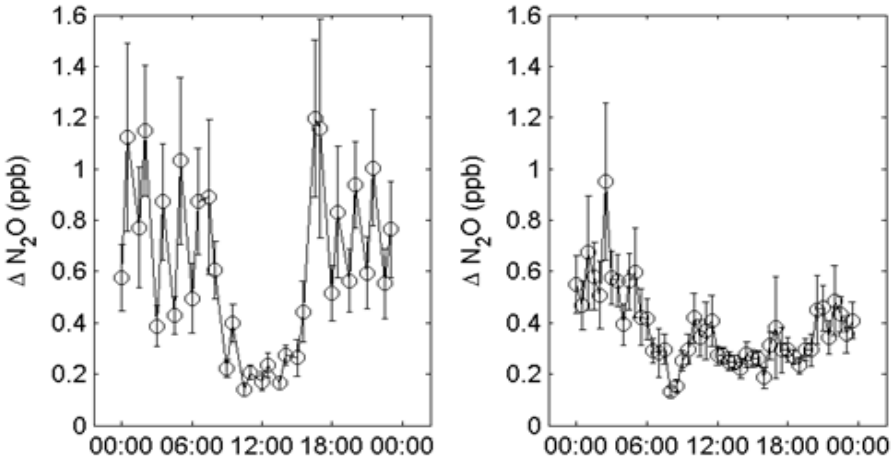

Figure C.4: Diurnal variability in N_2O during the Autumn (left panel) and the Spring (right panel) Experiments.

Appendix D

Unit of nitrous oxide flux

The nitrous oxide flux values are estimated using d_h^p values of Chapter 3 where F_g is defined as $F_g = \rho_a \Delta \rho_g d_h^p$. The unit of F_g can be expressed as:

$$F_g \quad = \frac{mol_{air}}{m^3} \frac{nmol}{mol_{air}} \frac{m}{s} \quad = nmol.m^{-2}.s^{-1} \tag{D.1}$$

Similarly, flux values were estimated using k_h^t values following $F_g = \rho_a \frac{\Delta c_g}{\Delta z} k_h^t$. The unit of F_g can be expressed as:

$$F_g \quad = \frac{mol_{air}}{m^3} \frac{nmol}{mol_{air}} \frac{1}{m} \frac{m^2}{s} \quad = nmol.m^{-2}.s^{-1} \tag{D.2}$$

Now, converting the above equation to per hectare values as:

$$F_g = 10^4 \ \ nmol.ha^{-1}.s^{-1} \tag{D.3}$$

and converting the above equation to per day values as:

$$F_g = 864 \times 10^6 \ \ nmol.ha^{-1}.day^{-1} \tag{D.4}$$

and converting the above equation to moles as:

$$F_g = 864 \times 10^{-3} \ \ mol.ha^{-1}.day^{-1} \tag{D.5}$$

and converting the above equation to grams (g) of N_2O-N as:

$$\begin{aligned} F_g = 28 \times 864 \times 10^{-3} \ \ gN_2O - N.ha^{-1}.day^{-1} \\ F_g = 24.192 \ \ gN_2O - N.ha^{-1}.day^{-1} \end{aligned} \tag{D.6}$$

where 28 is the formula weight of N_2. Therefore, when the right hand side of Equation D.1 is multiplied by 24.197, the flux unit becomes gN_2O-N.ha^{-1}.day^{-1}.

Appendix E

Korman-Meixner footprinting model

The two dimensional Korman-Meixner footprint function has already been shown in Equation 4.10. The solution of the analytical footprint approach is based on the power law relationship of the wind speed profile and vertical eddy diffusivity. Only the coefficients of Equation 4.10 are described here following Neftel et al. (2008). Two more exponents, *p* and *n*, are deduced to represent coefficients of Equation 4.10. These are expressed as:

$$\begin{aligned} p &= \frac{u_\star}{\kappa u(z_m)}\phi_M \\ n &= \frac{z_m}{\phi_M}\frac{d\phi_M}{dz_m} \end{aligned} \tag{E.1}$$

Here z_m is the measurement height, and ϕ_M is a stability parameter after Dyer (1974) and a function of z_m/L, and κ is the von Karman constant. Coefficient *A* is:

$$\begin{aligned} A &= 1+\mu \\ where, \mu &= \frac{1+p}{r} \end{aligned} \tag{E.2}$$

where *r* = 2+*p*-*n*. Coefficient *B* is:

$$\begin{aligned} B &= \frac{U {z_m}^r}{r^2 k} \\ where, U &= \frac{u_\star \phi_M}{\kappa p {z_m}^p} \end{aligned} \tag{E.3}$$

where $k = (\kappa u_\star z_m)/(\phi_H {z_m}^n)$. ϕ_H is also a dimensionless stability parameter after Dyer (1974). Coefficient *C* is:

$$C = \frac{B^\mu}{\Gamma(\mu)} \tag{E.4}$$

where Γ represents the Gamma function and D and E can be expressed as:

$$D = \frac{\sigma_v}{\mu} \frac{\Gamma(1/r)}{\Gamma(\mu)} \left(\frac{U}{r^2 k} \right)^{p/r} \tag{E.5}$$

$$E = \frac{r - p}{r} \tag{E.6}$$

Bibliography

Abramowitz, M. and Stegan, I. (2002). *Handbook of Mathematical Functions with Formulas, Graphs, and Mathematical Tables.* U.S. Department of Commerce.

Arya, S. (2001). *Introduction to micrometeorology.* Academic Press, San Diego.

Bjorneberg, D., Leytem, A., Westermann, D., Griffiths, P., Shao, L., and Pollard, M. (2009). Measurement of atmospheric ammonia, methane and nitrous oxide at a concentrated dairy production facility in southern Idaho using open-path FTIR spectrometry. *Transactions of the American Society of Agricultural and Biological Engineers*, 52(5):1749–1756.

Bolan, N., Saggar, S., Lou, J., Bhandral, R., and Singh, J. (2004). Gaseous emissions of nitrogen from grazed pastures: processes, measurements and modelling, environmental implications and mitigation. *Advances in Agronomy*, 84:37–120.

Bouwman, A. F., Boumans, L. J. M., and Batjes, N. H. (2002). Emissions of N2O and NO from fertilized fields: Summary of available measurement data. *Global Biogeochemical Cycles*, 16(4):1058.

Burba, G. and Anderson, D. (2010). Introduction to the eddy covariance method: General guidelines and conventional workflow. *LICOR Eddy Covariance Manual, http://www.licor.com.*

Businger, J. (1986). Evaluation of the accuracy with which dry deposition can be measured with current micrometeorological techniques. *Journal of Climate and Applied Meteorology*, 25:1100–1124.

Businger, J., Wyngaard, J., Izumi, Y., and Bradley, E. (1971). Flux profile relationships in the atmospheric surface layer. *Journal of Atmospheric Sciences*, 28(2):181–189.

Cai, X., Chen, J., and Desjardins, R. (2010). Flux footprints in the convective boundary layer: Large-eddy simulation and lagrangian stochastic modelling. *Boundary-Layer Meteorology*, 137(1):31–47.

Cai, X. and Leclerc, M. (2007). Forward-in-time and backward-in-time dispersion in the convective boundary layer: the concentration footprint. *Boundary-Layer Meteorology*, 123:201–218.

Cicerone, R. J. (1989). Analysis of the sources and sinks of atmospheric nitrous oxide (N_2O). *Journal of Geophysical Research*, 94:18265–18271.

Crenna, B. P., Flesch, T. K., and Wilson, J. D. (2008). Influence of source-sensor geometry on multi-source emission rate estimates. *Atmospheric Environment*, 42(32):7373–7383.

Crutzen, P., Mosier, A., Smith, K., and Winiwarter, W. (2008). N2O release from agro-biofuel production negates global warming reduction by replacing fossil fuels. *Atmospheric Chemistry and Physics*, 8:389–395.

De Klein, C., Barton, L., Sherlock, R., Li, Z., and Littlejohn, R. (2003). Estimating a nitrous oxide emission factor for animal urine from some New Zealand pastoral soils. *Australian Journal of Soil Research*, 41:381–399.

De Klein, C. and Eckard, R. (2008). Targeted technologies for nitrous oxide abatement from animal agriculture. *Australian Journal of Experimental Agriculture*, 48:14–20.

De Klein, C., Harvey, M., and Letica, S. (2011). Workshop report: Nitrous Oxide Chamber Methodology Guidelines. Technical report, Govt. of New Zealand.

Deardroff, J. (1972). Numerical investigations of neutral and unstable planetary boundary lauyers. *Journal of Atmospheric Sciences*, 29:91–115.

Delgrosso, S., Mosier, A., Parton, W., and Ojima, D. (2005). DAYCENT model analysis of past and contemporary soil NO and net greenhouse gas flux for major crops in the USA. *Soil and Tillage Research*, 83(1):9–24.

Denman, K., Brasseur, G., Chidthaisong, G., Ciais, P., Cox, R., Dickinson, D., Hauglustaine, C., Heinze, E., Holland, E., Jacob, D., Lohmann, U., Ramachandran, S., da Silva, D., Wofsy, F., and Zhang, X. (2007). Couplings between changes in the climate system and biogeochemistry. In *Climate change 2007: The physical science basis. Contribution of the working group 1 to the fourth assessment report of the Intergovernmental Panel on Climate Change*, pages 499–587. Cambridge University Press, Cambridge, UK.

Denmead, O. (2008). Approaches to measuring fluxes of methane and nitrous oxide between landscapes and the atmosphere. *Plant and Soil*, 309(1):5–24.

Di, H. and Cameron, K. (2002a). The use of a nitrification inhibitor, dicyandiamide DCD, to decrease nitrate leaching and nitrous oxide emissions in a simulated grazed and irrigated grassland. *Soil Use and Management*, 18:395–403.

Di, H. and Cameron, K. (2003). Mitigation of nitrous oxide emissions in spray-irrigated grazed grassland by treating the soil with dicyandiamide, a nitrification inhibitor. *Soil Use and Management*, 19:284–290.

Di, H., Cameron, K., and Sherlock, R. (2007). Comparison of the effectiveness of a nitrification inhibitor, dicyandiamide, in reducing nitrous oxide emissions in four different soils under different climatic and management conditions. *Soil Use and Management*, 23:1–9.

Di, H. J. and Cameron, K. C. (2002b). Nitrate leaching in temperate agroecosystems: sources, factors and mitigating strategies. *Nutrient Cycling in Agroecosystems*, 46(3):237–256.

Dyer, A. (1974). A review of flux profile relationships. *Boundary-Layer Meteorology*, 7:363–372.

Dyer, A. and Bradley, E. (1982). An alternative analysis of flux-gradient relationships at the 1976 ITCE. *Boundary-Layer Meteorology*, 22(1):3–19.

Farquharson, R. and Baldock, J. (2008). Concepts in modelling N2O emissions from land use. *Plant and Soil*, 309(1):147–167.

Fench, M. (2004). A simple method to estimate the eddy dissipation rate from SODAR/RASS measurements. In *16th Symposium on Boundary Layers and Turbulence*, pages 6.13.1 – 6.13.4. American Meteorological Society.

Finnigan, J., Clement, R., Malhi, Y., Leuning, R., and Cleugh, H. (2003). A reevaluation of long-term flux measurement techniques - part i: Averaging and coordinate rotation. *Boundary-Layer Meteorology*, 107:1–48.

Flesch, T., Wilson, J., Harper, L., and Crenna, B. (2005). Estimating gas emissions from a farm with an inverse-dispersion technique. *Atmospheric Environment*, 39:4863–4874.

Flesch, T., Wilson, J., Harper, L., Crenna, B., and Sharpe, R. (2004). Deducing ground-to-air emissions from observed trace gas concentrations: A field trial. *Journal of Applied Meteorology*, 43:487–502.

Flesch, T., Yee, E., and Wilson, J. (1995). Backward-time lagrangian stochastic dispersion models and their application to estimate gaseous emissions. *Journal of Applied Meteorology and Climatology*, 34(6):1320–1332.

Foken, T. and Nappo, C. (2008). *Micrometeorology*. Springer, Berlin.

Freeman, J. and Dale, R. (2012). Assessing bimodality to detect the presence of a dual cognitive process. *Behavior Research Methods*, pages 1–15.

Garratt, J. (1992). *The atmospheric boundary layer.* Cambridge University Press, Melbourne.

Gash, J. (1986). A note on estimating the effect of a limited fetch on micrometeorological evaporation measurements. *Boundary-Layer Meteorology*, 35:409.

Goulden, M., Munger, J., Fan, S., Daube, B., and Wofsy, S. (1996). Measurement of carbon sequestration by long-term eddy covariance:methods and a critical evaluation of accuracy. *Global Change Biology*, 2(3):169–182.

Grant, R., Pattey, E., Goddard, T., Kryzanowski, L., and Puurveen, H. (2006). Modeling the effects of fertilizer application rate on nitrous oxide emissions. *Soil Science Society of America Journal*, 70:235–248.

Hartigan, J. A. and Hartigan, P. M. (1985). The dip test of unimodality. *The Annals of Statistics*, 13(1):70–84.

Harvey, M., Laubach, J., Giltrap, D., Hudson, N., and Wheeler, D. (2008a). Enhancing confidence in extrapolating emission measurements. Technical report, NIWA Client Report:WLG2008-71.

Harvey, M., Pattey, E., Saggar, S., Bromley, T., Dow, D., Kotkamp, M., Martin, R., Moss, R., and Singh, J. (2008b). Verification techniques for N2O emission at the paddock scale in New Zealand: Farmgas2006. *Australian Journal of Experimental Agriculture*, 48(1-2):138–141.

Hogstrom, U. (1988). Non-dimensional wind and temperature profiles in the atmospheric surface layer: A re-evaluation. *Boundary-Layer Meteorology*, 42(1-2):55–78.

Hogstrom, U., Hunt, J., and Smedman, A. (2002). Theory and measurements for turbulence spectra and variances in the atmospheric neutral surface layer. *Boundary-Layer Meteorlogy*, 103:101–124.

Hollinger, D. and Richardson, A. (2005). Uncertainty in eddy covariance measurements and its application to physiological models. *Tree Physiology*, 25(7):873–885.

Holtslag, A. and Nieuwstadt, F. (1986). Scaling the atmospheric boundary layer. *Boundary-Layer Meteorology*, 36:201–209.

Horst, T. (1999). The footprint for estimation of atmosphere-surface exchange fluxes by profile techniques. *Boundary-Layer Meteorology*, 90(2):171–188.

Horst, T. and Weil, J. (1994). How far is far enough - the fetch requirements for micrometeorological measurement of surface fluxes. *Journal of Atmospheric and Oceanic Technology*, 11(4):1018–1025.

Hsieh, C., Chi, T., and Katul, G. (2000). An approximate analytical model for footprint estimation of scaler fluxes in thermally stratified atmospheric flows. *Advances in Water Resources*, 23(7):765–772.

Kader, B. A. and Yaglom, A. M. (1990). Mean fields and fluctuation moments in unstably stratified turbulent boundary layers. *Journal of Fluid Mechanics*, 212(1):637–662.

Kaimal, J. and Finnigan, J. (1994). *Atmospheric boundary layer flows: their structure and measurement.* Oxford University Press, New York.

Kaimal, J., Wyngaard, J., Haugen, D., Cote, O., Izumi, Y., Coughey, S., and Readings, C. (1976). Turbulence structure in the convective boundary layer. *Journal of Atmospheric Sciences*, 33:2152–2169.

Kaimal, J., Wyngaard, J., Izumi, Y., and Cote, O. (1972). Spectral characteristics of surface layer turbulence. *Quarterly Journal of the Royal Meteorological Society*, 98:563–589.

Katurji, M., Sturman, A., and Zawar-Reza, P. (2011). An investigation into ridgetop turbulence characteristics during neutral and weakly stable conditions: Velocity spectra and isotropy. *Boundary-Layer Meteorology*, 139(1):143–160.

Kelliher, F., Reisinger, A., Martin, R., Harvey, M., Price, S., and Sherlock, R. (2002). Measuring nitrous oxide emission rate from grazed pasture using fourier-transform infrared spectroscopy in the nocturnal boundary layer. *Agricultural and Forest Meteorology*, 111(1):29–38.

Kljun, N., Calanca, P., Rotach, M., and Schmid, H. (2004). A simple parameterisation for flux footprint predictions. *Boundary-Layer Meteorology*, 112(3):503–523.

Kljun, N., Korman, R., Rotach, M., and Meixner, F. (2003). Comparison of the langrangian footprint model LPDM-B with an analytical footprint model. *Boundary-Layer Meteorology*, 106(2):349–355.

Kormann, R. and Meixner, F. (2001). An analytical footprint model for non-neutral stratification. *Boundary-Layer Meteorology*, 99(2):207–224.

Kouznetsov, R., Kramer, V., Beyrich, F., and Engelbart, D. (2004). SODAR-based estimation of TKE and momentum flux profiles in the atmospheric boundary layer: Test of a parameterization model. *Meteorology and Atmospheric Physics*, 85:93–99.

Kramar, V. and Kouznetsov, R. (2002). A new concept for estimation of turbulent parameter profiles in the ABL using Sodar data. *Journal of Atmospheric and Oceanic Technology*, 19:1216–1224.

Kroon, P., Hensen, A., Jonker, H., Ouwersloot, H., Vermeulen, A., and Bosveld, F. (2010). Uncertainties in eddy covariance flux measurements assessed from CH4 and N2O observations. *Agricultural and Forest Meteorology*, 150(6):806–816.

Laubach, J. (2010). Testing of a lagrangian model of dispersion in the surface layer with cattle methane emissions. *Agricultural and Forest Meteorology*, 150(11):1428–1442.

Laubach, J. and Kelliher, F. (2004). Measuring methane emission rates of a dairy cow herd by two micrometeorological techniques. *Agricultural and Forest Meteorology*, 125(3-4):279–303.

Laubach, J. and Kelliher, F. (2005). Measuring methane emission rates of a dairy cow herd (ii): results from a backward-lagrangian stochastic model. *Agricultural and Forest Meteorology*, 129(3-4):137–150.

Laubach, J. and McNaughton, K. (1998). A spectrum independent procedure for correcting eddy fluxes measured with separated sensors. *Bondary-Layer Meteorology*, 89(3):445–467.

Laubach, J. and McNaughton, K. (2009). Scaling properties of temperature spectra and heat-flux cospectra in the surface friction layer beneath an unstable outer layer. *Bondary-Layer Meteorology*, 133(2):219–252.

Leclerc, M., Shen, S., and Lamb, B. (1997). Observations and large-eddy simulation modeling of footprints in the lower convective boundary layer. *Journal of Geophysical Research-Atmospheres*, 102(D8):9323–9334.

Li, C. S. (2000). Modeling trace gas emissions from agricultural ecosystems. *Nutrient Cycling in Agroecosystems*, 58(1):259–276.

Lundegardh, H. (1926). Carbon dioxide evolution of soil and crop growth. *Soil Science*, 23:417–450.

Luo, J., Lindsey, S. B., and Ledgard, S. F. (2008a). Nitrous oxide emissions from animal urine application on a new zealand pasture. *Biology and Fertility of Soils*, 44(3):463–470.

Luo, J., Saggar, S., Bhandral, R., Bolan, N., Ledgard, S., Lindsey, S., and Sun, W. (2008b). Effects of irrigating dairy-grazed grassland with farm dairy effluent on nitrous oxide emissions. *Plant and Soil*, 309(1):119–130.

Mahrt, L. (1998). Flux sampling errors from aircraft and towers. *Journal of Atmosphere and Oceanic Technology*, 15:416–429.

Mammarella, I., Werle, P., Pihlatie, M., Eugster, W., Haapanala, S., Kiese, R., Markkanen, T., Rannik, U., and Vesala, T. (2010). A case study of eddy covariance flux of n2o measured within forest ecosystems: quality control and flux error analysis. *Biogeosciences*, 7(2):427–440.

Matthias, A., Blackmer, A., and Bremner, J. (1980). A simple chamber technique for field measurement of emissions of nitrous oxide from soils. *Journal of Environmental Quality*, 9:251–256.

McLachlan, G. and Peel, D. (2000). *Finite mixture models*. Wiley, New York.

McMillan, A., Harvey, M., Martin, R., Bromley, T., Evans, M., Mukherjee, S., and Laubach, J. (2013). A micrometeorological method to assess the efficacy of a nitrous oxide mitigation strategy. *Under review Agricultural and Forest Meteorology*.

McMillan, A., Harvey, M., Martin, R., Evans, M., and Bromley, T. (2012). Determination of nitrous oxide emissions and mitigation efficacy using a paddock-scale measurement system. Technical report, Prepared for Ministry of Agriculture and Forestry, New Zealand.

McMillen, R. (1988). An eddy correlation technique with extended applicability to non-simple terrain. *Boundary-Layer Meteorology*, 43(3):231–245.

McNaughton, K. (2004a). Attached eddies and production spectra in the atmospheric logarithmic layer. *Boundary-Layer Meteorology*, 111:1–18.

McNaughton, K. (2004b). Turbulence structure of the unstable atmospheric surface layer and transition to the outer layer. *Boundary-Layer Meteorology*, 112(2):199–221.

McNaughton, K. (2006). On the kinetic energy budget of the unstable atmospheric surface layer. *Boundary-Layer Meteorology*, 118:83–107.

McNaughton, K. (2009). Rise and fall of monin-obukhov theory. *AsiaFlux Newsletter*, 30:1–4.

McNaughton, K., Clement, R., and Moncrieff, J. (2007). Scaling properties of velocity and temperature spectra above the surface friction layer in a convective atmospheric boundary layer. *Nonlinear Processes in Geophysics*, 14(3):257–271.

McNaughton, K. and Laubach, J. (1998). Unsteadiness as a cause of non-equality of eddy diffusivities for heat and vapour at the base of an advective inversion. *Boundary-Layer Meteorology*, 88:479–504.

McNaughton, K. and Laubach, J. (2000). Power spectra and co-spectra for wind and scalars in a disturbed surface layer at the base of an advective inversion. *Boundary-Layer Meteorology*, 96:143–185.

McNaughton, K. G. (2012). The flow of mechanical energy in convective boundary layers. *Boundary-Layer Meteorology*, 145(1):145–163.

McTaggart, I., Smith, K., and Dobbie, K. (1999). Nitrous oxide emissions from intensive agricultural systems: Variations between crops and seasons, key driving variables, and mean emission factors. *Journal of Geophysical Research-Atmospheres*, 104(D21):26891–26899.

Ministry for Primary Industries, G. o. N. Z. (2012). http://www.mpi.govt.nz/environment-natural-resources/climate-change/sustainable-land-management-and-climate-change.aspx. accessed: 1 September 2012.

Moncrieff, J., Malhi, Y., and Leuning, R. (1996). The propagation of errors in long-term measurements of land-atmosphere fluxes of carbon and water. *Global Change Biology*, 2:231–240.

Monin, A. and Obukhov, A. (1954). Osnovnye zakonomernosti turbulentnogo peremesivanija v prizemnom sloe atmosphery (Basic laws of turbulent mixing in the atmosphere near the ground). *Trudy geofiz inst AN SSSR*, 24:163–187.

Mukherjee, S., Sturman, A., McMillan, A., Harvey, M., and Zawar-Reza, P. (2013). Assessment of error propagation in measured flux values of an eddy diffusivity based micrometeorological setup. *Submitted to Atmospheric Environment*.

Nakanishi, M. and Niino, H. (2004). An improved mellor-yamada level-3 model with condensation physics: Its design and verification. *Boundary-Layer Meteorology*, 112(1):1–31.

Neftel, A., Flechard, C., Ammann, C., Conen, F., Emmenegger, L., and Zeyer, K. (2007). Experimental assessment of N2O background fluxes in grassland systems. *Tellus B*, 59:470–482.

Neftel, A., Spirig, C., and Ammann, C. (2008). Application and test of a simple tool for operational footprint evaluations. *Environmental Pollution*, 152(3):644–652.

Olson, J. B. and Brown, J. M. (2009). A comparison of two mellor-yamada-based pbl schemes in simulating a hybrid barrier jet. In *The 23rd Conference on Weather Analysis and Forecasting/19th Conference on Numerical Weather Prediction*, pages JP1.13.1 – JP1.13.14.

Parkin, T. (2008). Effect of sampling frequency on estimates of cumulative nitrous oxide emissions. *Journal of Environmental Quality*, 34(4):1390–1395.

Pasquil, F. and Smith, F. (1983). *Atmospheric Diffusion.* Wiley, New York, 3rd edition.

Pattey, E., Desjardins, R., Pennock, D., Edwards, G., Smith, W., Grant, B., and MacPherson, J. (2006a). Tools for quantifying N2O emissions from agroecosystems. *Agricultural and Forest Meteorology*, 142(2-4):103–119.

Pattey, E., Edwards, G., Strachan, I., Desjardins, R., Kaharabata, S., and Wagner Riddle, C. (2006b). Towards standards for measuring greenhouse gas fluxes from agricultural fields using instrumented towers. *Canadian Journal of Soil Science*, 86:373–400.

Paulson, C. (1970). The mathematical representation of wind speed and temperature profiles in the unstable atmospheric surface layer. *Journal of Applied Meteorology*, 9:857–861.

Petrie, S., Wear, S., Nottage, R., Scott, G., Wilson, T., Kennie, T., and Evans, D. (2006). New Zealand's greenhouse gas inventory 1990-2004. The national inventory report and common reporting format, April 2006. Technical report, Ministry for the Environment, Govt of New Zealand.

Phillips, F., Leuning, R., Baigent, R., Kelly, K., and Denmead, O. (2007). Nitrous oxide flux measurements from an intensively managed irrigated pasture using micrometeorological techniques. *Agricultural and Forest Meteorology*, 143:92–105.

Prather, M., Derwent, R., Ehhalt, D., Fraser, P., Sanhueza, E., and Zhou, X. (1995). *Climate Change 1994. Radiative Forcing of Climate Change and an Evaluation of the IPCC IS92 Emission Scenarios. Houghton, J.T. and Meira Filho L.G. and Bruce, J. and Hoesung Lee and Callander, B.A. and Haites, E. and Harris, N. and Maskell, K. (Eds)*. Cambridge University Press, Cambridge.

Qui, W., Di, H., Cameron, K., and Hu, C. (2010). Nitrous oxide emissions from animal urine as affected by season and a nitrification inhibitor dicyandiamide. *Journal of Soils and Sediments*, 10:1229–1235.

Raupach, M. R. (1989). Applying lagrangian fluid mechanics to infer scalar source distributions from concentration profiles in plant canopies. *Agricultural and Forest Meteorology*, 47(2):85–108.

Ravishankara, A., Daniel, J., and Portmann, R. (2009). Nitrous oxide (N2O): The dominant ozone-depleting substance emitted in the 21st century. *Science*, 326:123–125.

Rochette, P. and Eriksen-Hamel, N. (2008). Chamber measurements of soil nitrous oxide flux: Are absolute values reliable? *Soil Science Society of America Journal*, 72(2):331–342.

Rochette, P. and Hutchinson, G. (2005). Measurement of soil respiration in situ: Chamber techniques. In Hatfield, J. and Baker, J., editors, *Micrometeorology in agricultural systems.*, Agronomy Monogram, pages 247–286, Madison, WI.

Saggar, S., Harvey, M., Giltrap, D., Metherell, A., and Andrew, R. (2005). Simultaneous examination of nitrous oxide emissions in grazed pastures using paddock-scale measurements and process-based models. *Environmental Sciences*, 2:117–131.

Saggar, S., Harvey, M., Singh, J., Giltrap, D., Pattey, E., Bromley, T., Martin, R., Dow, D., Moss, R., and McMillan, A. (2010). Chambers, micrometeorological measurements, and the New Zealand denitrification-decomposition model for nitrous oxide emission estimates from an irrigated dairy-grazed pasture. *Journal of Integrative Environmental Sciences*, 7(supp1):61–70.

Saggar, S., Rodda, N., Hedley, C., Tate, K., Andrew, R., and Townsend, J. (2004). Modelling nitrous oxide emissions from dairy-grazed pastures. *Nutrient Cycling in Agroecosystems*, 68(3):243–255.

Saggar, S., Tate, K., Giltrap, D., and Singh, J. (2008). Soil-atmosphere exchange of nitrous oxide and methane in New Zealand terrestrial ecosystems and their mitigation options:a review. *Plant and Soil*, 309(1):25–42.

Schmid, H. (1994). Source areas for scalars and scalar fluxes. *Boundary-Layer Meteorology*, 67(3):293–318.

Schmid, H. (2002). Footprint modeling for vegetation atmosphere exchange studies: a review and perspective. *Agricultural and Forest Meteorology*, 113(1-4):159–183.

Schmid, H., Cleugh, H., Grimmond, C., and Oke, T. (1991). Spatial variability of energy fluxes in suburban terrain. *Boundary-Layer Meteorology*, 54:249–276.

Schmid, H. and Oke, T. (1990). A model to estimate the source area contributing to turbulent exchange in the surface layer over patchy terrain. *Quarterly Journal of the Royal Meteorological Society*, 116:965–988.

Schuepp, P., Leclerc, M., MacPherson, J., and Desjardins, R. (1990). Footprint prediction of scalar fluxes from analytical solutions of the diffusion equation. *Boundary-Layer Meteorology*, 50:355.

Singh, J., Saggar, S., Giltrap, D., and Bolan, N. (2008). Decomposition of dicyandiamide (DCD) in three contrasting soils and its effect on nitrous oxide emission, soil respiratory activity and microbial biomass − an incubation study. *Australian Journal of Soil Research*, 46:517–525.

Skiba, U., Sheppard, L., MacDonald, J., and Fowler, D. (1998). Some key environmental variables controlling nitrous oxide emissions from agricultural and semi-natural soils in Scotland. *Atmospheric Environment*, 32(19):3311–3320.

Smedman, A., Hogstrom, U., Hunt, J., and Sahlee, E. (2007). Heat/mass transfer in the slightly unstable atmospheric surface layer. *Quarterly Journal of Royal Meteorological Society*, 133:37–51.

Smith, K. and Conen, F. (2004). Measurement of trace gases: I Gas analysis, chamber methods, and related procedures. In Smith, K. and Cresser, M., editors, *Soil and environmental analysis: Modern instrumental techniques.*, pages 433–437.

Smith, K. and Dobbie, K. (2001). The effects of temperature, water-filled pore space and land use on n2o emissions from an imperfectly drained gleysol. *European Journal of Soil Science*, 52(4):667–673.

Sogachev, A. and Lloyd, J. (2004). Using a one-and-a-half order closure model of the atmospheric boundary layer for surface flux footprint estimation. *Boundary-Layer Meteorology*, 112(3):467–502.

Stull, R. (1988). *An Introduction to Boundary-Layer Meteorology.* Kluwer Academic Publishers, The Netherlands.

Sturman, A. and Spronken-Smith, R. (2001). *The Physical Environment: a New Zealand Perspective.* Oxford University Press, Melbourne.

Sweeney, C., Fraser, B., Hunt, M., Fyfe, J., Gulliver, S., Petrie, S., Godber, D., Tsui, K., Dahiya, A., Pickering, A., and Austin, D. (2011). New Zealand's greenhouse gas inventory 1990-2009. Submitted to the United Nations Framework Convention on Climate Change, 15 April 2011. Technical Report ISSN: 1179-223X, Ministry for the Environment, Govt of New Zealand.

Taylor, J. R. (1997). *An introduction to error analysis: the study of uncertainties in physical measurements*. University Science Books, Sausalito, Calif.

Theobald, P., Carran, R., and Evans, J. (1995). Emission of nitrous-oxide from some grazed pasture soils in new zealand. *Australian Journal of Soil Research*, 33(2):341–352.

Townsend, A. (1956). *The structure of turbulent shear flow*. Cambridge University Press, Cambridge.

Vickers, D. and Mahrt, L. (1997). Quality control and flux sampling problems for tower and aircraft data. *Journal of Atmospheric and Oceanic Technology*, 14(3):512–526.

Webb, E., Pearman, G., and Leuning, R. (1980). Correction of flux measurements for density effects due to heat and water-vapor transfer. *Quarterly Journal of the Royal Meteorological Society*, 106:85–100.

Welch, P. (1967). The use of fast fourier transform for the estimation of power spectra: A method based on time averaging over short, modified periodograms. *IEEE Transactions on Audio and Electroacoustics*, 15(2):70–73.

Wilson, J., Flesch, T., and Harper, L. (2001). Micro-meteorological methods for estimating surface exchange with a disturbed windflow. *Agricultural and Forest Meteorology*, 107:207–225.

Wyngaard, J. (1992). Atmospheric turbulence. *Annual Review of Fluid Mechanics*, 24:205–233.

Yaglom, A. (1977). Comments on wind and temperature flux-profile relationships. *Boundary-Layer Meteorology*, 11(1):89–102.

Zhang, Y., Liu, H., Foken, T., Williams, Q. L., Liu, S., Mauder, M., and Liebethal, C. (2010). Turbulence spectra and cospectra under the influence of large eddies in the energy balance experiment (EBEX). *Boundary-Layer Meteorology*, 136(2):235–251.